ROUGH AIRFOIL SIMULATION FOR WIND TURBINE APPLICATIONS

A Dissertation Presented

By

Nathaniel B. deVelder

Submitted to the Graduate School of the
University of Massachusetts Amherst in partial fulfillment
of the requirements for the degree of

Doctor of Philosophy

February 2020
Mechanical and Industrial Engineering

ROUGH AIRFOIL SIMULATION FOR WIND TURBINE APPLICATIONS

A Dissertation Presented

By

Nathaniel B. deVelder

Approved as to style and content by:

Matthew Lackner, Co-Chair

James Blair Perot, Co-Chair

Hans Johnston, Member

James Manwell, Member

Sundar Krishnamurty, Department Head
Mechanical and Industrial Engineering

ACKNOWLEDGEMENTS

Thank you to my co-advisers Dr. J. Blair Perot and Dr. Matthew Lackner for the years of patient, knowledgeable, and kind support and mentorship. Thank you also to my committee members Dr. James Manwell and Dr. Hans Johnston for taking part in this dissertation process, teaching interesting classes, and engaging with my curiosity. Thanks to Dorothy Adams for all the administrative help throughout the years. Thanks to Dr. Jim Manwell and Dr. Jon McGowan for taking a chance on admitting me as a music major with little engineering experience. Thanks to my friends and colleagues in the masters and doctoral programs for all the study sessions, discussions, and support. Lastly, thank you my partner Emily Stephens, without whom this dissertation would not have been possible, for the support, encouragement, and motivation over my extended program at the University of Massachusetts.

ABSTRACT

ROUGH AIRFOIL SIMULATION FOR WIND TURBINE APPLICATIONS

FEBRUARY 2020

NATHANIEL B. DEVELDER, B.A., BOSTON UNIVERSITY

M.S.M.E., UNIVERSITY OF MASSACHUSETTS AMHERST

Ph.D., UNIVERSITY OF MASSACHUSETTS AMHERST

Directed by: Professor J. Blair Perot and Professor Matthew A. Lackner

As a result of insects or other environmental fouling, surface roughness on wind turbine blades can reduce power output significantly. Superhydrophobic surfaces, though possibly a passive, cost-saving, answer to the problem of ice accretion on wind turbine rotors in cold climates, may alter turbulence development in the blade boundary layer similar to environmental roughness. This work uses an equivalent sand grain extension to the Turbulent Potential model to computationally assess the aerodynamic effects of surface roughness on the s809 airfoil, including a representational superhydrophobic surface. Rough surface boundary layer theory, application of the equivalent sand grain method, roughness parameter correlation, and wind turbine aerodynamic computational approaches are discussed. Modifications to the Turbulent Potential model including turbulence Reynolds number dependence are addressed. An altered version of the Turbulent Potential model is proposed using an elliptic damping equation in the pressure strain term. Validation of Turbulent Potential model changes is demonstrated by comparison to multiple direct numerical simulations of Moser et al., the impinging jet of Cooper et. al, and the Ohio State University wind tunnel experiments of the s809 airfoil with both a smooth and rough leading edge.

CONTENTS

LIST OF TABLES

LIST OF FIGURES

Figure **Page**

CHAPTER 1

INTRODUCTION

On April 20, 1943, the U.S. Patent Office awarded James Dobson Altemus a patent for a system of infrared lamps [1], that when affixed in strategic parts of an airplane, could prevent propeller and wing ice formation. Whether or not Altemus' system ultimately worked, his invention is an interesting early attempt to prevent ice accretion in a device that necessitated maintenance of its geometric shape for aerodynamic effectiveness and therefore safety. Ice accretion, on an aerodynamic-reliant machine, causes bulk shape and density distortions, and therefore unexpected behavior of that machine. Much like the wing or propeller of an airplane; safe, reliable, and long-lasting operation of a wind turbine in a cold climate is dependent on maintaining the geometry and material properties of the rotor by preventing ice accretion.

It has been surmised that highly water-repellent superhydrophobic surfaces (SHS) could be a passive, cost-lowering answer to the problem of ice accretion on wind turbine rotors in cold climates [2]. Though promising, the benefit of superhydrophobic surfaces, could come at the cost of altering the flow field in unexpected ways. From an aerodynamic perspective, SHS looks like a regularly roughened surface. The intention of this work is to computationally assess the aerodynamic effects of rough surfaces, including superhydrophobic surfaces, in the context of airfoils and wind turbine rotors, without making any claims on the effectiveness of superhydrophobic surfaces. As a means of providing background in this ef-

fort, cold climate wind resources, current wind turbine ice mitigation techniques, superhydrophobic surfaces, wind turbine simulation, turbulence modeling, and computational approaches to roughness are addressed.

1.1 Wind Turbines and Superhydrophobicity

In a 2013 report [3], classification society Germanischer Lloyd (now part of DNV GL after a merger with Det Norske Veritas) defines a cold climate as one in which "minimum temperatures of below $-20°C$ have been observed during long term measurements (preferably ten years or more) on an average of more than nine days a year." Accordingly, the $-20°C$ temperature must have been reached for a minimum of one hour per day. However, a cold climate based on this definition may or may not be a climate that encourages icing. The International Energy Agency Programme for Research, Development and Deployment on Wind Energy Conversion Systems produced a report that details growth conditions for various types of ice, and notes that few icing events occur below $-25°C$ [4]. The label "cold climate" will be used throughout this work to represent both large-region cold climates (such as the entirety of northern Canada) and micro cold climates (such as a mountaintop that experiences cold climate like conditions despite being surrounded by more temperate regions).

Despite several cold climate failure modes for wind turbines, there are several advantages to locating wind turbines in cold climate areas. These include a cost balance between increasingly-limited temperate locales for wind turbines (due to ecological considerations, population density and NIMBYism, and simple resource

location), the high costs of moving offshore, and the increased costs of adaption to cold climates. Baring-Gould et al. [4] are positive about the potential for cold climate development. It is also noted in [5] that air density increases with decreasing temperature, while scaling wind turbine power output linearly, and as such could be advantageous for power production. Despite acknowledging a lack of market studies quantifying cold climate resource potential, [4] notes a "vast wind energy production potential" for cold climate sites. A mapping of western Europe for icing events is shown in [6] however it is not compared with wind resource maps of the same region.

In a review of wind turbine icing mitigation techniques [2], Parent describes several effects of ice formation on wind turbines. Measurement errors of anemometers can be as high as 60% during an icing event. Annual power production can decrease as much as 50% depending on duration and intensity of an icing event. Overproduction, mechanical failures, electrical failures, and safety hazards are all documented in the literature cited in [2]. Ice growth has also been shown to weigh as much as 50% of blade weight, underscoring the significant danger of ice to the structural integrity of the blades [7]. Clearly, costs associated with these errors, decreased efficiencies, failures, and hazards can be significant, depending on the duration, frequency, and severity of icing events. Icing mitigation broadly falls into two categories, active and passive. Active icing mitigation techniques assume the use of additional energy (e.g. thermal, chemical, or kinetic) during or after an icing event to prevent or remove ice. Passive techniques, as focused on in this work, assume the use of intrinsic material or device properties, such as surface

features, surface colors, or blade material properties, to discourage the formation of ice or remove ice formations. A review of mitigation techniques is given in [2, 5].

It is said that in 1941, swiss engineer Georges de Mestral went for a walk with his dog and returned covered in burrs. Eight years later he had perfected a product, Velcro™, that proceeded to become so ubiquitous that most hook-and-loop fasteners are now referred to by that name regardless of brand [8, 9]. Velcro™, is one of a significant number of everyday products that have been directly inspired by, or later found to mimic, the natural world. This is known as biomimicry, or biomimetic development, a term coined by Otto Schmidt in the 1960s, and included in Webster's Dictionary in 1974 [9].

The water-shedding property of the lotus leaf is another example of a natural phenomenon that has been studied and adapted for human use. The lotus leaf surface is said to be superhydrophobic due to microscale surface features that repel water droplets by increasing the droplet-surface contact angle [9–11]. Interestingly, Cheng and Rodak [11] found that the superhydrophobicity of the lotus leaf is not maintained during condensation.

The wettability, or tendency of a surface to attract or repel water can be categorized as hydrophobic, meaning water repellent, or hydrophilic, meaning water attracting. Wettability is measured in the form of a water droplet's contact angle θ_{CA} with a surface. High contact angles ($\theta_{CA} > 90°$) are associated with hydrophobicity, and contact angles larger than approximately 150° are considered to

be superhydrophobic [12]. Contact angles are also classified as static or dynamic, with dynamic angles having a hysteresis $\Delta\theta_{CA}$ dependent on the heterogeneity and/or dynamism of the surface [12]. Given the purpose and scope of this work, superhydrophobic surfaces are assumed to repel water and inhibit ice accretion due to regularly pattered surface asperities, a discussion of which can be found in [5, 13–16]. The balance of this work focuses on the nature of SHS surface asperities and the aerodynamic effect that surface asperities exhibit on the boundary layer flow of airfoils and wind turbine blades.

1.2 Other Roughness Types

Dalili et al. [5] discuss multiple ways that wind turbine blades become fouled and face reductions in power output. One such issue is insects that fly during periods of low wind, getting hit, and becoming attached to the turbine blade. Dalili cites Corten et al. claiming that low levels of insect contamination can reduce turbine output by up to 8% while high levels can reduce turbine output up to 55%. Surface fouling, increasing the roughness of the blade surface, is therefore a significant issue for which the turbine industry needs solutions. Dalili also cites a patent by Somers and Tangler (the creators of the s809 airfoil) for roughness insensitive airfoils, however we will see later in this work that even the s809 can be affected by rough surfaces.

Dalili et al. [5] also have a short section on blade erosion. This is a problem when the air is carrying a significant amount of small particulates which strike the blade at high speeds, damaging blade coatings and surfaces, causing roughness.

This problem is amplified in higher speed sections of the blade, as higher speed particulates (relative to the blade velocity) will do more damage. The gas turbine industry also considers surface fouling and erosion a serious problem and has developed a number of technologies to mitigate the problem as discussed in [17].

1.3 Dissertation Overview

The primary goal of this dissertation is to adapt the Turbulent Potential model, a RANS turbulence model used in computational fluid dynamics, to incorporate rough surface boundary conditions that could be used to both design against, and predict the performance degradation of, fouled airfoils. Secondarily, we aim to state whether or not superhydrophobic surfaces would likely impact the aerodynamic performance of wind turbine airfoils in the same way that surface fouling would. Towards these aims, we review the multiple levels and fidelities of current practice in wind turbine modeling. The effects of surface roughness and superhydrophobic surfaces are described broadly and then given general context in fluid dynamics. The Turbulent Potential model is then described, along with a number of modeling changes implemented during the course of this research. Rough surface boundary conditions in other turbulence models are discussed. Two methods applied to the $k\omega$-SST model are identified as candidates for adaptation to the Turbulent Potential model, and the arrival at a full set of rough boundary conditions for the TPM is derived from that starting point. Results from turbulent channel flow, impinging jets, the NASA 2D hump case, and the s809 airfoil are shown and discussed. The effects of the rough surface boundary conditions on the

s809 airfoil are compared to the Ohio State University experiments and then applied with mock SHS coatings to view the effect. Findings could be applied to the design of new airfoils that are even less roughness dependent than the s809. New airfoil data could be used in any number of reduced order modeling techniques that rely on airfoil data for their conclusions.

The work presented here is, to the author's awareness, the first to employ wall-normal Reynolds stress in an equivalent sand grain roughness modeling approach. Also presented is the first attempt at inclusion of elliptic pressure-strain damping in Turbulent Potential Model (or equivalently turbulent potentials in a $\boldsymbol{v^2f}$like model). This work also provides analysis of turbulence Reynolds number dependence, using an extended range of turbulence Reynolds numbers, on turbulence diffusion. Also presented is a preliminary examination of the aerodynamic impact of micron-size rough surfaces on airfoil flow.

CHAPTER 2

REVIEW OF COMPUTATIONAL METHODS IN WIND TURBINE AERODYNAMICS

Recent data shows that electricity from renewable sources grew to almost 15% of total installed capacity in 2013 in the United States [18]. Generation from wind power machines increased 20% in 2013, while total wind electric capacity grew by 1.8% [18]. Such increased usage of wind power, alongside a push to quantify and eventually utilize a significant off-shore wind resource [19], has led to an exponential growth in academic research on wind power topics.

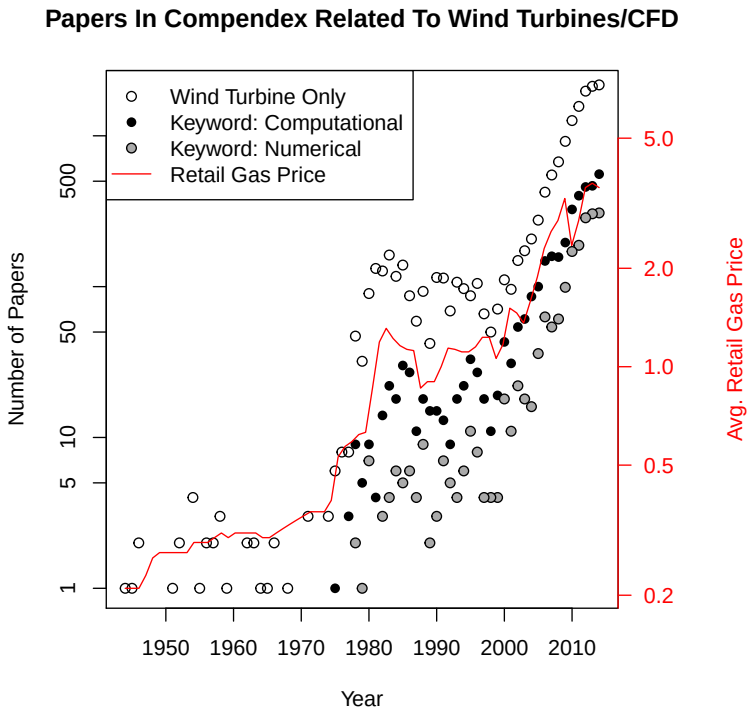

Figure 2.1: Query to Compendex showing trends in computational wind energy research. Average retail gas price is measured in dollars.

Figure 2.1 shows three simple queries to the Compendex, a computerized version of the Engineering Index. The first is for the words "wind" and "turbine" in the paper title field, and the second and third add the keywords "numerical" and "computational" respectively in searching the subject, abstract, and title fields. Qualitatively, the numbers show a research response to the 1973 oil crisis and subsequent oil price increases of the late 1970's, followed by a slight decline, then exponential growth starting around the early 2000s.

Much of this research has focused on the aerodynamic modeling of wind turbines and groups of interacting wind turbines. Note that there is a difference between "aerodynamic" and "aeroelastic" calculations, respectively considering rigid and deformable bodies in fluid flow. The focus of this work is the state of aerodynamic modeling methods, though there certainly is some overlap in practice. Aerodynamic modeling of wind turbines poses significant challenges. These challenges can be addressed using several methods, all involving trade-offs in engineering-level assumptions for ease and cost of computation.

2.1 Challenges in Aerodynamic Modeling of Wind Turbines

A comprehensive approach to wind turbine aerodynamic modeling necessitates a thorough understanding of environmental flow fields and wind turbine technology. The illustration in figure 2.2 collectively depicts aspects of a wind turbine system that add complexity to wind turbine modeling. The figure shows a turbine with tapered and twisted blades in a turbulent, sheared flow field, with turbine yaw,

blade pitch, and blade rotation degrees of freedom. Also shown is a floating offshore platform, which adds surge, sway, heave, pitch and roll degrees of freedom.

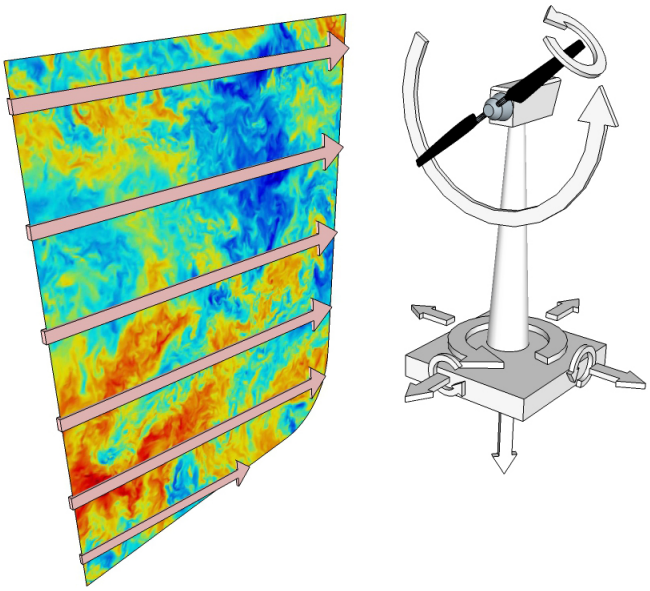

Figure 2.2: Pictorial representation of mean velocity shear, turbulent fluctuations, turbine yaw, platform motions, blade rotation, and blade pitch

Rotational motion of the rotor infers a spanwise distribution of velocity that results in pressure imbalances that drive span-wise flow. Relatedly, finite length blades result in pressure imbalances that cause "roll-up" or flow around the tip and the root of the blade. Not represented in the illustration are interactions between the rotor and tower, and the rotor and its own wake. Ultimately, each of these physical realities contributes to the performance of a wind turbine, and every modeling approach must be assessed on the assumptions made to represent flows that result from these conditions.

A 2001 blind comparison study of wind turbine modeling methods [20] illustrates the significant differences between various modeling approaches. Thirty experts, from eighteen organizations, ran the same simulations using nineteen different

modeling tools on twenty separate cases. Under the simplest of conditions, turbine power predictions varied between 25% and 175% of the measured power output, and results at higher wind speeds were even worse [20].

2.1.1 Reynolds Number

Wind turbine blades experience high magnitude and wide ranging chord-based Reynolds numbers given blade rotation and variation in freestream wind conditions. Figure 2.3 shows differences in Re_c on the order of 3×10^6 at span-wise stations for a linearly-tapered blade with a radius of 50m, root chord of 4m, and tip chord of 0.67m.

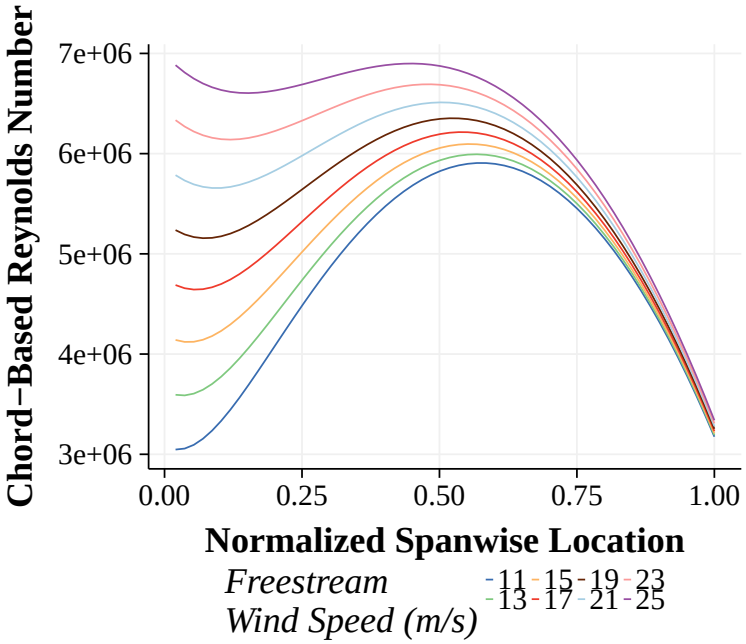

Figure 2.3: Variation in Re_c along the span of a simplified 50m blade rotating at 13 rpm, at freestream wind values corresponding to a maximum power operating state.

For computational fluid dynamics simulations, increasing Reynolds number is directly correlated with computational expense. As the important physical pro-

cesses in the boundary layers get pushed closer to the wall, smaller computational mesh sizes are required to represent them.

2.1.2 Separation

Given that utility scale wind turbines operate at high values of Re_c, variations in angle of attack can result in separation. Several papers [21–23] show the challenge of predicting separating airfoil flows with computational fluid dynamics (CFD) methods. Issues around the prediction of dynamic stall are also related to separation modeling [24].

2.1.3 Transition

The s809 [25], a 21% thickness to chord ratio airfoil designed specifically for use on wind turbines, has geometric properties such that for mild angles of attack, the flow around the front half of the airfoil is laminar. Transition prediction is notoriously difficult for turbulence models and can significantly impact pressure distribution predictions [21]. Correct prediction of transition in commonly used RANS models often necessitates the use of a separate model that involves some a priori knowledge of the transition location.

2.1.4 Rotation

The velocity experienced by any point on a wind turbine blade is dependent both on span-wise radial position and, in cases of large diameter turbines experiencing sheared flow, blade azimuth dependent. At certain Reynolds numbers, this may

result in span-wise flow at the blade. Lower order models such as the Blade Element Momentum Method rely on the assumption of radial independence. Also, as discussed earlier, rotation may result in a significant spanwise range of Reynolds numbers, making computational meshing more challenging and/or expensive.

2.1.5 Turbulent Flow Fields

Representation of turbulent flow in airfoil and wind turbine modeling can take many forms, from using logarithmic profiles that obliquely include turbulence effects, to the direct modeling of all flow scales and structures around airfoils at low Reynolds numbers. Turbulence modeling is discussed starting in section 2.4.1.

2.2 Momentum Theory

The simplest, oldest, and most widespread engineering-level method for modeling the horizontal-axis wind turbine (HAWT) is known as blade element momentum theory (BEM). It is generally considered that Wilson and Lissaman [26] introduced blade element momentum theory for use in numerical computations of wind turbines [27–30]. Their work followed 19th century research on actuator disk theory by W.J.M. Rankine (1865) in his work on marine propellers, as well as W. Froude (1878), R.E. Froude (1889), and S. Drzewiecki (1892). Further development came after the turn of the century by Drzewiecki (1920), Lanchester (1915), Joukowski (1918), Prandtl (1919), Betz (1920,1922), and Goldstein (1929) with a formal generalization of the theory by Glauert in 1935 [31]. Various publications give more or less credit to individual researchers, a historical parsing of which is beyond the

scope of this work [26–28, 30, 32–36].

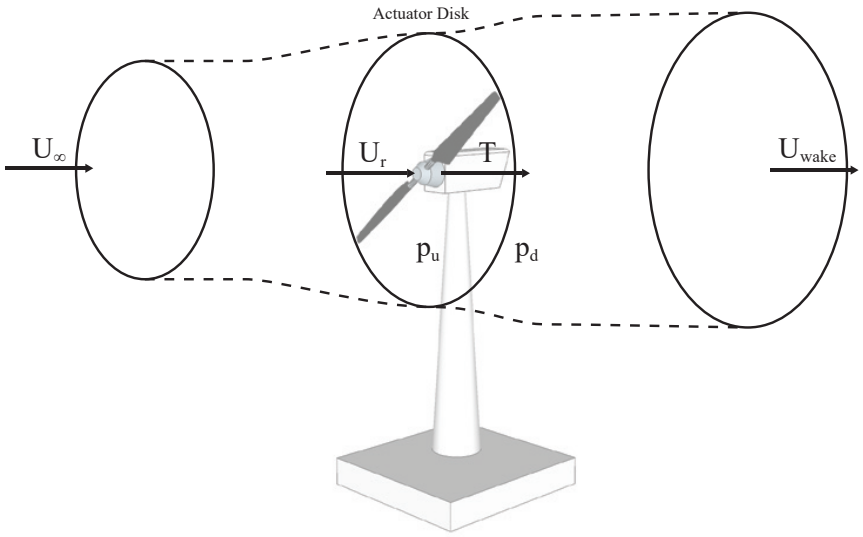

Figure 2.4: Control volume for basic 1D momentum theory across a wind turbine rotor

Figure 2.4 shows a simple control volume surrounding a wind turbine rotor. Assuming no flow through the control volume (streamtube) boundary, mass flow rate should be equivalent on both sides of the rotor plane.

$$\dot{m} = \rho A U \tag{2.1}$$

Assuming a divergence-free velocity field, the following equivalence can be made:

$$\rho A_\infty U_\infty = \rho A_r U_r = \rho A_{wake} U_{wake} \tag{2.2}$$

Axial induction can then be defined in equation 2.3 as a percentage deficit of wind velocity due to momentum extraction of the rotor,

$$a = 1 - \frac{U_r}{U_\infty} \qquad or \qquad U_r = U_\infty(1-a). \tag{2.3}$$

Through the application of Bernoulli's equation to the control volume, an equation for thrust is derived,

$$T = 2\rho A U_\infty^2 a(1-a). \tag{2.4}$$

Multiplying thrust by U_r gives an equation for power.

$$P = 2\rho A U_\infty^2 a(1-a)U_r = 2\rho A U_\infty^3 a(1-a)^2 \tag{2.5}$$

And the thrust and power coefficients are given by equations 2.6 and 2.7.

$$C_T = \frac{T}{1/2\rho A U_\infty^2} = 4a(1-a) \tag{2.6}$$

$$C_P = \frac{P}{1/2\rho A U_\infty^3} = 4a(1-a)^2 \tag{2.7}$$

Equation 2.7 has a maximum at $a = 1/3$ and so results in $C_{P_{max}} = 0.593$. Known as the Betz limit, this means that only 59.3% of aerodynamic power in the

streamtube is available to be converted to mechanical power. Sørenson [37] shows this to be a conservative maximum given that rotational effects are ignored, and should be reduced by approximately 5%.

So far in this analysis, only axial momentum has been considered, but rotational effects are significant as well. Rotational induction is shown in equation 2.8, where U_θ is the rotor plane component of velocity imparted by the rotor onto the flow, in the opposite direction of the blade rotation.

$$a' = \frac{U_\theta}{2\Omega r} \tag{2.8}$$

The velocity at the rotor disk in a 2D blade section coordinate system is a sum of axial and rotational velocities.

$$U_{rel} = U_\infty(1-a)\hat{i} + \Omega r(1+a')\hat{j} \tag{2.9}$$

Figure 2.5 illustrates the relevant angles and velocities from a cross section of a wind turbine blade.

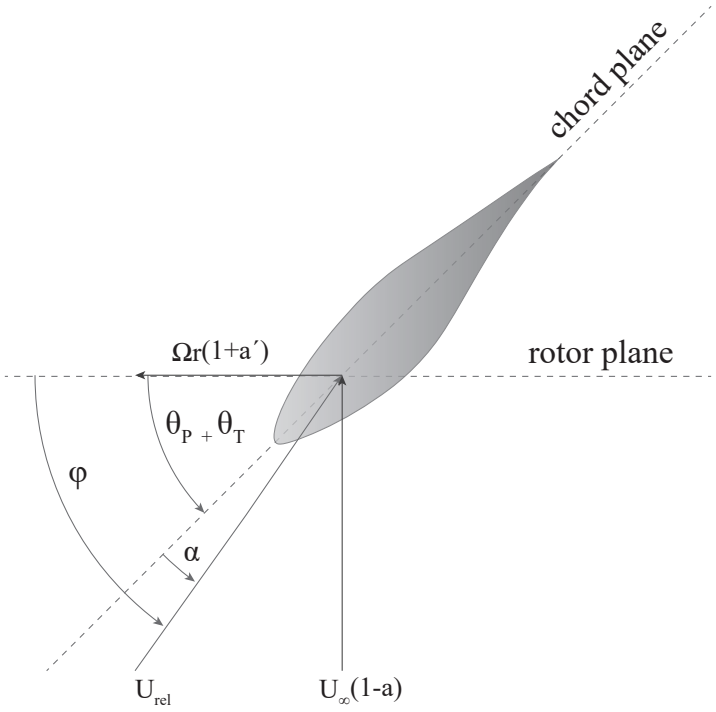

Figure 2.5: Momentum Theory Geometry

Glauert [31] contributed the primary conceptual idea of BEM, which is to split the actuator disk into radially spaced (annular) control volumes as in figure 2.6, and locally solve a momentum and energy balance assuming constant forcing and no interaction between successive annuli. Several sources derive the full set of equations for the standard Blade Element Momentum Method [27, 30, 35, 38, 39], some of which depend on iterative solutions for axial (a) and rotational (a') induction factors.

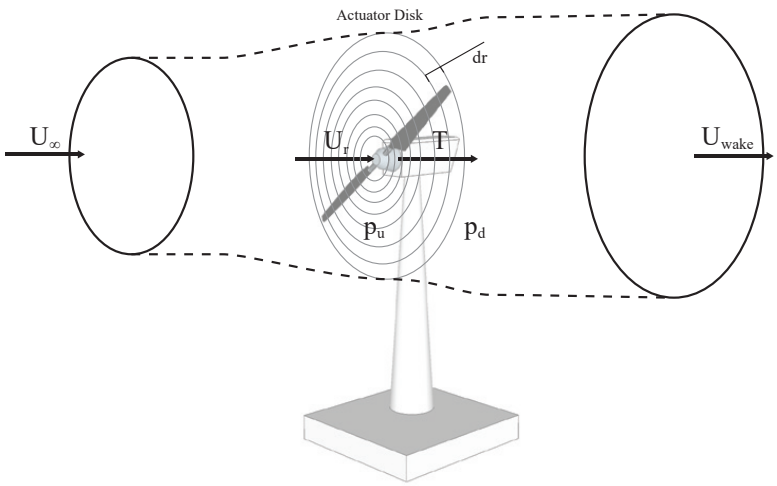

Figure 2.6: Annuluar approach to BEM equations

$$\varphi = tan^{-1}\left(\frac{U(1-a)}{\Omega r(1+a')}\right) \tag{2.10}$$

$$a = \frac{1}{4sin^2\varphi/(\sigma C_n)+1} \tag{2.11}$$

$$a' = \frac{1}{4sin\varphi cos\varphi/(\sigma C_t)-1} \tag{2.12}$$

$$\sigma = \frac{cN_{blades}}{2\pi R} \tag{2.13}$$

Figure 2.7 shows the general algorithm for iterative versions of the Blade Element

Momentum method. Note that BEM is dependent on the accuracy of table-lookup data for airfoil lift and drag, which Tangler shows in [40] to vary significantly.

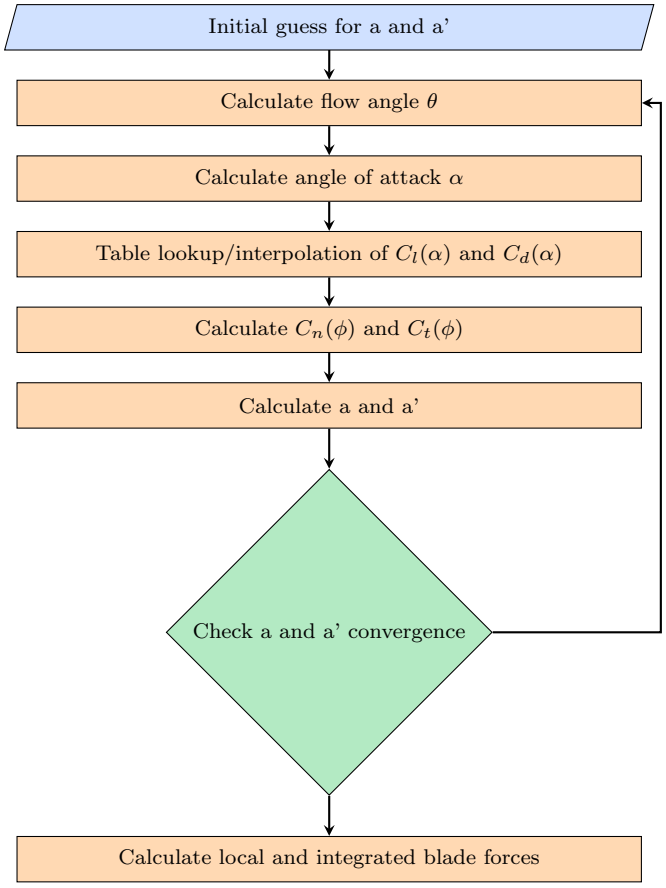

Figure 2.7: Flow diagram of basic BEM algorithm

Note that Manwell et al. derive equations for a and a' that do not necessitate iterative solutions. Several corrections are necessary to increase the accuracy of basic BEM theory. To account for a finite number of blades, Prandtl's tip-loss factor can be included. The Glauert correction is necessary for axial induction factors larger than 0.4-0.5, in which the turbine enters a turbulent wake state and momentum theory breaks down [35].

Several computational codes are publicly available that can use BEM to solve

wind turbine aerodynamics. Primary among the free options are the aeroelastic code FAST from the U.S. National Renewable Energy Laboratory (NREL), PROPID from the University of Illinois Urbana-Champaign, and Q-Blade originally from TU Berlin. Commercial options like ADAMS from MSC.Software, and Bladed from DNV GL, are also available. FAST, ADAMS, and Q-Blade all integrate the BEM aerodynamics code AeroDyn, also developed at NREL. A comparative assessment of certification-level wind turbine design codes was written by Buhl in 2006 [41], however several industry and software changes out-date some information contained in that work.

Research involving the blade element momentum method retains relevance because of its low computational cost and proven effectiveness within applicability limits. BEM research can generally be categorized in one of three ways: wind turbine design, expansion of model applicability and accuracy, and the integration general momentum methods into higher-complexity methods. Each of these categories usually involves comparison or validation with experimentation or higher-order methods.

2.2.1 Wind Turbine Design and Standards

Several reviews and book chapters of wind turbine aeroelasticity and aerodynamics exist in the literature [27, 39, 42–46], and discuss formative work on turbine design. Turbine manufacturers looking for design certification through the International Electrotechnical Commission (IEC) still need to prove, using an aeroelastic code, that their designs will in fact match their advertised ratings. Interesting recent

approaches to momentum-based wind turbine design include the use of BEM with evolutionary or genetic algorithms [47].

Literature using BEM in this topical area is generally concerned with the addition of models for specific physical processes or turbine states, such as yawed inflow, dynamic inflow, dynamic stall, offshore platform motion, or improved C_l vs. α curves.

Momentum based methods can be used within higher-complexity models when resolution of the rotor flow-field is less important than larger scale flow-field dynamics. Such methods will be discussed in section 2.4 on actuator disk methods in Navier-Stokes based computational fluid dynamics.

2.3 Inviscid Computational Methods

Wind turbine simulation methods that assume inviscid, irrotational, incompressible flow inhabit a computational middle ground between momentum based methods and full viscosity-inclusive Navier-Stokes based methods. Inviscid methods make use of the assumption that viscous effects inside the boundary layer are negligible compared to the flow outside the boundary layer. These methods are referred to in the literature as "Potential Flow" methods or "Vortex" methods [24, 48]. The advantage to using such methods over BEM is their intrinsic handling of unsteady and yawed flow states [49]. Vortex methods have their roots in works such as Prandtl [50], Jones [51], and Weissinger's [52] work on lifting line theory. Vortex methods were used in the helicopter industry as early as 1967 [24].

Potential flow methods are broadly categorized into two types based on handling of wake geometry, prescribed wake models and free wake models. Prescribed wake models, by using prescription functions for wind turbine wake geometry, avoid computation of wake self-induction and advection, thereby decreasing computational expense. This trade-off limits prescribed wake methods to well-known and calculable flow states. This limitation seems to explain the comparative predominance of literature on free-wake methods. A recent paper by Breton, Coton, and Moe compared dynamic stall models and the NREL Phase VI data using a prescribed wake vortex code [53]. Coton, along with other authors, has published several papers on the use of prescribed wake models for both vertical and horizontal axis wind turbines [54–57]. Chattot has written extensively on a prescribed wake model for wind turbine analysis [58–62]. Cline and Crawford show that transitioning from a free wake to prescribed wake model, at increasingly downstream distances, results in slight but increased accuracy in angle of attack [48]. Early work in prescribed wake analysis comes from helicopter rotor simulations [63–65] and starting in 1991, wind turbine analysis [66–72].

Alternatively, free wake models allow the geometry of the computational grid to convect freely amidst the solution. Gupta and Leishman et al. [24, 38, 73–76], Kloosterman [49], Sebastian and Lackner [77, 78], Sezer-Uzol et al. [79], and Sant et al. [80, 81] are all known for recent work on free-wake vortex models.

2.3.1 Potential Flow Background

Starting with the incompressible Navier-Stokes equations for momentum and continuity, equations 2.14 and 2.15 respectively, we see that the inviscid assumption results in the Euler equation for momentum (eq. 2.16) where variables are defined at the beginning of this work.

$$\frac{\partial \mathbf{u}}{\partial t} + (\mathbf{u} \cdot \nabla)\mathbf{u} = \frac{1}{\rho}\nabla p + \nu \nabla^2 \mathbf{u} \tag{2.14}$$

$$\nabla \cdot \mathbf{u} = 0 \tag{2.15}$$

$$\frac{\partial \mathbf{u}}{\partial t} + (\mathbf{u} \cdot \nabla)\mathbf{u} = \frac{1}{\rho}\nabla p \tag{2.16}$$

Given that a velocity field can be represented as the gradient of a scalar function, the velocity potential, we can rewrite the velocity,

$$\boldsymbol{u} = \nabla \phi, \tag{2.17}$$

where ϕ is the stream function. In applying continuity, we get Laplace's equation.

$$\nabla \cdot \mathbf{u} = \nabla \cdot \nabla \phi = \nabla^2 \phi = 0 \tag{2.18}$$

Potential flow methods ultimately come down to solving equation 2.18. As Katz and Plotkin [82] note, the Euler equation is used to connect velocity to pressure and is only necessary for calculation of aerodynamic forces.

Assuming no body forces and applying momentum in the form of Euler's equation, we get the unsteady Bernoulli equation through integration as shown in [83].

$$\frac{\partial \phi}{\partial t} + \frac{1}{2}(\nabla \phi)^2 + \frac{p}{\rho} = f(t) \tag{2.19}$$

Potential flow methods, in the most general of terms, involve locating and orienting the fundamental solutions to Laplace's equation, such that solid boundaries and flowfield physics are properly represented. Fundamental solutions include sources (and sinks), doublets, and vortices. The potential vortex has been widely used in aircraft and wind turbine simulations, on account that it can fully represent circulation and therefore lifting surfaces.

2.3.2 Vortex Methods

Cottet and Koumoutsakos [84] provide a thorough survey of the general use of vortex methods. Karamcheti [83] and Katz & Plotkin [82] describe vortex methods in the context of aerodynamic flows. To start, vorticity and circulation are defined in equations 2.20 and 2.21.

$$\boldsymbol{\omega} = \nabla \times \mathbf{u} \tag{2.20}$$

$$\Gamma \equiv \oint_C \boldsymbol{u} \cdot d\boldsymbol{l} \tag{2.21}$$

Circulation is related to vorticity through the use of Stokes' theorem as in equation .

$$\Gamma \equiv \oint_C \boldsymbol{u} \cdot d\boldsymbol{l} = \int_S \boldsymbol{\omega} \cdot \boldsymbol{n} dS \tag{2.22}$$

Wind turbine blades are then represented as either lines (also called tubes or filaments) of "bound" circulation located at the 1/4 chord, or as geometric panels representing actual blade geometry. The first of these methods is known as Prandtl's lifting line theory. Bound circulation can be calculated using the Kutta-Joukowski theoreom and airfoil table lookups.

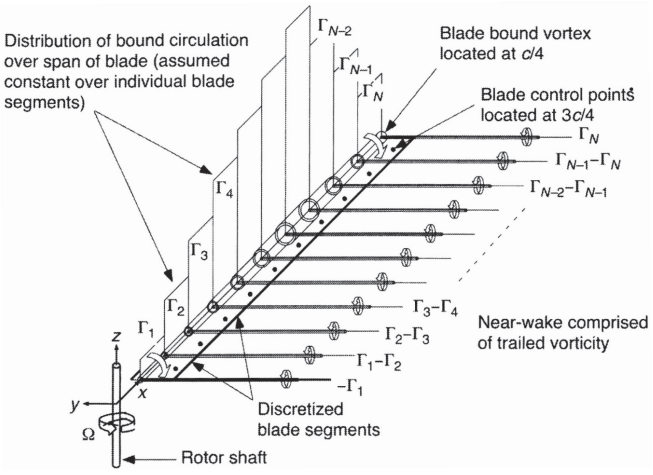

Figure 2.8: Lifting Line Illustration from Leishman [32]

Loops of vortex lines are superimposed such that the bound vortex line and the

shed and trailing vortex lines form a lattice that represents the wake. Kelvin's theorem states that the total amount of circulation on this lattice cannot change with time.

$$\frac{D\Gamma}{Dt} = 0 \tag{2.23}$$

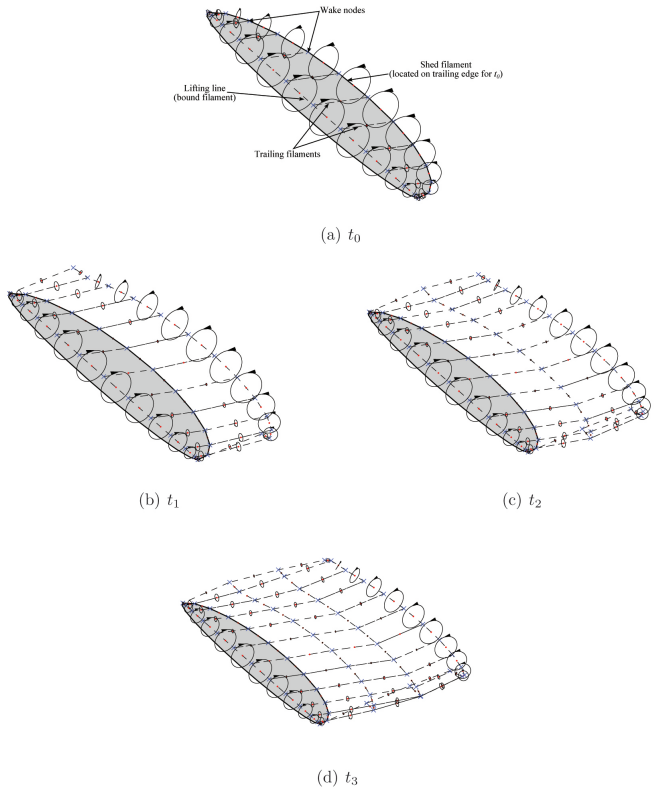

Figure 2.9: Wake development off of lifting line from Sebastian [77]

Each filament has the effect of inducing velocity at all other filaments, which is calculated using the Biot-Savart Law.

$$\boldsymbol{u} = \frac{\Gamma}{4\pi} \int \frac{d\boldsymbol{l} \times (\boldsymbol{r}_0 - \boldsymbol{r}_1)}{|\boldsymbol{r}_0 - \boldsymbol{r}_1|^3} \tag{2.24}$$

Panel methods calculate circulation at the blade by arranging vortex filaments into a geometric grid (similar to a 3D model) that is used to enforce a no-entry boundary condition. Similar methods are used for trailing and shed wake filaments.

2.3.3 Hybrid Methods

Some researchers have been successful in merging viscous Navier-Stokes computations in the near wake and vortex methods in the far wake. Borrowing an approach from the helicopter industry, Xu and Sankar [85] develop a hybrid methodology which compares favorably against the NREL Phase II and III data. In a later paper [86], they also compare to the NREL Phase VI rotor experiment with mixed but "encouraging" results dependent on spanwise position. Schmitz and Chattot also present work on a hybrid method with a prescribed wake [87, 88].

2.3.4 Computational Considerations

Calculation of induced velocity using the Biot-Savart Law comes at a computational cost of the grid size squared e.g. $\mathcal{O}(N^2)$. In wing and blade simulations, grid size grows as nodes are shed into the wake making each timestep more expensive. Several approaches can be taken to cut down on this computational expense.

2.3.4.1 Induced Velocity Calculation Reduction

Leishman [89] notes several methods for reducing the number of induced velocity calculations in a free-wake vortex code. These include simply using fewer vortex elements, subdividing the wake into influential and non-influential regions, and

alternating freely-convecting nodes with interpolated nodes.

2.3.4.2 Algorithmic Improvement

$\mathcal{O}(N^2)$ problems, also known as N-body problems, exist in many scientific fields including particle physics, astronomy, and electrical engineering. In 1986, Barnes and Hut, working in the context of gravitational simulations, designed what is termed a "tree-code" and reduced the N-body algorithmic cost from $\mathcal{O}(N^2)$ to $\mathcal{O}(NlogN)$ with some quantifiable error [90]. One year later, Greenguard and Rokhlin developed an algorithm that went even further, taking N-body problems from $\mathcal{O}(N^2)$ to $C\mathcal{O}(N)$ [91], that would later be termed the Fast-Multipole Method. This constant C is large, so there is a threshold at which this method becomes an efficiency gain.

2.3.4.3 Use of Specialized Hardware

The Gravity Pipe (GRAPE) project started in 1989 with the goal of developing specialized hardware to speed up gravitational simulations [92]. The base premise of GRAPE hardware is to use more transistors per chip as arithmetic units (as opposed to more general purpose caches, control logic, buses etc.) and as such can perform orders of magnitude more floating-point operations per clock cycle [92]. Graphics processing units (GPUs) have also been shown to improve the computational speed of N-body problems significantly [93–103].

2.4 Viscous Computational Fluid Dynamics

Computational fluid dynamics (CFD) modeling of wind turbines is the youngest of modeling techniques discussed in this work. Multiple review papers [37, 104] credit the first full Reynolds-Averaged Navier-Stokes simulation of a rotor blade to N. N. Sørensen and M. Hansen in 1998. The separation of fluidic length scales in a wind turbine flow is the major challenge presented by such simulations. Assuming $10^6 < Re_c < 10^7$, a wall-resolved Reynolds-Averaged Navier Stokes solution for a unit chord blade would require a first grid point on the order of $1e^{-5}m < \Delta y < 1e^{-6}m$ to properly model the blade boundary layer, whereas the rotor diameter of a turbine is on the order of $10m < D < 100m$. CFD methods are broadly categorized by the ways in which they approach these scales, whether it be full resolution, filtering, averaging, or making assumptions that cut down on the range of length scales to be simulated.

Wind turbine simulation with computational fluid dynamics (CFD) is generally carried out using the **incompressible** Navier-Stokes equations, shown in differential form in 2.14 and 2.15. Most literature on wind turbine CFD tends toward a finite volume approach to these equations, though a recent paper by Hsu shows that the finite-element method is also used [105].

As noted above, CFD methods can be classified based on approach to scale representation. Direct numerical simulations solve the Navier-Stokes equations directly, resolving all scales present in the flow. Large Eddy Simulations (LES) use spatial filtering schemes to solve larger scales directly and model smaller scales.

Reynolds-Averaged Navier Stokes (RANS) simulations solve averaged equations thereby modeling all scales of the flow.

2.4.1 Direct Numerical Simulation

DNS is not widely used for wind turbine (or related) simulation due to high Reynolds number regimes and subsequent DNS grid resolution requirements. However, some investigators explore wind turbine dynamics at lower Reynolds numbers for clues to behavior at higher Reynolds numbers. Gross et al. studied the s822 airfoil and the phenomenon of rotational augmentation using direct numerical simulation at $Re_c = 100,000$ [106]. A separation control technique is presented in a paper by Zhang and Samtaney using the NACA-0018 airfoil at $Re_c = 10,000$ [107].

An alternate approach to using DNS for wind turbine simulation is to avoid grid resolution requirements by using a momentum based approach at the rotor. Ivanell et al. present DNS of a wind turbine wake using the actuator line method of Sørensen and Shen [45] to represent blade forces [108].

2.4.2 Large Eddy Simulation

LES is used significantly more than DNS in wind turbine (and related) simulations, though almost exclusively for wake modeling in concert with a reduced order method used at the rotor disk. Grid requirements are significantly higher for LES than for RANS models. Choi and Moin [109] show that for $Re_c = 10^6$, over 50 million grid points are needed to properly simulate wall-resolved flow over

a 3D wing with an aspect ratio of 4 using LES. At $Re_c = 10^7$, this requirement increases two orders of magnitude to over 7 billion grid points. Spalart et al. [110], in making the case for DES (method discussed below), estimated 10^{11} grid points for an airliner wing of aspect ratio 8 at $Re_c = 10^7$. Sanderse et al. [111] note that in comparison to RANS, which only requires wall-normal grid refinement, LES requires grid refinement in all three directions.

Books about LES have been written by Sagaut [112], Garnier et al. [Garnier2009], and Volker [Volker2004]. Reviews of LES formulation, modeling considerations, successes, and challenges have been written by Piomelli [113], Moin [114], and Bouffanais [115].

To represent blade forces in LES modeling, three approaches are commonly used: actuator disks, actuator lines, or actuator surfaces. Sanderse et al. provide a thorough background and review of actuator type methods starting with vertical axis work by Rajagopalan et al. in 1990 through work published prior to that paper's release date in 2011 [111]. J. Sørensen's review [37] notes that the first actuator disk approach to HAWT modeling is in Sørensen and Myken in 1992. From 2012 on, LES wind turbine simulations have made up a significant portion of the wind turbine modeling literature.

In 2012, both Yang et al. [116] and Myers and Meneveau [117] published work on turbine spacing in wind farms. Myers and Meneveau found that spacing on the order of 15D for a large wind farm may be optimal, compared to current conventions of approximately 7D. Réthoré [118] proposed a modification to Rhie-

Chow to incorporate discrete pressure jumps found in actuator type methods.

In 2013, Meyers and Meneveau [119] showed streamtube representations of energy and momentum for different wind farm layouts modeled using LES. Story et al. [120] coupled an LES actuator disc approach with the aeroelastic code FAST, using a controller to account for realistic operation. Krogstad and Eriksen [121] published the results of a 2011 blind test comparison of CFD methods in wind energy, reporting that the LES of J.N Sørensen and R. F. Mikkelsen produced the most consistent results. Mo et al. use a blade resolved LES method of NREL Phase VI turbine and show good agreement at a freestream velocity of 7 m/s.

In 2014, several LES papers were published [122–129]. The work of Yang et al. used a mesoscale weather research and forecasting (WRF) model to feed an actuator line wind farm model using an immersed boundary method (IBM) for realistic terrain.

In 2015, Zhou et al. [130] ran an LES of the exact geometry NREL Phase VI rotor, using a wall function approach in the boundary layer, comparing various inflow cases. Allaerts and Meyers [131] show that atmospheric boundary layer (ABL) conditions, specifically a conventionally neutral ABL structure, can significantly impact the power output of a wind farm. Nilsson et al. [132] compute an LES of the Lillegrund wind farm using the actuator disk method. Van der Laan et al. [133] developed an improved $k-\varepsilon$ model and compared it to LES simulations, showing significant improvement in wake profile agreement. Luo et al. [134] studied the aerodynamics and aeroacoustics using an exact geometry LES model. Martínez-

Tossas, Churchfield, and Meneveau [135] showed minimal effects of SGS modeling changes using an actuator line method under uniform inflow, except in the far wake breakdown region. Martínez-Tossas, Churchfield, and Leonardi [136] show similarities between actuator line and actuator disk methods.

2.4.3 Detached Eddy Simulation

Due to prohibitive grid and timestep requirements for full LES simulation of a wing, Spalart et al. suggested "Detached Eddy Simulation" (DES) in a 1997 paper [110]. DES is a hybrid approach that solves for three-dimensional, unsteady flow using a single turbulence model, switching between an LES approach and a Reynolds-Averaged Navier-Stokes (RANS) approach dependent on grid density [137]. This switching takes place by redefining the RANS model length scale as in equation **??**.

$$L_{DES} = min(L_{RANS}, C_{DES}\Delta) \tag{2.25}$$

C_{DES} is a model constant, and Δ is a grid scale that acts as a filter width in LES mode [137]. Grid design is of utmost importance in DES and, as Bunge notes, should only differ from an LES grid in the vicinity of solid walls [137]. Several papers discuss DES development and grid requirements [137–140]

Shur et al. [141] show that DES can represent massively separated flow (α as high as 90°1) over a wing to within 10% of experimental vales.

Li et al. compared DES simulations to RANS simulations of the NREL Phase VI experimental wind turbine using an overset grid method. Results showed minimal difference in the constant pitch cases and DES giving more accurate results in transient pitch cases [142]. Johansen et al. [143] similarly found that their $k-\omega$ SST DES implementation performed similarly to the RANS $k-\omega$ SST, though with significantly more turbulent flow structures. In 2015, Troldborg et al. [144] compared actuator disk, actuator line, and fully resolved modeling methods using DES and RANS approaches, with both steady inflow and Mann algorithm turbulence. Their results show general agreement betweeen the methods, but significant difference in the near wake fully-resolved case when using turbulent inflow conditions.

2.4.4 Reynolds Averaged Navier Stokes Simulation

The use of RANS (also called Unsteady RANS or URANS) simulation for wind turbine models is generally a practical choice, made when high Reynolds number flow converges with a requirement to resolve boundary layer effects on a minimum of computational resources. Though the least expensive of the full Navier-Stokes CFD methods, RANS models are still much more costly than potential flow models and momentum based models.

Reynolds averaging of the Navier-Stokes equations involves decomposing the total velocity, $\boldsymbol{U}(\boldsymbol{x},t)$ into a mean component $\langle \boldsymbol{U} \rangle$, and fluctuating component $\boldsymbol{u}$.

$$\boldsymbol{U} = \langle \boldsymbol{U} \rangle + \boldsymbol{u} \tag{2.26}$$

$$\partial_t \langle \boldsymbol{U_i} \rangle + \langle \boldsymbol{U_j} \rangle \partial_j \langle \boldsymbol{U_i} \rangle = \frac{1}{\rho} \partial_i P + \nu \nabla^2 \langle \boldsymbol{U_i} \rangle - \partial_j \langle u_j u_i \rangle \tag{2.27}$$

$$\partial_i \langle \boldsymbol{U}_i \rangle = 0 \tag{2.28}$$

Equations 2.27 and 2.28 are collectively known as the Reynolds Averaged Navier Stokes (RANS) equations. The last term on the RHS of equation 2.29 is the divergence of the Reynolds stress tensor.

$$\nabla \cdot \boldsymbol{R} = \partial_j \langle u_j u_i \rangle \tag{2.29}$$

Derivation of the transport equation for the Reynolds stress tensor can be found in Durbin [145]. Classification of RANS models is regularly presented in terms of how much effort is undertaken (i.e. how many transport equations are used) to model the Reynolds stress tensor. For rotor aerodynamics, one and two equation RANS models are used frequently in the literature. Such models depend on the Boussinesq, or linear eddy-viscosity, hypothesis (EVH) shown in equation 4.1 for closure of equations 2.27 and 2.28.

$$\boldsymbol{R} = \langle u_j u_i \rangle = -2\nu_T S_{ij} + \frac{2}{3} \delta_{ij} k \tag{2.30}$$

In this equation, ν_T is the eddy viscosity, S_{ij} is the symmetric part of the velocity

gradient tensor, and the second term on the RHS is the non-deviatoric part of $\boldsymbol{R}$ that is generally subsumed by the pressure term.

Rethoré, Sørenson, and Bechmann [146] recount the three major assumptions of EVH from the Bernard and Wallace text:

1. For a given flow resolution, a particle is expected to conserve its velocity over the turbulent time-scale τ

2. τ is large enough that fluctuations at current time t are uncorrelated with fluctuations at $t - \tau$

3. The mean velocity over the path a particle travels during τ changes linearly

The work of Rethoré et al. clearly shows that for wind turbine flows, the eddy-viscosity hypothesis overestimates the axial Reynolds stress in the vicinity of the rotor, due to incongruities with assumptions 1 and 3. They suggest the work of Jin and Braza (1994), and the use of vorticity in the turbulent kinetic energy (TKE) production term, as a possible partial remedy to these issues [146].

Despite the shortcomings of the linear eddy-viscosity hypothesis, several factors make RANS simulation attractive for blade-resolved wind turbine research. This is reflected in the literature. Table 2.1 shows a non-exhaustive but representative list of RANS simulations of wind turbine rotors with resolved blades.

In sum, these papers generally show good agreement with their respective experimental data comparisons, however certain challenges remain. Comparisons to the NREL Phase VI experiment, at 10 m/s inflow, show the importance of turbulence

Research Team	Year	Comparison	Turbulence Model
Sørensen and Hansen [147]	1998	Nordtank 500/41	$k-\omega$ SST
Duque et al. [148]	1999	NREL Phase VI	Baldwin and Barth
Sørensen et al. [149]	2002	NREL Phase VI	$k-\omega$ SST
Xu and Sankar [86]	2002	NREL Phase VI	Spalart-Allmaras + Vortex Method
Chaviaropoulos et al. [150]	2003	NREL Phase II	$k-\omega$,$k-\omega$ SST,$k-\varepsilon$, SA
Pape and Lecanu [23]	2004	NREL Phase VI	$k-\omega$ SST
Sørensen and Johansen [151]	2007	Upwind	$k-\omega$ SST
Potsdam and Mavriplis [152]	2009	NREL Phase VI	Spalart-Allmaras vs. Baldwin-Barth
Zahle et al. [153]	2009	NREL Phase VI	$k-\omega$ SST
Sørensen [154]	2009	NREL Phase VI	$k-\omega$ SST + Transition
Bechmann et al. [155]	2011	MEXICO	$k-\omega$ SST
Li et al. [142]	2012	NREL Phase VI	$k-\omega$ SST vs. DES
Lanzafame et al. [156]	2013	NREL Phase VI	$k-\omega$ SST
Quon et al. [157]	2013	NREL Phase VI	Hybrid URANS-LES-VV
AbdelSalam and Ramalingam [158]	2014	Danwin 180 kW	$k-\varepsilon$ + Crepso + El Kasmi
Carrion et al. [159]	2015	MEXICO	$k-\omega$
Guntur and Sørensen [160]	2015	MEXICO	$k-\omega$ SST
Song and Perot [161]	2015	NREL Phase VI	Spalart-Allmaras
Make and Vaz [162]	2015	MARIN	$k-\omega$ SST vs. Spalart-Allmaras
Troldborg et al. [144]	2015	NREL 5MW	$k-\omega$ SST vs. DES

Table 2.1: Full-rotor resolved-blade RANS simulations

modeling, in particular the ability of a model to capture transition and separation. Sørensen [154] highlights this challenge showing side-by-side comparisons using fully turbulent and transition model approaches.

With few exceptions, the simulations in table 2.1 generally use steady inflow with a constant turbulence intensity. Another result of Troldborg et al. [144] highlights that full rotor RANS and DES simulations have significantly different far wake stuctures dependent on the inflow.

2.4.5 Practical Issues

Wind turbine flows present several practical challenges that full Navier-Stokes simulations must address. High Reynolds number regimes and scale separation

make mesh generation and grid size challenging. Rotational motion infers either mesh motion or rotating reference frames. Realistic approximation of the atmospheric boundary layer infers challenges with the modeling turbulent inflow and turbulence modeling.

2.4.5.1 Meshing for Rotating Machinery

Modeling the rotation of a wind turbine rotor requires a choice between several meshing options in CFD. The simplest method involves applying a rotating reference frame to a static mesh or mesh subsection, which is only applicable in steady-state simulations. More complicated, and the method used in OpenFOAM, is that of mesh regions that rotate relative to each other, using interface mapping algorithms to connect the meshes at each timestep. More complicated still is the method of overset grids, used in several simulations in table 2.1. Overset meshing involves generating an overlapping grid for each component and recalculating a new additive grid at each timestep.

2.4.5.2 Software and Parallelization

It is not uncommon for resolved blade rotor simulations, or LES simulations to number in the tens or hundreds of millions of grid points. In order to efficiently solve such large domains, software packages must efficiently handle parallelization. Generally this is handled by software libraries with an underlying technology called the Message Passing Interface (MPI).

2.4.5.3 Representative Data For Wind Simulation

Atmospheric flow velocities in the vicinity of the earth's surface are inherently chaotic. Large scale variations in surface topology and roughness can significantly alter flowfield characteristics. Thorough assessment of the wind resource at a specific site can involve several months or years of data collection and analysis. The wind energy research community has put significant effort into properly representing wind fields for simulations of varying levels of complexity.

At a basic level, probability distributions such as the Rayleigh, Weibull, or Gumbel can be used directly for generalized statistical predictions of wind turbine power output as discussed in [27].

Log and power law representations are used to mimic atmospheric flow and incorporate varying degrees of ABL roughness in simulations [27].

The wind field simulation of Mann [163] aims to represent turbulence such that second-order statistics like cross-spectra and variance match that of real atmospheric conditions.

Troldborg et al. [144] shows the importance of turbulence inflow conditions. Significant differences in the wake exist when using short inlet length and averaged turbulence vs. realistic (i.e. coherent structures) turbulence. Their work uses the Mann algorithm transformed into a time series by way of Taylor's frozen turbulence hypothesis.

Several works attempt to include representations, empirical data, or mesoscale

models of the atmospheric boundary layer (ABL) [123, 127, 128, 131, 132]. Vertical entrainment in the ABL is an important topic affecting the performance of wind farms [122, 164].

2.4.5.4 Turbulence Models and Modeling

Both the table on page 1026 of the Carrión paper [159] and table 2.1 in this work show significant bias towards the $k-\omega$ SST turbulence model over other RANS models for exact geometry rotor simulations. DES and LES, with better overall representation of the Reynolds stresses, are seeing more use in exact geometry rotors [130, 142, 144, 165].

2.4.6 Going Forward

As an alternative to solving the Navier-Stokes equations for macroscopic variables, work published in the past year has shown the viability of solving the Lattice-Boltzmann equations (LBE) in the context of wind turbine simulations [166, 167]. Wood and Deiterding predicted the power output of a Vestas turbine to within 5% of manufacturer specifications [166]. Several advantages, and some drawbacks, exist for simulations of this type. LBE is particularly suited to parallel computation as there is no elliptic pressure equation requiring communication from all parts of the mesh, only nearest neighbors are required [166].

Despite a large cell count, $\sim 1.4e+8$ cells, computations in [166] ran on 288 cpu cores and took a mere 38.5 hours wall clock time to advance the wake 10 seconds. This is a significant advantage compared to NS methods, that even given

an optimal computational environment and parallel distribution, might take on the order of days per rotor revolution of a single rotor [161, 162].

CHAPTER 3

SHS, CFD, AND SURFACE ROUGHNESS

In recent years, superhydrophobic surfaces have seen increased study both experimentally [16, 168, 169] and computationally [170–174]. As discussed in the introduction, a superhydrophobic surface repels water droplets due to micron scale surface features that increase a droplet's equilibrium contact angle θ_e. This angle is formed between the line tangent to the liquid-vapor interface and the line tangent to the solid-liquid interface, and is independent of droplet size [175]. θ_e is defined by Young's equation (equation 3.1) where the γ terms are interfacial surface tension forces between solid (S), liquid (L), and vapor (V) phases.

$$\cos\theta_e = \frac{\gamma_{SV} - \gamma_{SL}}{\gamma_{LV}} \tag{3.1}$$

Conventionally, $\theta_e < 90$ is referred to as hydrophilic and $\theta_e > 90$ as hydrophobic. For surfaces that contain asperities, or roughness elements, two extreme cases of wetting exist. If the liquid penetrates all the surface asperities, fully wetting the surface, it is referred to as the Wenzel state. If the liquid rests on top of the asperities, it is referred to as the Cassie state. Shirtcliffe discusses the ramifications of these states and shows derivations for modifications to Young's equation for their representation [175].

It is important to note that equation 3.1 implies a single angle at which equi-

librium exists, however on real surfaces, droplet stability can exist at a range of angles. This range can depend on several factors including surface heterogeneity, surface tilt, or changing volume of a droplet [175]. The mechanics of droplet interactions with superhydrophobic surfaces are beyond the scope of this work, however several reviews exist in the literature [12, 175–180].

3.1 Description of Superhydrophobic Surfaces

Given the abundance of literature showing the water and ice repellent properties of superhydrophobic surfaces, it is prudent to first broadly define a set of geometric and topological properties for SHS that will be useful in representing SHS in simulations. Celia et al. [181] describe a significant number of processes to produce superhydrophobic surfaces, showing both heterogeneous and homogeneous results. Vorobyev and Guo [168] produced etched metal SHS using femtosecond lasers, creating surface asperities in platinum approximately $100\mu m$ apart and $75\mu m$ deep. Daniello et al. [182] used both $30\mu m$ and $60\mu m$ ridges in their study of SHS drag reduction in turbulent channel flow. Jung and Bhushan show a simulated shark skin with with a height of $200\mu m - 500\mu m$ and pitch of $100\mu m - 300\mu m$. Bhushan et al. [183] state that for circular pillars and characteristic droplet size of 1mm, asperities of $30\mu m$ height, $15\mu m$ diameter, and $130\mu m$ pitch are ideal. Guo et al. [177] show that lotus leaf surfaces contain macro-asperities approximately $3\mu m - 10\mu m$ combined with wax crystal micro-asperities on the order of $70nm - 100nm$

Öner and McCarthy [184] published an analysis of effects of topography length scales on surface wettability. Their research shows that the maximum asperity width (square) to support SHS behavior is approximately $32\mu m$ and that contact angle is independent of the studied asperity height range of $20\mu m - 140\mu m$.

For the purposes of this work, SHS is defined as surface covered in regularly shaped asperities, approximately $32\mu m$ in diameter (or square), at a height of approximately $30\mu m - 140\mu m$.

3.2 Smooth Wall Turbulent Boundary Layer

Surface asperities, or surface roughness elements, have a significant impact on the wind turbine boundary layer as discussed in [185], though before addressing their impact, it is important to understand the smooth wall turbulent boundary layer. Fully turbulent flow in the proximity of a solid boundary follows a predictable flow pattern in the vicinity of that boundary as a result of the no-slip boundary condition and turbulence mechanisms. There are three distinct layers, the viscous sub-layer, the log-layer, and the velocity-defect layer, each having a "buffer zone" between them.

Figure 3.1 shows smooth wall velocity profile wherein both quantities are normalized as shown in 3.2, where ν is the kinematic viscosity and u_τ is the "friction velocity."

$$y^+ = y\frac{u_\tau}{\nu} \qquad\qquad u^+ = u\frac{u_\tau}{\nu} \tag{3.2}$$

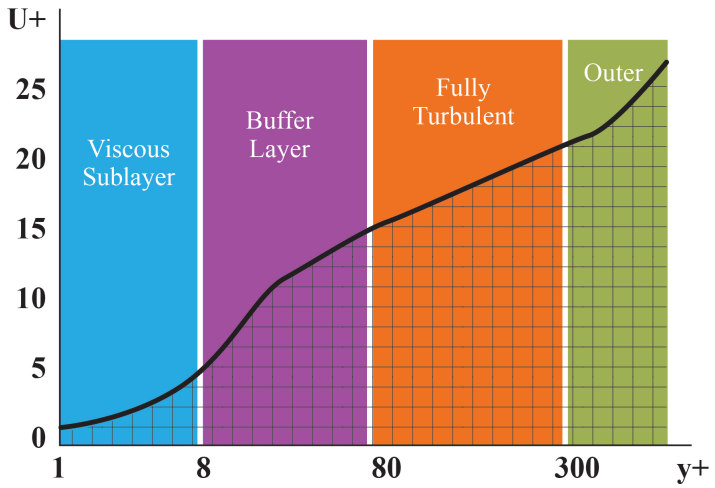

Figure 3.1: Example of the layered structure of boundary layer flow. The log-layer is labeled as "Fully turbulent" and the velocity-defect layer is in the "Outer Region"

$$u_\tau = \sqrt{\frac{\tau_w}{\rho}} \tag{3.3}$$

τ_w represents shear stress at the wall, and may be calculated given a known velocity gradient near the wall, or by knowing the coefficient of friction, which can be estimated using one of many power-law like equations.

$$\tau_w = \mu \frac{\partial u}{\partial y} = \frac{1}{2} c_f \rho U_{rel}^2 \tag{3.4}$$

μ in the above equations is the dynamic viscosity $\mu = \rho\nu$. For estimating the coefficient of friction c_f, the 1/7 power law profile is valid for flows with $Re < 10^6$ but the Schlicting Law can be used up to $Re < 10^9$ [186].

$$c_f = (2\log_{10}(Re) - 0.65)^{-2.3} \tag{3.5}$$

Hoffman's CFD textbook (Vol 3 pg 5) defines the regions represented in figure 3.1 as such:

$$y^+ < 2 \sim 8 \Longrightarrow \text{viscous sublayer} \tag{3.6}$$

$$2 \sim 8 < y^+ < 2 \sim 50 \Longrightarrow \text{buffer zone} \tag{3.7}$$

$$y^+ > \sim 50 \Longrightarrow \text{fully turbulent zone (log layer)} \tag{3.8}$$

As is apparent by its name, the viscous sublayer is dominated by viscosity effects. The buffer zone between the viscous sublayer and the log layer is responsible for the bulk of the turbulent generation [187]. Roughness elements larger than the viscous sublayer interfere with turbulent generation in the buffer layer and alter the curve in the log layer [187]. The log-layer is defined in equation 3.9 from Cebeci and Smith [188] (among many other sources) which is commonly referred to as the "law of the wall",

$$u^+ = \left(\frac{1}{\kappa}\right) \ln y^+ + B, \tag{3.9}$$

where the Von Kármán constant $\kappa \approx 0.41$, and $B \approx 5.1$ for smooth walls.

3.3 Nikuradse and ESG

The representation of surface asperities, or surface roughness, is clearly of importance to practitioners of CFD due to impacts on wall bounded flows. Surface roughness research has roots in the middle 19th century in the works of Hagen and of Darcy [187]. In 1933, J. Nikuradse, a student of Ludwig Prandtl, set out to quantify the effects of both fine and coarse roughness on pipe flow at all Reynolds numbers. In so doing, he developed a pipe roughening method using sieved sand grains and an alteration to equation 3.9 to account for roughness effects of regularly sized roughness elements [189].

Nikuradse found the rough wall log layer to be [187]:

$$u^+ = \left(\frac{1}{\kappa}\right) \ln\left(y/k_s\right) + 8.5 + \frac{\Pi}{\kappa} W(y/\delta) \tag{3.10}$$

The third term on the left hand side is the contribution of the outer layer flow, and is usually negligible below $y/\delta \approx 0.15$ [187]. Equation 3.10 can also be expressed as a smooth wall log layer plus a roughness function that represents the downward shift in the velocity curve [190]. This formulation was introduced independently by Clauser and by Hama as discussed in [191].

$$u^+ = (\frac{1}{\kappa}) \ln y^+ + B + \Delta B(k_s^+) \tag{3.11}$$

$$k_s^+ = \frac{k_s u_\tau}{\nu} \tag{3.12}$$

Roughness regimes are generally categorized using k_s^+. With values varying somewhat in the literature, the three regimes are hydrodynamically smooth ($k_s^+ \leq 2.25$), transitional ($2.25 < k_s^+ \leq 90$), and fully rough ($k_s^+ > 90$).

In considering a method for estimating k_s (sandgrain roughness height) in equations 3.10 and 3.12, it is important to note that Nikuradse's method for pipe roughening. In order to maintain a constant r/k, Nikuradse sieved ordinary building sand and then measured several hundred individual grains using a Zeiss thickness gauge accurate to 0.001 mm [189].

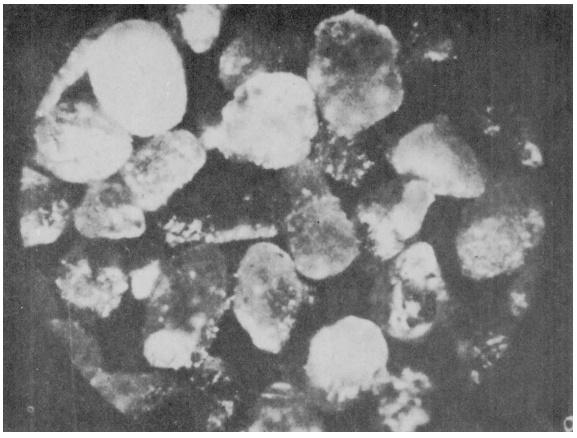

Figure 3.2: Nikuradse's "microphotograph" of sandgrain pipe roughness [189]

Figure 3.3 shows an idealized version of k_s as the diameter of a closely packed sphere. However, the true effect on the flow may be closer to an outward extension of the boundary by r_s plus a roughness effect with a length scale also on the order of r_s.

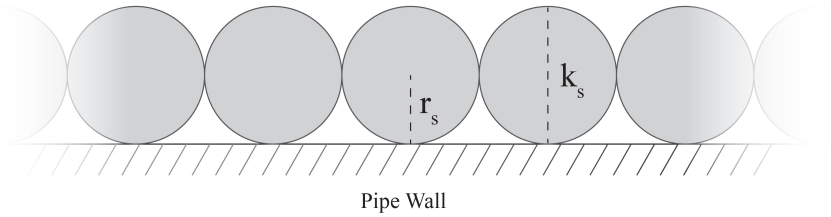

Figure 3.3: Idealized version of Nikuradse's sandgrain pipe roughness

Regardless of the "proper" flow length scales, Nikuradse's k_s is a "common-currency" approach to roughness height. Nikuradse measured k_s and correlated it to a certain ΔB. More recently, researchers have developed equivalent sand grain (ESG) correlation functions to approximate the effect of varied roughness topologies in terms of Nikuradse's k_s.

3.3.1 Relation between ESG and actual surface roughness

As a common-currency measure for roughness when implementing roughness models in CFD, "equivalent sand-grain height" (ESG or k_s) height produces the same roughness function as Nikuradse's uniform sand grain in the "fully-rough" range [187, 192, 193]. Flack and Schultz [193] give correlation functions from Dvorak, Dirling, Sigal and Danburg, and van Rij et al. as well as developing a new correlation function, all relating various topological roughness parameters to the k_s value. As an example, the Dirling correlation is given in equations 3.13 to 3.15.

$$\Lambda = \left(\frac{d}{h_r}\right)\left(\frac{A_f}{A_s}\right)^{-4/3} \tag{3.13}$$

$$\frac{k_s}{h_r} = 0.0164\Lambda^{3.78}, \Lambda \leq 4.93 \tag{3.14}$$

$$\frac{k_s}{h_r} = 139\Lambda^{-1.90}, \Lambda > 4.93 \tag{3.15}$$

Dirling takes topological features of roughness and translates them to equivalent sand grain roughness, where h_r is the mean roughness height, k_s is the ESG height, d is the mean distance between roughness elements i.e. $d = \sqrt{sa/n}$ (sa = surface area and n is number of elements), A_f is the surface area of a roughness element projected normal to the flow, and A_s is the wetted surface area of a roughness element directly in the path of upstream flow.

The Flack and Schulz correlation in [193] uses only two values, the RMS height of the roughness elements and the skewness of the roughness surface elevation probability density function. They reviewed a large amount of roughness scaling parameters for that work and found those two had the highest correlative and therefore predictive value.

3.4 Surface displacement vs. Roughness

As shown in figure 3.3, tightly packed roughness elements have two significant effects, displacing the effective surface by a radius of the element, and introducing hills and valleys (also with a length scale of the radius of the element) to which the flow must adapt. However, the tightly packed spheres approximation represents

only one specific type of shape deformation that a surface may experience.

3.4.1 Environmental Accumulations

Wind turbines are installed in all manner of environments, and as such are exposed to many stochastic environmental effects. Insect accumulation, dirt accumulation, and ice buildup are addressed here.

3.4.1.1 Insects and Dirt

Insects killed by fast moving objects can become attached to the surface of that object becoming a deformation seen by the airflow. The same can happen with dust and dirt in locations with air that contains a substantial particulate count. It is these types of accumulation that were studied in the Ohio State University study on roughness using the s809 airfoil [21].

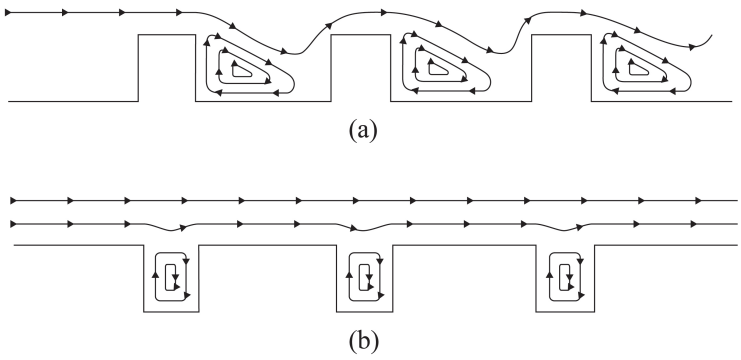

Figure 3.4: Illustration of a)"k" type roughness b) "d" type roughness

Figure 3.4 shows an important distinction in roughness topology. As discussed in Jimenez [187], in the limit of $k^+ >> 1$, k_s should be proportional to the mean roughness dimensions, e.g. "k". However, it was shown by Perry that certain

topologies were proportional to the boundary layer height δ, e.g. "d" [187].

As shown in figure 3.4, k-type roughness elements produce recirculation regions that re-attach upstream of the next element, with each element fully exposed to the flow. With d-type roughness elements, recirculation regions tend to shelter roughness elements such that the outer flow is much less affected.

Jimenez notes that surfaces with element spacing on the order of (greater than) 3-4 times their height k tend to act like k-type rough surfaces [187]. Insect accumulation, in all but extreme cases, is an example of k-type roughness.

3.4.1.2 Ice Buildup

Ice accumulation is a special case, given that effective surface displacement and roughness can both exist simultaneously depending on the specifics of the ice growth.

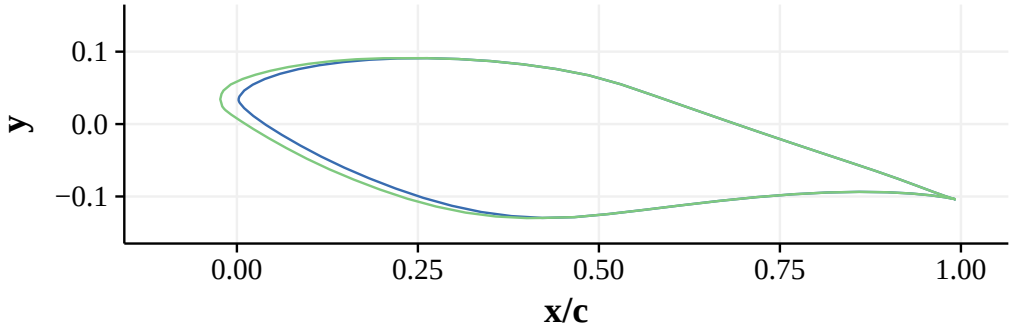

Figure 3.5: Example modeled ice buildup on the s809 airfoil. Uses the steady method of Myers and Charpin [194]; (——) No ice buildup, (——) Ice buildup

Early work by Ackley and Templeton [195] addressed the modeling of ice accretion on a helicopter rotor. Subsequent work is relevant across fields, with many of

these papers being specific to wind turbine ice accretion [194, 196–210]. Significant work is contributed by the NASA Glenn research center, and their software code LEWICE [211], which is a time stepping ice accretion code based on the model of Messinger.

3.4.2 Pitting/Scraping

Manufacturing processes, environmental scraping, and particulate concentrations in the air may result in scraped or pitted surfaces. This type of roughness can generally be classified as d-type roughness until it reaches a critical mass wherein there are more scrapes or pits than not. This work is not specifically looking a d-type roughness, however in the equivalent sand grain approach it is likely a matter of using a representative correlation to find a k_s value and $f(k_s^+)$ that will work for a given surface. Ligrani and Moffat [212] consider roughness to be d-type when the flow properties scale on pipe diameter rather than roughness parameters.

3.4.3 Modeling Issues

When developing CFD models for wind turbine airfoils and blades while aiming to model the effects of small scale roughness, it is important to note the scale to which linear approximations are mismatched to the curves they represent. Like the exaggerated image in figure 3.6, choice of spline and linear resolution can significantly impact the airfoil model's surface smoothness.

Figure 3.7 shows how different resolutions of linear representation can effect the top side of an airfoil curve. Clearly figure 3.7a shows that a simple 150 point linear

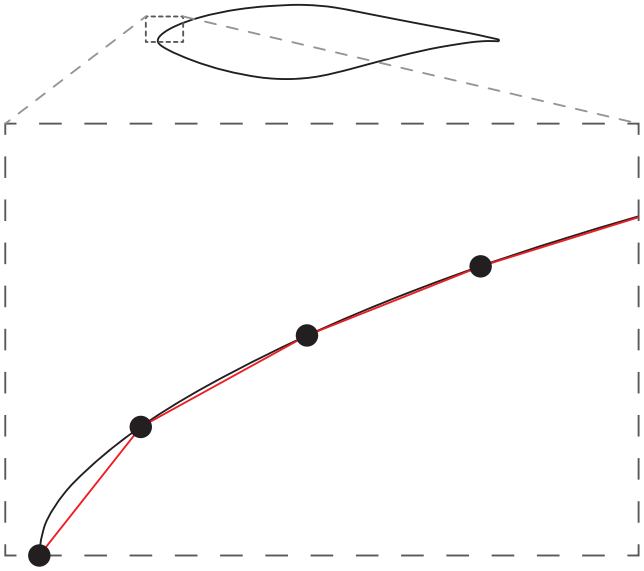

Figure 3.6: Illustration of linear representation of a curved airfoil surface. Shows (exaggerated) error that could be on the order of roughness without careful modeling practices

approximation cannot represent the curve without error around or above the SHS element height. The 150 point linear reconstruction of a 200 point spline (similar to what might happen in a solid body model) shows a better initial reconstruction and most error below the scale of a superhydrophobic surface element. Figures 3.7c and 3.7d show that having a better spline initial approximation and more points in the linear approximation can reduce error even farther below the scale of a superhydrophobic surface element.

3.5 Application of Surface Roughness to CFD simulations

The literature contains several reviews describing general effects of roughness [185, 187, 213–215]. Sagol's review [185] is specifically focused on wind turbines, and notes that on rough surface airfoils, researchers find two general effects as com-

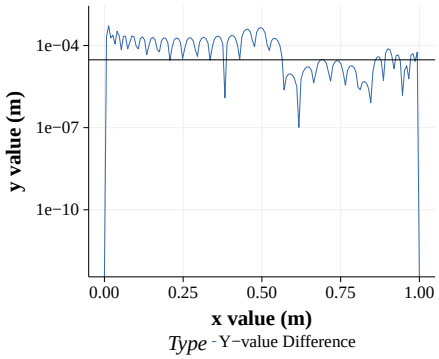

(a) *Magnitude of difference between y-values of 150 point linear and spline interpolations of s809 airfoil top surface from 33 original points*

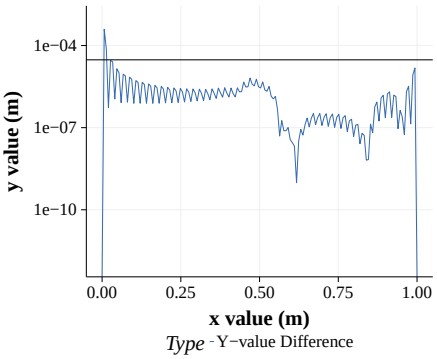

(b) *Magnitude of difference between y-values of 150 point linear and spline interpolations of s809 airfoil top surface from an initial 200 point spline*

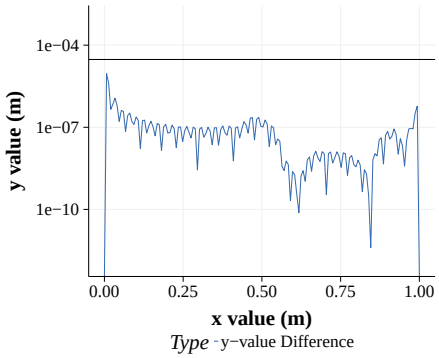

(c) *Magnitude of difference between y-values of 150 point linear and spline interpolations of s809 airfoil top surface from an initial 1000 point spline*

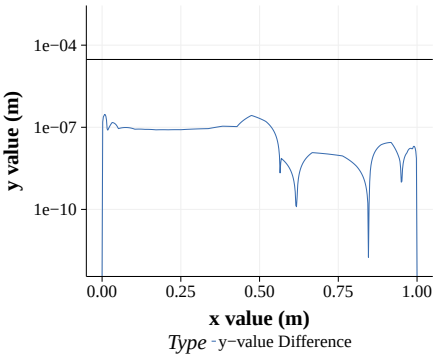

(d) *Magnitude of difference between y-values of 500 point linear and spline interpolations of s809 airfoil top surface from an initial 1000 point spline*

Figure 3.7: Linear vs. spline interpolation of a 2D s809 airfoil top surface where the black line is the minimum height of an SHS element of 30 microns

pared to smooth airfoils: a laminar-to-turbulent transition farther upstream and a prolonged period of transition. Sagol [185] also highlights research results showing that roughness effects are more impactful near the leading edge of an airfoil, but that full roughness on an airfoil increases drag and decreases lift more than roughness only on the leading edge.

3.5.1 General Effects of surface roughness on turbulence parameters

Flack and Schultz [191] provide ample discussion of rough wall turbulent boundary layer effects. Important to this discussion is the concept of wall similarity. Simply put, wall similarity is the concept that roughness effects are confined to the inner boundary layer, having little to no effect on the outer region. The roughness function ΔB is dependent on mean flow similarity [191]. The experiments in [191] support the notion of wall similarity in the mean flow, Reynolds Stresses, and turbulence statistics for 3D roughness (i.e. square posts and the like) and 2D roughness (i.e. ridges) at high Reynolds numbers. Orlandi [216] shows a proportionality between wall-normal Reynolds stress and the roughness function.

3.5.2 Direct numerical Simulations of Roughness Elements

Given the difficulty of near-wall experimental measurement, and in support of rough wall experiments such as [191], DNS has given researchers significant insight into the nature of rough wall flows. The nature of superhydrophobic surface drag reduction has been discussed [170, 172, 173, 217, 218].

3.5.3 Common practices for including surface roughness in turbulence models

Turbulence models are conventionally classified by their applicability close to walls. High Reynolds number models do not resolve the boundary layer, relying on a

first cell height of $30 \lesssim y^+ \lesssim 100$ and an imposed functional representation, or "wall function", for flow incident to the wall. Low Reynolds number models resolve boundary layer flow and rely on first cell heights on the order of $y^+ \approx 1$. These classifications are somewhat unfortunate, as neither model type is limited to high or low Reynolds number flows, and it is common practice to choose a "low" Reynolds number turbulence model when needing to resolve the boundary layer at any Reynolds number.

As discussed in the introduction to Aupoix [219] there are three commonly used methods for the inclusion of surface roughness in turbulence modeling. The first method really comes down to not including roughness in the turbulence model at all. With enough computational resources, one can incorporate 2D or 3D structures on the surface of a model that are representative of the roughness elements. The fluid equations are solved without modification, though to create and solve a resolved boundary layer on so many roughness elements is complex and resource intensive. Another method discussed by Aupoix [219] is the "discrete element approach" which is a globally averaged application of roughness that modifies the mean flow equations. Readers can check [219] and the cited references in that work for more background on the method. The last approach, and the approach taken in the work, is the "equivalent sand grain" method, in which correlations are used to map properties of the roughness elements into a single value k_s which represents the height of a sand grain from Nikuradse's experiments [189] that would cause the velocity shift desired. Modifications are made to the boundary conditions of the turbulence model, increasing the strength of turbulence

near the wall, causing a stronger drag force and reduction of velocity in the log layer. The equivalent sand grain approach can be applied though wall functions or directly as Dirichlet boundary conditions.

3.5.3.1 Wall Functions

High Reynolds number models use wall functions to calculate boundary layer flow that spans the first cell from the wall. To include roughness, such models explicitly include a ΔB, as in equation 3.11, that includes the effect of ESG roughness. As a practical example, Fluent-6.3 and OpenFOAM 1.6-ext both use equations 3.16 - 3.18 to determine the roughness function ΔB.

For $k_s^+ \leq 2.25$:

$$\Delta B = 0 \tag{3.16}$$

For $2.25 < k_s^+ \leq 90$:

$$\Delta B = \frac{1}{\kappa} \ln \left[\frac{k_s^+ - 2.25}{87.75} + C_s k_s^+ \right] \times \sin \left\{ 0.4258 (\ln(k_s^+) - 0.811) \right\} \tag{3.17}$$

For $k_s^+ > 90$:

$$\Delta B = \frac{1}{\kappa} \ln(1 + C_s k_s^+) \tag{3.18}$$

Recent work on roughness inclusive wall functions has been carried out by Apsley [220] and Suga et al. [221].

3.5.3.2 Resolved Boundary Layer

Efforts have been made by several researchers to include roughness in low Reynolds number turbulence models [192, 222–234]. Vijiapurapu and Cui [235] compared RANS models and LES for modeling roughness effects in a circular pipe. Patel and Yoon [236] compared rough wall $k-\omega$ and $k-\epsilon$ models, showing that the $k-\omega$ model fared well over a wide range of Reynolds numbers. Lu and Liou [237] compare the low-Reynolds number rough wall versions of $k-\varepsilon$ of Zhang et al. to that of Foti and Scandura, which both modify the damping functions to attain a roughness effect. They found Zhang et al. to suffer at high roughness heights and neither model to accurately predict turbulent kinetic energy or skin friction. Durbin [224] uses a two-layer $k-\epsilon$ model with modifications to the mixing length formulation and the boundary condition on k. His method depends on a calibration with experimental data for the associated roughness.

Significant effort has been put into equivalent sand grain based roughness boundary conditions for the $k\omega - SST$ turbulence model. Knopp et al. [228] build on the work of Hellsten et al. [227] and Patel and Yoon [236], developing a new $k-\omega$ roughness adaptation that avoids the strict grid requirements of Wilcox [227].

Table 3.1 shows a sampling of roughness inclusive RANS methods in the literature.

Reference	Boundary Conditions	Notes
Durbin et al. [224]	$k_w = \frac{{u_\tau}^2}{\sqrt{C_\mu}} min\left(1, \left(\frac{r^+}{90}\right)^2\right)$ $\varepsilon_w = \frac{{u_\tau}^4}{\nu C_l A_\varepsilon \sqrt{C_\mu}} \left(\frac{r^+}{90 y_0}\right)^2$	Uses calibration scheme to solve for y_0
Blocken [190]	$k_w = \frac{{u_\tau}^2}{\sqrt{C_\mu}}$ $\varepsilon_w = \frac{u_\tau^3}{\kappa y_w}$	Wall function approach
Tarada [232]	$k_w = 0$ $\tilde{\varepsilon}_w = 0$	Adds drag model to momentum equation
Zhang, Faghri, and White [234]	$k_w = 0$ $\varepsilon_w = \frac{\partial^2 k}{\partial y^2}$	Roughness is modeled in f_μ and f_1 functions
Knopp, Eisfeld, Calvo [228]	$k_w = \frac{{u_\tau}^2}{\sqrt{C_\mu}}$ $\omega_w = \frac{u_\tau}{\sqrt{C_\mu}\kappa d_0}; d_0 \approx 0.03 k_r$	Blending functions are used to match with smooth wall BCs
Wilcox [228]	$k_w = 0$ $\omega_w = \frac{u_\tau^2}{\nu} S_R; S_R = f(k_r^+)$	
Hellsten & Laine [227]	$k_w = 0$ $\omega_w = \frac{u_\tau^2}{\nu} S_R; S_R = f(k_r^+)$	Added correction to turn off SST limitation in the roughness layer
Langel et al. [229]	$k_w = 0$ $\omega_w = \frac{u_\tau^2}{\nu} S_R; S_R = f(k_r^+)$	Use Langtry-Menter transition model inside BL
Aupoix & Spalart [223]	Boeing: $\frac{\partial \tilde{\nu}}{\partial n} = \frac{\tilde{\nu}}{d}$ Onera: $\tilde{\nu}_w^+ = f(h_s^+)$	

Table 3.1: Roughness inclusion in RANS modeling literature

CHAPTER 4

TURBULENT POTENTIAL MODEL AND MODIFICATIONS

Industry workhorse turbulence models, such as **Spalart-Allmaras**, $\boldsymbol{k\omega}$-$\boldsymbol{SST}$, and $\boldsymbol{v^2f}$ close the momentum equation by formulating the Reynolds stress tensor analogous to the viscous stress. An "eddy-viscosity" term, ν_t, is the primary output of such models. If the ν_t term appears only to the first power, it is known as a "linear eddy-viscosity" model. Several alternatives exist for avoiding the linear eddy-viscosity hypothesis,

$$\boldsymbol{R} = \overline{u_j u_i} = -2\nu_t S_{ij} + \frac{2}{3}\delta_{ij}k \tag{4.1}$$

where k is the turbulent kinetic energy and

$$S_{ij} = \frac{1}{2}(\partial_j \boldsymbol{U_i} + \partial_i \boldsymbol{U_j}) = \frac{1}{2}(\nabla \boldsymbol{U} + \nabla \boldsymbol{U}^T). \tag{4.2}$$

These include formulating eddy-viscosity as a non-linear cubic term [238], or modeling the full Reynolds stress tensor as in the many RSTM RANS models. The Turbulent Potential (TP) model [239] is another alternative that uses the RANS equations but avoids the linear eddy-viscosity hypothesis, while approaching the accuracy of RSTM models at a computational cost and flexibility closer to 2-

equation models.

The Turbulent Potential model was first suggested by Perot and Moin [240] along with an initial proposal for the form of the transport equations. The theoretical basis for the TP model starts with the RANS equations.

$$\partial_t \boldsymbol{U_i} + \boldsymbol{U_j}\partial_j \boldsymbol{U_i} = -\frac{1}{\rho}\partial_i p + \nu\nabla^2 \boldsymbol{U_i} - \partial_j \overline{u_j u_i} \tag{4.3}$$

$$\partial_i \boldsymbol{U}_i = 0 \tag{4.4}$$

The TP model solves 4.3 using 6 transport equations (k,ε,ϕ,ψ_1,ψ_2,ψ_3), though in 2 dimensional flow, $\psi_1 = \psi_2 = 0$ so some savings can be found. Several versions of transport equations have been published in the literature, along with several validations based on experimental and DNS data [239–244]. The Turbulent Potential model is implemented in OpenFOAM for this work. This implementation is validated against DNS channel data, impinging jet experiments, and smooth and rough airfoil data.

Perot and Moin [240] provide the basic rationale and machinery of the Turbulent Potential Model. Unlike many RANS models, the eddy-viscosity hypothesis is not used in favor of directly relating the divergence of the Reynolds stress tensor to the mean flow equations.

Equations 4.3 and 4.4 represent RANS momentum and continuity respectively,

where $\nabla \cdot \boldsymbol{R} = \partial_j \overline{u_j u_i}$ is the effect of the fluctuating velocity in the form of the divergence of the Reynolds stress tensor. It can be shown that this divergence term can be mathematically transformed using the Helmholtz theorem [240]. The divergence term is treated as a body force and the Helmholtz theorem is applied with the gauge constraint $\nabla \cdot \boldsymbol{\psi} = 0$:

$$\boldsymbol{f} = \nabla \cdot \boldsymbol{R} = \nabla\phi + \nabla \times \boldsymbol{\psi} \tag{4.5}$$

The divergence of the Reynolds stress tensor is simply the gradient of a scalar variable plus the curl of a vector variable, and these terms can be modeled using theory akin to that of full Reynolds stress transport models. The relationship between the potentials and the Reynolds stress tensor is elliptic,

$$\nabla^2\phi = \nabla \cdot \nabla \cdot \boldsymbol{R} \tag{4.6}$$

$$\nabla^2\boldsymbol{\psi} = -\nabla \times \nabla \cdot \boldsymbol{R} \tag{4.7}$$

But in situations with a single direction of inhomogeneity in the turbulence such as channel flow or free-shear flows, these relationships simplify to

$$\phi = R_{22} \tag{4.8}$$

$$\boldsymbol{\psi} = [-R_{32}, 0, R_{12}] \tag{4.9}$$

where the 2 direction is the direction of inhomogeneity.

From this 1D case, it is seen that ϕ is related to the fluctuations along the direction of turbulence inhomogeneity that physically produce turbulent mixing, and that $\boldsymbol{\psi}$ is related to the turbulent shear stresses.

Using $\nabla\phi + \nabla \times \boldsymbol{\psi}$ to represent $\nabla \cdot \boldsymbol{R}$ is exact and affords modeling opportunities not available when using the Boussinesq (eddy-viscosity) hypothesis, shown in equation 4.1. The TPM retains all of the physics that is lost when the eddy viscosity hypothesis directly relates the Reynolds stresses to the velocity gradient tensor. Eddy viscosity models are geared towards formulating a scalar ν_t, some representations of which can be rather complex. There is a significant range of flow scenarios where the equilibrium eddy viscosity assumption is known not hold irrespective of the complexity of ν_t or the eddy viscosity expression.

The turbulent potentials can be added to many other models in order to replace the eddy-viscosity relation. This work happens to rely on k and ε as supporting equations, however there is no intrinsic reason why other length or time scales (like a $k - \omega$ model) can not be used.

TPM complexity is positioned between eddy-viscosity models and full Reynolds stress transport models. The TPM offers at least two distinct advantages over full RST models. By decoupling the tensor Reynolds-stress solution, the TPM

offers a more flexible and forgiving set of equations. The TPM also reduces computational cost, especially in 2D flows, when compared to a full Reynolds stress transport models. It can be useful to consider the TPM as an RST-like model that has been rotated into a coordinate system aligned with the dominant turbulence inhomogeneity. Homogeneous turbulence has no affect on the mean flow.

The Turbulent Potential Model, as used in this work, is represented by equations in appendix A and the antecedent statement of constants. Though the model looks like 4 transport equations, it is important to remember that the ψ/k equation is one equation in 2D and two equations (3 equations with a constraint) in 3D.

4.1 Production Discussion

The TPM uses a simplified turbulent kinetic energy production term (P) that is only exact in flows with a single direction of inhomogeneity. In more complex flows, missing components of the actual production will likely result in poor predictive capability in the model. A discussion is entertained here to explore the possibility of adding back some of the missing production terms. Prior to discussing simulations, some attention must pe paid to the formulation of the production term in the TP model. Based on the Reynolds stress transport equation, the production tensor is defined as [245]:

$$P_{ij} = -\overline{u_i u_k}\frac{\partial U_j}{\partial x_k} - \overline{u_j u_k}\frac{\partial U_i}{\partial x_k} \tag{4.10}$$

$$P_{11} = -2\overline{u_1 u_1}\frac{\partial U_1}{\partial x_1} - 2\overline{u_1 u_2}\frac{\partial U_1}{\partial x_2} - 2\overline{u_1 u_3}\frac{\partial U_1}{\partial x_3} \tag{4.11}$$

$$P_{22} = -2\overline{u_2 u_1}\frac{\partial U_2}{\partial x_1} - 2\overline{u_2 u_2}\frac{\partial U_2}{\partial x_2} - 2\overline{u_2 u_3}\frac{\partial U_2}{\partial x_3} \tag{4.12}$$

$$P_{33} = -2\overline{u_3 u_1}\frac{\partial U_3}{\partial x_1} - 2\overline{u_3 u_2}\frac{\partial U_3}{\partial x_2} - 2\overline{u_3 u_3}\frac{\partial U_3}{\partial x_3} \tag{4.13}$$

$$P_{12} = -\overline{u_1 u_1}\frac{\partial U_2}{\partial x_1} - \overline{u_2 u_1}\frac{\partial U_1}{\partial x_1} - \overline{u_1 u_2}\frac{\partial U_2}{\partial x_2} - \overline{u_2 u_2}\frac{\partial U_1}{\partial x_2} - \overline{u_1 u_3}\frac{\partial U_2}{\partial x_3} - \overline{u_2 u_3}\frac{\partial U_1}{\partial x_3} \tag{4.14}$$

If $k = \frac{1}{2}\overline{u_i u_i}$, it follows that the TKE production term $\mathcal{P} \equiv \frac{1}{2}P_{ii}$, which results in the definition for TKE production shown in equation 4.17.

$$\mathcal{P} = -\tfrac{1}{2}(\mathcal{P}_{11} + \mathcal{P}_{22} + \mathcal{P}_{33}) \tag{4.15}$$

Which for a flow with inhomogeneity only in the "2" direction and no flow in the "3" direction gives

$$\mathcal{P} = -\overline{u_1 u_2}\frac{\partial U_1}{\partial x_2}, \tag{4.16}$$

which is the primary production in the Turbulent Potential Model.

$$\mathcal{P} = -\tfrac{1}{2}(\mathcal{P}_{11} + \mathcal{P}_{22} + \mathcal{P}_{33}) = -\overline{u_i u_j}\frac{\partial U_i}{\partial x_j} \tag{4.17}$$

As is discussed in Pope [245], only the anisotropic components of $\overline{u_i u_j}$ affect production in incompressible flow because the velocity gradient tensor is traceless. The Reynolds shear stress and velocity gradients are predominantly opposite in sign (giving a positively signed P), however there is no intrinsic need for this to be so, and the production term can occasionally act as a sink.

Prior work on the Turbulent Potential Model shows that in flows with a single direction of inhomogeneity (such as plane channel flow), $\mathcal{P}$ is represented exactly by the following expression.

$$\mathcal{P} = \boldsymbol{\psi} \cdot \boldsymbol{\omega} \tag{4.18}$$

However in flows with multiple directions of inhomogeneity, turbulent generation through straining is left unaccounted for. Before going further, we define the rate of strain tensor $\mathbf{S}_{ij}$, equation 4.20, as the symmetric part of the velocity gradient tensor:

$$\frac{\partial \mathbf{U}_i}{\partial x_j} = \boldsymbol{S}_{ij} + \boldsymbol{\Omega}_{ij} \tag{4.19}$$

Where the following are definitions of those components:

$$\mathbf{S}_{ij} = \frac{1}{2}\left(\frac{\partial \mathbf{U}_i}{\partial x_j} + \frac{\partial \mathbf{U}_j}{\partial x_i}\right) \tag{4.20}$$

$$\mathbf{\Omega}_{ij} = \frac{1}{2}\left(\frac{\partial \mathbf{U}_i}{\partial x_j} - \frac{\partial \mathbf{U}_j}{\partial x_i}\right) \tag{4.21}$$

Equation 4.21 shows the rotation rate tensor. This tensor does not contribute to turbulence production, as the double inner product of a symmetric tensor with a skew-symmetric tensor is equal to zero.

Many RANS models use the production formulation shown in equation 4.22, which is a consequence of the eddy-viscosity theory. As shown in Sveningsson and Davidson [246], this model form of production needs realizability limits when used with the v^2f model and the situation is no different for the Turbulent Potential Model.

$$\mathcal{P} = 2\nu_T S_{ij} S_{ij} \tag{4.22}$$

$$|S| = |2S_{ij}S_{ij}|^{\frac{1}{2}} \tag{4.23}$$

In this work, a blended production model is tested in impinging jet flow. Equation 4.24 is based on the hypothesis that Reynolds shear stress and vorticity are

dominant modes of production in near-wall and shear layer regions, whilst everywhere else, shearing and straining production must both be present. The term α is necessarily equal to one at the smooth wall and 0.5 in isotropic, ($\phi/k = 2/3$), regions of the flow. Looking at a wide range of channel flow data [247], $180 < Re_\tau < 5200$, α is independent of turbulence Reynolds number.

$$\mathcal{P} = \alpha \boldsymbol{\psi} \cdot \boldsymbol{\omega} + (1 - \alpha) 2 \nu_T S_{ij} S_{ij} \tag{4.24}$$

$$\nu_T = C_\mu \frac{\phi k}{\varepsilon} \tag{4.25}$$

Figure 4.1 shows the exact production and production models 4.22 and 4.24 using the $Re_\tau = 590$ channel simulation described later in this manuscript. Figure 4.1a shows a green dashed line that has a significantly different shape than the others. This is the classic production model (eqn 25). Despite what looks like a significant discrepancy between the exact production and both the near-wall and peak behavior of the classic model (equation 4.22), the mean velocity results in Figure 4.1b show very little variation.

4.2 Turbulence Reynolds Number Dependence

The turbulence Reynolds number is a dimensionless quantity that quantifies how turbulent a flow is by comparing an effective viscosity caused by turbulence to the actual kinematic viscosity of the fluid. The most commonly used turbulence

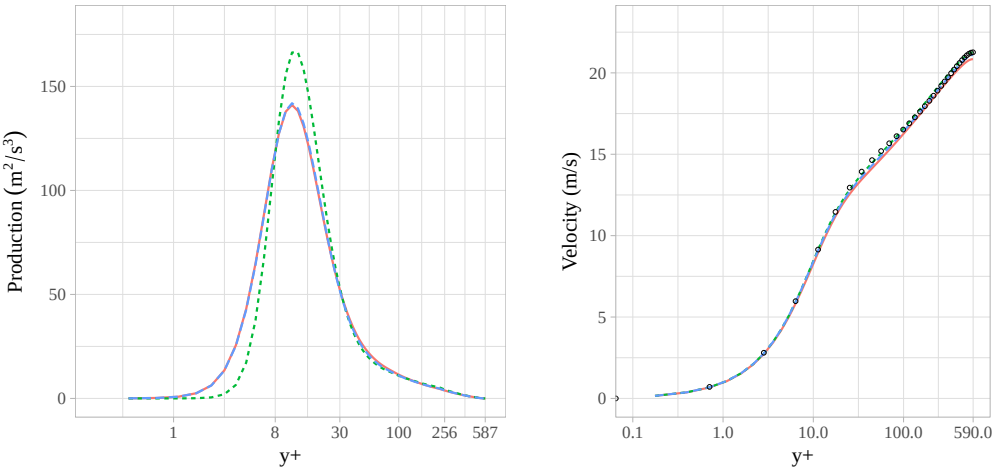

(a) *TKE Production* **(b)** *Mean velocity*

Figure 4.1: Comparison of channel flow mean velocity simulation results with a-priori calculated production models from DNS data of Moser et al. [248] (------) Classic Production (eqn 25), (———) Exact Production (eqn 24), (- - - - -) Mixed Production (eqn 27), (∘) DNS Data, Moser et al.

Reynolds number (stated three different but equivalent ways depending on preference) is a function of $f(k, \varepsilon, \nu)$.

$$Re_\tau = \frac{kT}{\nu} \tag{4.26}$$

$$Re_L = \frac{k^{1/2}L}{\nu} \tag{4.27}$$

$$Re_T = \frac{k^2}{\nu\varepsilon} \tag{4.28}$$

However, similar non-dimensional turbulence Reynolds numbers exist and depend on the model's definition of ν_t and it is incumbent upon researchers to define

which turbulence Reynolds number is being used.

$$Re_T = \frac{\nu_t}{\nu} \tag{4.29}$$

$$Re_T = \frac{R_{12}}{\nu \boldsymbol{\omega}} \tag{4.30}$$

In a simple flow situation such as a plane channel, where all else is kept the same, decreasing the fluid's kinematic viscosity would increase turbulence Reynolds number and therefore result in a decreasing boundary layer height with sharper gradients near the wall. Some flow variables, turbulent kinetic energy for instance, scale with turbulence Reynolds number while others do not. A large part of correctly capturing physics in a turbulence model is for that model to be able to capture term scaling with turbulence Reynolds number.

4.2.1 Turbulence Dissipation

The dissipation rate tensor in turbulent flow has been studied extensively for modeling purposes. Antonia et al. [249] give some modeling history and suggest a model based on the dissipation anisotropy tensor d_{ij} related to the Reynolds stress anisotropy tensor by $d_{ij} \approx Re_T^{1/2} b_{ij}$.

How then should one create a dissipation term that is tensorially consistent, yet somehow deals with the impossible conundrum of dissipation terms that have different powers of turbulence Reynolds number dependence? In the elliptic ver-

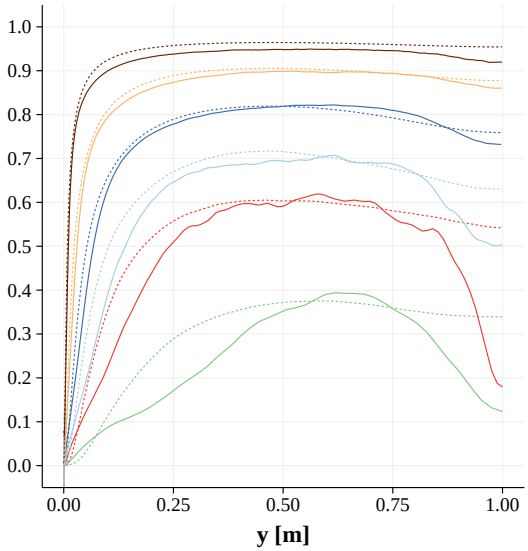

Figure 4.2: DNS Dissipation in ϕ/k divided by $(\frac{\phi}{k} - \frac{2}{3})\frac{\varepsilon}{k}$ (solid Lines) and the $(1-\gamma)$ model term (dashed lines)

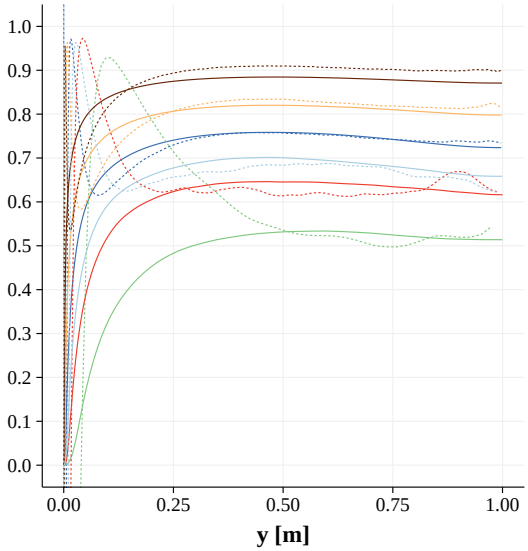

Figure 4.3: DNS Dissipation in ψ/k divided by $(\frac{\psi}{k})\frac{\varepsilon}{k}$ (solid lines) and the $(1-\lambda)$ term (dashed lines)

sion of the TPM presented below, the $1-\lambda$ terms in front of the dissipation are considered to be different, however this is less than ideal from a consistency standpoint.

4.2.2 Diffusion/Eddy Viscosity

Many RANS models use simple expressions for eddy viscosity, such as $\beta_k k^2/\varepsilon$ or $C_\mu v^2 T$, however the eddy viscosity in the Turbulent Potential model is solely an additional diffusion mechanism. If one looks only at the $Re_T = 590$ channel flow case, it would seem that these expressions capture the actual eddy viscosity $R_{12}/(\partial U/\partial y)$ well enough for engineering purposes. As concerns the TPM, the diffusion terms for the turbulent potentials are not turbulence Reynolds number dependent. However, looking at the formulations for eddy viscosity, we see that there is a significant turbulence Reynolds number dependence present in the commonplace version.

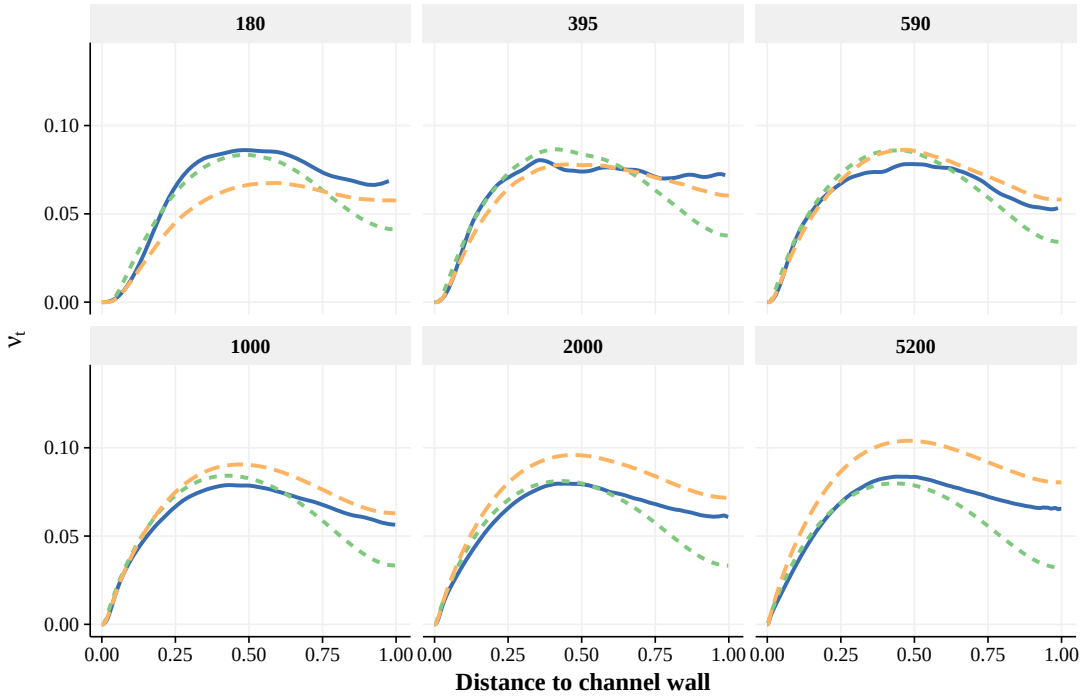

Figure 4.4: Turbulence Reynolds number dependence of ν_t. Shown for (——) $R_{12}/(\partial U/\partial y)$, (– – – –) $C_\mu v^2 T$, and (·····) the new TPM model

A new model for eddy viscosity (diffusion only) is offered in the Turbulent Potential model statement of equations in appendix A. It uses the λ term to offset the turbulence Reynolds number dependence in the original.

4.3 Elliptic Potential Model

Inhabiting the space between the computational efficiency and stability of one and two-equation turbulence models, and the physical accuracy of Reynolds stress transport models, are the $\boldsymbol{v^2 f}$ and Turbulent Potential models. These models are related in the use of their respective variants of the wall normal Reynolds stress as a transport variable. In the $\boldsymbol{v^2 f}$ model v^2 is used directly. In the Turbulent Potential model the derivatives of ϕ and v^2 are equal, and in flows with a single direction of inhomogeneity, ϕ and v^2 are equivalent. Both models have been shown to perform well in a variety of flow regimes, though in the context of this work, it can be said that they have complimentary shortcomings. Despite the advanced physics of the $\boldsymbol{v^2 f}$ model, it is still dependent on the eddy viscosity hypothesis. The Turbulent Potential model, despite avoiding the eddy viscosity hypothesis, has included ad-hoc (asymptotically consistent) damping of the redistribution terms and treats ϕ as a local (hyperbolic) transport PDE when in actuality it has been shown to behave more elliptically.

The $\boldsymbol{v^2 f}$ model was first presented in Durbin [250] and has become widely used in industrial and research applications since that time. $\boldsymbol{v^2 f}$ has been shown to perform well in separated flows [251] and on strongly lifting bodies [252, 253]. Much discussion and effort has been made towards correcting the model in stag-

nation point flows. In [254], Durbin shows that realizability constraints on turbulent length and time scales can prevent extraneous TKE buildup near stagnation points. Sveningsson shows in [246] that these realizability constraints are important insofar as their effect on the TKE production term, and as such, limiting the eddy viscosity is sufficient and makes the computations more stable generally.

Durbin [250] gives the background and justification necessary for including an elliptic wall blocking effect on the pressure strain term of the wall-normal Reynolds stress.

4.3.1 Model definition

The elliptic version of the TPM is defined in appendix A. The elliptic equation for the combined pressure strain and dissipation terms is of the same form as many other works [250, 255, 256]. However, it was found that a slow pressure strain term with both elliptic damping and $(1 - \lambda)$ damping was too suppressed near the wall. So, by an alteration of C_{p1} we can eliminate the λ completely from the equation.

$$C_{p1}^{*} = \frac{C_{p1} - \lambda}{1 - \lambda} \tag{4.31}$$

This definition results in $C_{p1}^{*} \approx 1.6$ in the freestream, rising near the wall where it is killed by the elliptic damping. A non-linear return-to-isotropy term has also been added to each of the slow pressure strain models of the potential equations. The elliptic version also uses a standard definition of the linear isotropization-of-

production (IP) model instead of that modified by Perot [239].

Rather than use an arbitrary damping function on the pressure strain in the ξ equation, f_d was created as the hyperbolic tangent of the ratio between f and the entire right hand side of the f equation. This results in a damping that mimics that of the scalar potential near the wall, while moving towards unity in the free-stream. Attempts at using a limiter at unity instead of hyperbolic tangent resulted in divergent solutions. Other damping functions were also tried for the pressure strain in the vector potential, but the inconsistency was constantly suspect when solutions went awry.

Channel flow results for the elliptic Turbulent Potential model are shown below, and results from the impinging jet case are shown in the results chapter. Preliminary results are promising, however much more testing is warranted before making any substantial claims about the model's efficacy.

4.4 Roughness Inclusion and Modeling Results

Aupoix and Spalart give a good introduction to boundary condition rough surface modeling options in [223], discussing two different approaches. The "discrete element approach" uses additional terms in the flow equations which they claim is rarely used. The "equivalent sand grain" approach connects a real-world roughness height to a non-dimensional idealized height which is then (in eddy viscosity models) used to increase near-wall turbulent eddy viscosity. Aupoix and Spalart further categorize this modeling approach into two methods, one in which eddy

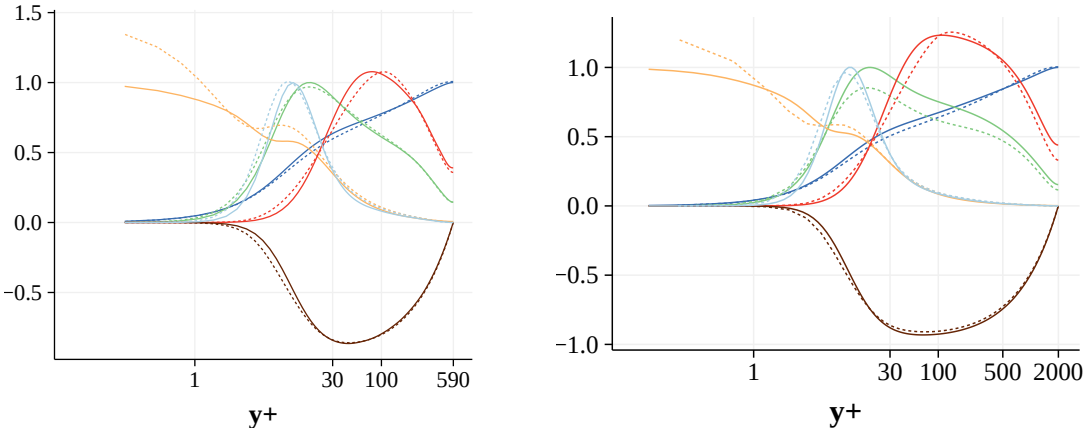

(a) *Elliptic Turbulent Potential at* $Re_\tau = 590$

(b) *Elliptic Turbulent Potential at* $Re_\tau = 2000$

Figure 4.5: Comparison of channel flow mean velocity simulation results with a-priori calculated production models. From DNS data of Moser et al. [248] and Lee and Moser [247], Dashed line: model, Solid line: DNS of Lee and Moser, (———) U/U_{max}, (———) $\varepsilon/\varepsilon_{max}$, (———) k/k_{max},(———) ϕ, (———) ψ, (———) P.

viscosity is zero at the wall and one in which eddy viscosity is greater than zero at the wall. Knopp convincingly shows in [228] that one such model of the first type, the $k-\omega$ roughness extension of Wilcox from 1998, requires onerously high near-wall resolution in order to properly represent the turbulence quantities starting from a zero boundary condition.

4.4.1 Roughness Regimes and Limits of Applicability

Looking back to figure 3.1, there is a clear structure to turbulent boundary layers. The classification of rough surface boundary layers is made in relation to the smooth boundary layer divisions. In a general sense, roughness elements that do not protrude beyond the viscous sublayer have little effect on the flow and are considered hydro-dynamically smooth. Conversely, roughness elements that entirely disrupt the buffer layer, where much of the turbulence generation processes

happen, and extend into the log layer are considered to be "fully rough" surfaces. Anything between these two extremes is considered to be in the "transitionally rough" region. The boundaries of these three regions are the source for considerable debate and examination. According to Aupoix [219], Nikuradse suggested that the smooth regime ends at $k_s^+ = 3.5$ and the fully rough regime starts at $k_s^+ = 68$. In developing their correlation, Ligrani and Moffat [212] recommended $k_s^+ = 2.25$ and $k_s^+ = 90$ as the limits for sand grain roughness and $k_s^+ = 15$ and $k_s^+ = 55$ for uniform spheres roughness, noting that the uniformity of the spheres leads to a less gradual transition.

4.4.2 Rough Wall BCs

Work on roughness in computational fluid dynamics has been primarily focused (for good reason) on turbulence models that are highly validated and widely used in industry. Two of the methods that use the equivalent sand grain approach are discussed in more depth, and will provide a basis for adaptation to the Turbulent Potential Model.

To start, we define the friction velocity to take into account both molecular and turbulent viscosity.

$$u_\tau^2 = \nu \frac{\partial u}{\partial y} + |\boldsymbol{\psi}| \tag{4.32}$$

4.4.2.1 Knopp et al. Method

Following Knopp's derivation [228] and defining $\omega = \varepsilon/0.09k$ we end up with the following equation for fully rough wall turbulence dissipation.

$$\varepsilon|_w = \frac{\beta_k^{1/2} k|_w u_\tau}{\kappa(y + d_0)} \tag{4.33}$$

This equation is valid in fully rough conditions only and will need to be altered for values of k_r^+ in the transitional roughness range. Using the Knopp modifications for the transitional roughness regime, the $\varepsilon|_w$ equation becomes the following.

$$\varepsilon|_w = \frac{u_\tau^3}{\kappa(0.03k_s)f(k_s^+)} min\left[1, \frac{k_s^+}{90}\right] \tag{4.34}$$

$$f(k_s^+) = min\left[1, \left(\frac{k_s^+}{30}\right)^{2/3}\right] min\left[1, \left(\frac{k_s^+}{45}\right)^{1/4}\right] min\left[1, \left(\frac{k_s^+}{60}\right)^{1/4}\right] \tag{4.35}$$

It was found that in order to be compatible with the ϕ boundary condition (derived a subsequent section), the "adapted" Knopp dissipation boundary condition needed to be scaled down by approximately 0.3.

$$\varepsilon|_w^* = \frac{0.3u_\tau^3}{\kappa(0.03k_s)f(k_s^+)} min\left[1, \frac{k_s^+}{90}\right] \tag{4.36}$$

For turbulent kinetic energy, we take the fully rough value to be the log layer

value in a turbulent flow modified by a linear function to represent the transitionally rough regime.

$$k|_w = \frac{u_\tau^2}{\beta_k^{1/2}} min\left[1, \frac{k_s^+}{90}\right] \tag{4.37}$$

Looking back to table 3.1 we see that this is a common starting point amongst the models that assume a finite turbulent viscosity at the wall.

$$\nu_t|_w = C_\mu \frac{\phi k}{\varepsilon} \tag{4.38}$$

$$\frac{\psi}{k}|_w = \frac{C_\mu \phi \boldsymbol{\omega}}{\varepsilon} \tag{4.39}$$

The ϕ/k wall value is discussed in a subsequent section of this work, and takes a considerable effort to determine. It will be shown that this value is dependent on the choice of k_w^+ and a roughness function.

4.4.2.2 Aupoix Method

In [219], Aupoix analyzes all previous attempts at including rough surface boundary conditions in the $k-\omega$ and $k-\omega SST$ family of models. He then transforms the equations into their non-dimensional equivalents and solves each rough surface inclusion method in order to compare them. A set of rough wall correlations is subsequently derived, one on Nikuradse's correlation and one upon the Grigson's

representation of Colebrook's results. These are shown below, and as an aside, these are also currently implemented in the commercial software Fluent.

$$k_w^+ = \frac{1}{\sqrt{\beta_k}} tanh\left[\left(\frac{log(k_s^+/30)}{log10} + 1 + tanh\frac{k_s^+}{125}\right) tanh\frac{k_s^+}{125}\right] \tag{4.40}$$

$$\omega_w^+ = \frac{300}{k_s^{+2}}\left(tanh\frac{15}{4k_s^+}\right)^{-1} + \frac{191}{k_s^+}\left(1 - exp\left(-\frac{k_s^+}{250}\right)\right) \tag{4.41}$$

From here it is trivial to expand the left hand side and write the boundary conditions for k_w and ω_w.

$$k_w = k_w^+ U_\tau^2 \tag{4.42}$$

$$\omega_w = \frac{\omega_w^+ U_\tau}{\nu} \tag{4.43}$$

4.4.2.3 New Expressions for TPM Variables

From the two methods discussed previously, as well as Durbin [224] we have possible rough boundary condition expressions for the k and ε variables. Though these works differ in terms of strategies for altering the transitional roughness regime, they rely on certain core fundamentals. Aupoix puts the SST models in context, and rigorously tests them in comparison to one another and experimental data. However, it is the author's understanding that such and undertaking has not been

made for any models containing Reynolds stresses (v2f, TPM, RTSMs as a whole). Where then should we look for ideas on the creation of boundary conditions for the ϕ and $\boldsymbol{\psi}$ variables in the TPM? There is just such a work from the DNS side of turbulence research by Orlandi [216], showing a relationship between the wall-normal Reynolds stress and the velocity shift caused by surface roughness. Orlandi starts by explaining that historically the wall-normal Reynolds stress has been less studied by experimentalists because of the difficulty of measuring it near the wall. DNS allows for high resolution snapshots of all the Reynolds stresses throughout the domain. He then discusses Nikuradse and the oft presented law of the wall.

$$U^+ = \frac{1}{\kappa} log(y^+) + B - \Delta U_C^+ \tag{4.44}$$

Using a large DNS data set at both low and intermediate turbulence Reynolds numbers ($Re_\tau = 200$ and $Re_\tau = 800$) and other validation cases, Orlandi was able to reformulate the law of the wall as such. For clarity's sake, $R_{22} = v'v'$ is the wall-normal Reynolds stress.

$$U^+ = \frac{1}{\kappa} log(y^+) + B(1 - \frac{\sqrt{v'v'}^+}{\kappa}) \tag{4.45}$$

Note that Orlandi's expression in [216] contains a U_w that was subtracted from the left hand side to estimate the velocity difference in the viscous and buffer layers. For our purposes we ignore this term (it is quite small) and present the

log-layer shift above.

Equation 4.45 gives us an avenue into developing a rough boundary condition for $\phi \approx v'v'$. To do so, we start with the Ligrani and Moffat approximation for the roughness function ΔU_C^+.

$$\Delta U_C^+ = (\frac{1}{\kappa} log(k_s^+) + B - 8.5) sin(\frac{g\pi}{2}) \tag{4.46}$$

$$k_s^+ < 2.25 : g = 0$$

$$k_s^+ > 90 : g = 1$$

$$2.25 < k_s^+ < 90 : g = \frac{log k_s^+ - log 2.25}{log 90 - log 2.25}$$

Setting equal the two roughness functions, and then rearranging gives an expression for the friction wall-normal Reynolds stress.

$$\phi^+|_w = \left(\frac{\kappa}{B} (\frac{1}{\kappa} log(k_s^+) - 3.4) sin(\frac{g\pi}{2}) \right)^2 \tag{4.47}$$

This in itself is an expression of the boundary condition for ϕ at a rough surface, however, the TPM solves for ϕ/k or $\sqrt{\phi/k}$ and as such, we should take the expression for k from Knopp, Aupoix, or Durbin and divide. From this point, it is simply (or not so simply) a matter of finding an $f(k_s^+)$ that represents the wall behavior of $\sqrt{\phi/k}$.

$$\frac{\phi_w^+}{k_w^+} = \frac{\left(\frac{\kappa}{B}(\frac{1}{\kappa}log(k_s^+) - 3.4)sin(\frac{g\pi}{2})\right)^2}{\frac{1}{\sqrt{\beta_k}}tanh\left[\left(\frac{log(k_s^+/30)}{log10} + 1 + tanh\frac{k_s^+}{125}\right)tanh\frac{k_s^+}{125}\right]} \tag{4.48}$$

$$\frac{\phi_w^+}{k_w^+} = \frac{\left(\frac{\kappa}{B}(\frac{1}{\kappa}log(k_s^+) - 3.4)sin(\frac{g\pi}{2})\right)^2}{\frac{1}{\sqrt{\beta_k}}min\left[1, \frac{k_s^+}{90}\right]} \tag{4.49}$$

A simple tanh function can then used to represent the dependence on k_s^+ for the Ligrani and Moffat correlation,

$$\frac{\phi_w^+}{k_w^+} = \frac{\phi|_w}{k|_w} \approx 0.12(tanh(k_s^+/14))^3 \tag{4.50}$$

as well as for the Aupoix/Colebrook correlation.

$$\frac{\phi_w^+}{k_w^+} = \frac{\phi|_w}{k|_w} \approx 0.22(tanh(k_s^+/14))^3 \tag{4.51}$$

Expression 4.48 uses the Aupoix definition of k_w^+ and expression 4.49 uses Knopp's method. It is important to note that because of the definition for $\boldsymbol{\psi}/k$ at the wall,

$$\left.\frac{\psi}{k}\right|_w = \frac{C_\mu \phi}{\varepsilon}\frac{\partial U}{\partial y}, \tag{4.52}$$

different (but proportional) values of ϕ_w can be paired with values of ε_w such that the Reynolds shear stress at the wall is equivalent. However, ϕ_w is non-negotiably

set to a roughness function of choice, and therefore the primary mode of altering ψ/k at the wall is through the ε_w boundary condition.

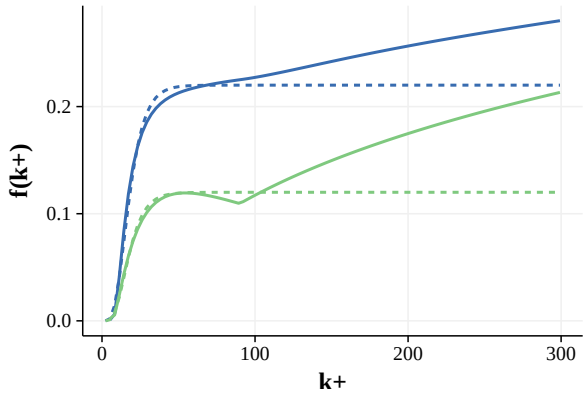

Figure 4.6: Model vs. Theory for ϕ/k at rough wall. (——) Theory Equation 4.48, (——) Theory Equation 4.49, (- - - - -) Current Work Equation 4.50,(- - - - -) Aupoix/Colebrook Model Equation 4.51

It was found that in the Turbulent Potential Model, obtaining model expressions (i.e. the dashed lines in figure 4.6), that did not trigger a runaway wall value of the turbulent vector potential,was not a trivial task. The expressions shown above were settled on as a compromise in order to get the transitional roughness behavior correct and the constant approximated to first order in the fully-rough regime. Future versions of this model should certainly consider revisiting this formulation in order to correctly handle larger roughness values. The choice of $\phi/k|_w$ as a constant in the fully rough regime is rather arbitrary given that it depends on the limiter imposed on the $k|_w$ equation. Arguably, the $k|_w$ equation should be modified and validated before moving on to $\phi/k|_w$.

An expression was found for ε_w that is a modification of the Knopp $\varepsilon|_w$ in the transitional roughness region. This is an adaptation of the Knopp ω_w equation

such that epsilon encouraged toward the smooth wall value at low k_s^+.

$$\varepsilon^+|_w = 0.23\left(0.2(1 - min(1, k_s^+/90)^3) + \frac{min(1, k_s^+/90)}{\kappa 0.03 k_s^+}\right) \tag{4.53}$$

4.4.2.4 Relevance of d_0

Development of a set of rough surface boundary conditions should ideally take into account the hydrodynamic roughness length scale that represents the distance d_0 for which the rough surface mean velocity would be extrapolated to 0 from the top of the roughness elements. Knopp et al. [228] give a particularly clear derivation and discussion of this concept, crediting [223] and [224] for the foundational work. The Knopp [228] derivation leads to the following expression.

$$\frac{y + d_0}{d_0} = \frac{y}{k_r} exp(\kappa B) \tag{4.54}$$

With the assumption that $d_0 << y$ this equation reduces to a simple function of k_r.

$$d_0 = exp(-8.5\kappa) k_r \approx 0.03 k_r. \tag{4.55}$$

At this point it is important to stop and note that this may be the simplest representation of d_0 and there could be any number of expressions that work. Durbin [224] uses a more complicated expression, calibrating with experimental

boundary layer data to get d_0 (noted as y_0 in [224]).

Aupoix [219] discusses d_0 and concurs that strictly speaking the $0.03k_s$ wall shift should be accounted for. He claims that it is mandatory for models in which the wall distance plays a key role, i.e. Smith's k-l model or Spalart-Allmaras. However, he ignores the shift in his ***kω-SST*** model owing to it only affecting a marginal activation of the SST limiter. It is also clear that dissipation wall boundary conditions developed to use u_τ^3 in the numerator need a length scale in the denominator in order to be consistent, whereas those using u_τ^4 in the numerator need only a viscous scale in the denominator and can subsume any length scales into the $f(k_s^+)$.

CHAPTER 5

RESULTS AND DISCUSSION

5.1 Computational Cost: TPM vs. Others

One primary factor in assessing a turbulence model is computational cost. As a general rule, the computational cost of a model increases with the number of transport equations solved. The airfoil cases presented here have undergone timing simulations in order to understand the true added cost of the additional transport equations in the Turbulent Potential Model. These timing runs were completed using OpenFOAM on the same single node, using 64 Intel MIC co-processor CPUs. The k-Epsilon model was used as a baseline, given its widespread use and low computational cost. Each timing has been averaged over 700 timesteps. Each case was set up using an unsteady combined PISO-SIMPLE loop with three outer corrector loops and two inner corrector loops and one non-orthogonality pressure corrector. This timing is a straightforward cost comparison of each turbulence code, and does not take into consideration slower/faster convergence properties of any model.

	$k-\varepsilon$	$k\omega - SST$	$v^2 f$	TPM
Timestep	1.0	1.03	1.07	1.18
Turbulence Subroutine	1.0	1.15	1.99	2.64

Table 5.1: Comparison of relative computational times for simulation of 4 degree angle of attack airfoil, using $k-\varepsilon$ as a baseline

The table above confirms the general rule regarding transport equations and added computational cost. The $k-\epsilon$ model solves 2 equations, as does SST. The v^2-f model solves 4 transport equations (for roughly twice the model cost). And the TPM model solves 6 equations (in 3D). However, the less intuitive result is that despite a 264% increase in the TPM turbulence modeling cost compared to $k-\epsilon$, a timestep only increases by 18%. The predominant cost of this flow solution, like almost all others, is in elliptic mean pressure solution, and not in the turbulence models.

5.2 Wind turbine boundary layer considerations

As a first step to approaching this problem, it is important to recognize whether or not superhydrophobic surfaces, with mean roughness heights on the order of 30 to 100 microns, are large enough to disrupt turbulent generation happening outside the viscous sublayer. To do so, the NREL 5MW reference turbine [257] and Upwind 8MW turbine geometries are used to compare the height of the viscous sublayer to the mean height of SHS asperities. Figures in appendix C show a first estimate as to whether the super-hydrophobic features will significantly affect the flow using the Schlicting Law for the coefficient of skin friction in equation 3.5. Reynolds numbers at each spanwise blade section are calculated using U_{rel}, the velocity seen by a wind turbine blade, defined by the following equation from [27].

$$U_{rel} = \sqrt{U_{inf}^2 + (\Omega r)^2} = U\sqrt{1+\lambda^2} \tag{5.1}$$

The Reynolds number is then defined by the following equation where ν is the kinematic viscosity and C_r is the chord length at a spanwise radius r.

$$Re = \frac{U_{rel} C_r}{\nu} \tag{5.2}$$

In sum, the figures in appendix C affirm, to first order, the notion that superhydrophobic surface asperities do protrude into the buffer layer, and as such are likely to affect turbulence generation in a wind turbine boundary layer. Note also that as Reynolds numbers increase, with the upscaling of turbine blades, it is expected that surface asperities will have an even more significant impact.

5.3 Initial work with wall functions

Steady state simulations over a range of attack angles (α) are carried out in OpenFOAM 1.6-extend for both the smooth and rough surface s809 airfoil and compared to the Ohio State University airfoil experiments [21]. The Spalart-Allmaras turbulence model is used, and a wall function approach is applied to solid boundaries. The figures in appendix D show results for lift, drag, and moment coefficients, and a parametric variation of the "roughnessConstant" parameter in OpenFOAM. Lift coefficient generally shows good agreement, while drag coefficient and moment coefficient are less accurate.

C_s, varied in the second two plots of appendix D, is a tunable constant (matching that of Fluent 6.3) such that the default value ($C_s = 0.5$), when used with k-ϵ turbulence models, reproduces Nikuradse's rough pipe data assuming tightly-

packed, uniform sand-grains. These simulations are assumed to be in the fully rough regime and as such use equation 3.18. Results suggest that the estimated value of K_s could be too high and that lower values may give more accurate results.

5.4 Channel Flow

The $Re_\tau = 590$ channel flow DNS of Moser, Kim, and Mansour [248] provides a development and testing ground for the turbulent potential model. The viability of terms is immediately seen if DNS channel flow results are plugged in to term balance plots. After channel simulations are run, results can be compared as in figure 5.2.

Plane channel flow provides a baseline computational simulation from which to launch all further inquiry. RANS models are often first-pass verified and/or tuned to plane channel flow given the ease of implementation and the abundance of DNS statistics available for comparison. This work uses a 4 x 4 x 256 grid with a channel half height of 1m.

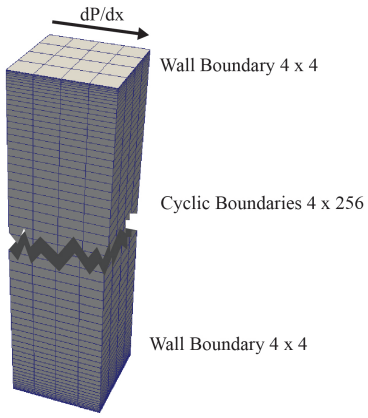

Figure 5.1: Stylized drawing of channel flow mesh

5.4.1 Smooth Wall Channel Flow

It can be shown that the no-slip condition on the channel wall leads to a set of smooth surface boundary conditions. The condition $\varepsilon_w = 2\nu\nabla k^{1/2}|_n$ encourages k to approach the wall like $O(y^2)$.

k_w	ε_w	ϕ/k_w	$\boldsymbol{\psi}/k_w$
0	$2\nu\nabla k^{1/2}\|_n$	0	$\langle 0,0,0\rangle$

Table 5.2: Smooth wall boundary conditions for the Turbulent Potential Model simulation

As a portion of this work is dedicated to addressing inconsistencies in turbulence Reynolds number dependence of the model, two smooth wall channel flow simulations at two different Re_τ are shown. It is uncommon in the turbulence modeling literature to present channel flow simulations, though it probably should be the norm to present at least two. Many assumptions contain hidden or non-intuitive dependencies on turbulence Reynolds number.

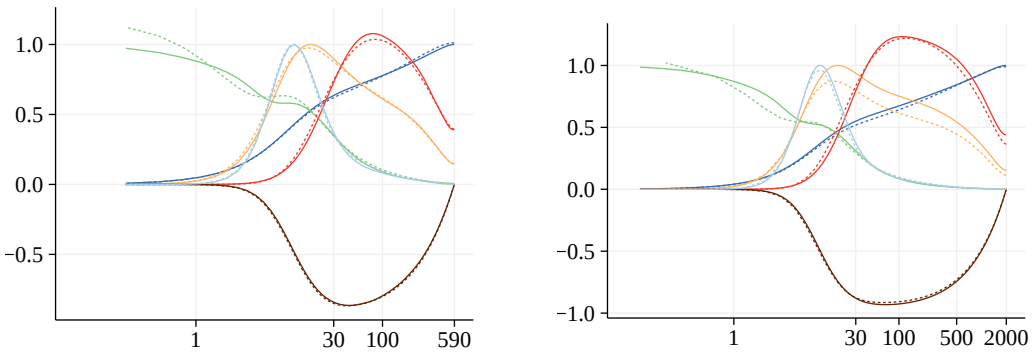

(a) $Re_\tau = 590$ **(b)** $Re_\tau = 2000$

Figure 5.2: Comparison of channel flow mean velocity simulation results with a-priori calculated DNS data. From DNS data of Moser et al. [248] and Lee and Moser [247]. Dashed line: model, solid line: DNS, (———) U/U_{max}, (———) $\varepsilon/\varepsilon_{max}$, (———) k/k_{max},(———) ϕ, (———) ψ, (———) P.

Figure 5.2 shows good agreement between the TPM turbulence statistics and DNS results, with the obvious exception of the turbulence kinetic energy under-prediction in the $Re_\tau = 2000$ case. This is an interesting result given that the turbulence production and dissipation show relatively good agreement. It stands to reason that if the P and ε terms are accurate, the turbulent diffusion term is the only term left in the TKE equation for inaccuracy to affect the solution.

5.4.2 Rough Wall Channel Flow

The primary objective and test for rough surface modifications to turbulence models is to replicate the downward velocity shift that occurs with increasing roughness height. To do so, the same mesh as used for the smooth wall is used here. An equivalent sand grain height is then estimated given an arbitrary range of non-dimensional roughness heights $k_s^+ < 125$ using the smooth wall friction velocity and kinematic viscosity $k_s = k_s^+ \nu / U_\tau$. Note that the actual k_s^+ will be slightly different given the changes incurred by imposing non-zero Reynolds stresses at the wall, but these differences are only on the order of 0.1%. Knopp-adapted and Aupoix-adapted boundary conditions are tested alongside the current work.

The velocity shift for the Knopp-adapted boundary condition simulations are shown in figure 5.3. It is immediately apparent that the lower third of the transitional roughness regime is under-predicted, or intentionally made to be closer to the Nikuradse data, which is similar to what Aupoix predicted in [219].

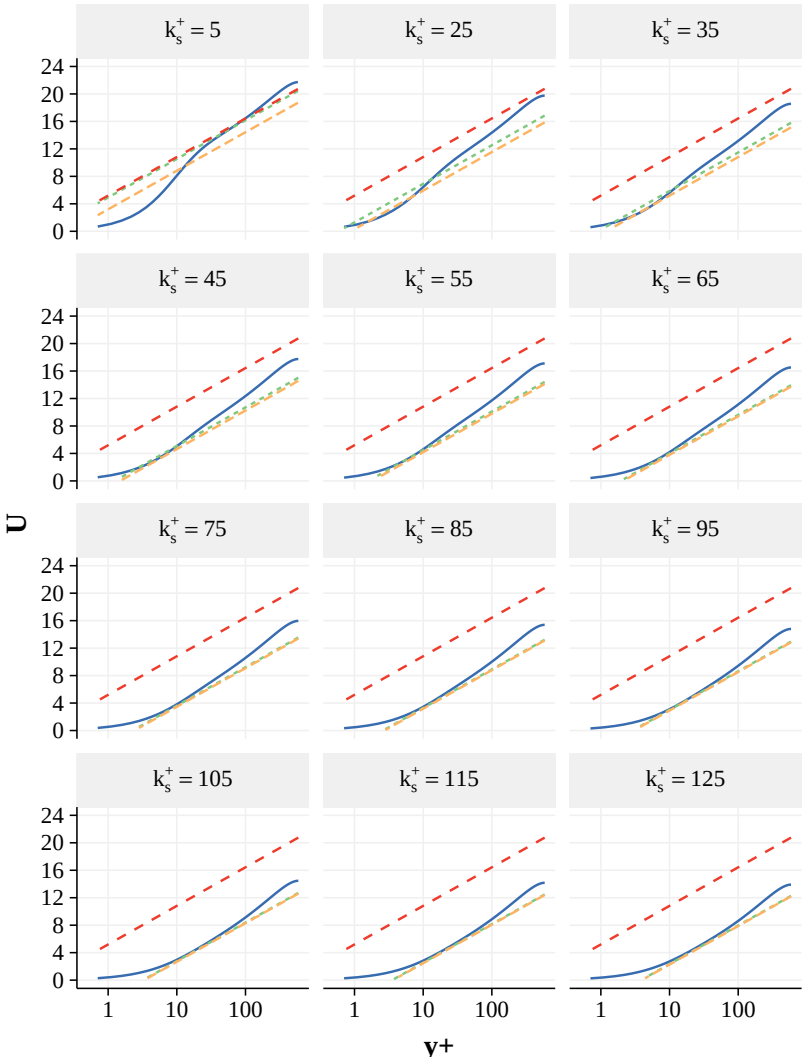

Figure 5.3: Rough wall channel flow results for multiple values of k_s^+ using the method adapted from Knopp et al. [228]. (- - - - -) Smooth log-layer theory, (---------) Ligrani and Moffett (Nikuradse) (- - - - -) Colebrook,(———) Velocity from channel from simulation

Attempts were made to bolster the velocity shift in the under-predicted region by adding a multiplier to $\boldsymbol{\psi/k}|_w$ in the form of $0.15(1+0.67\sqrt{90/k_s^+})\boldsymbol{\psi/k}|_w$ but this only worsened the outcomes at low k_s^+. The $\boldsymbol{\psi}/k|_w$ boundary condition makes the solution depend significantly on ε_w which appears to be stronger in the $k_s^+ < 20$ region than is reasonable for the Turbulent Potential model.

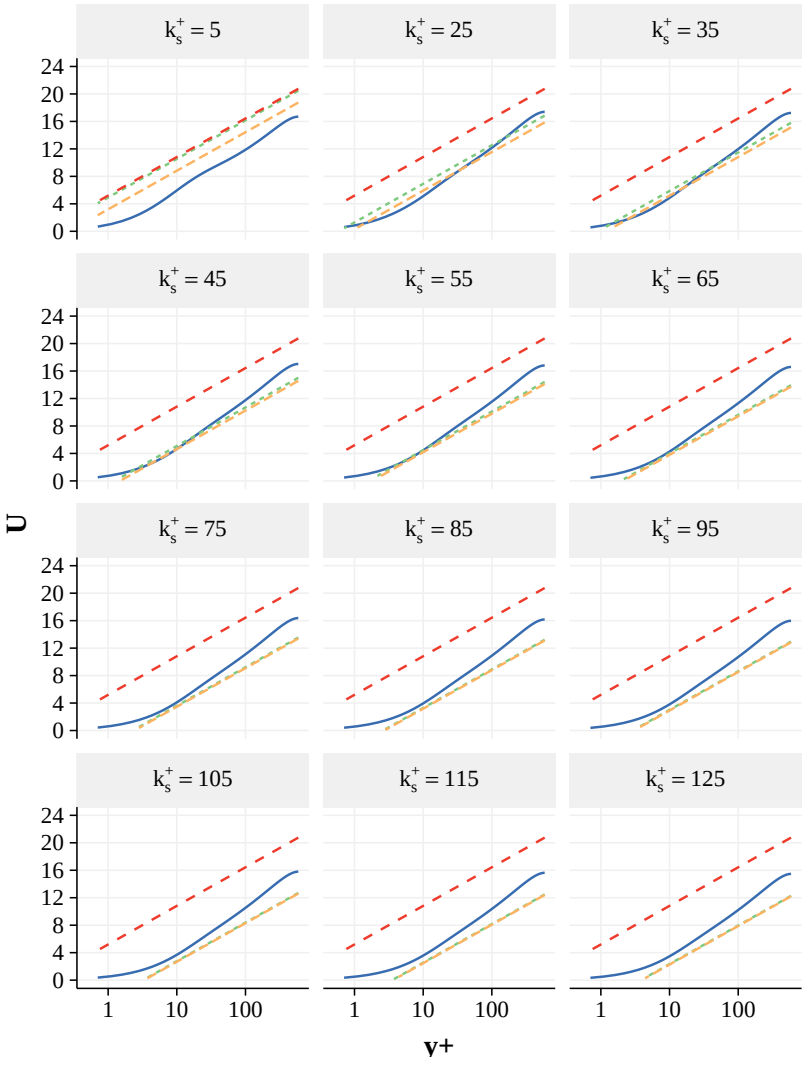

Figure 5.4: Rough wall channel flow results for multiple values of k_s^+ using the method adapted from Aupoix [219]. (- - - - -) Smooth log-layer theory, (----------) Ligrani and Moffett (Nikuradse) (- - - - -) Colebrook,(———) Velocity from channel from simulation

The next figure contains the results from the Aupoix-adapted method. This set of results is oppositely configured to that of the Knopp-adapted correction, wherein the low k_s^+ results are over-predicted compared to both the Ligrani and Moffett and Colebrook values, and values approaching and at the fully rough regime are slightly under-predicted. Given that Aupoix used the Colebrook data

when creating his model [219], it makes intuitive sense that these results are closer to the Grigson/Colebrook values.

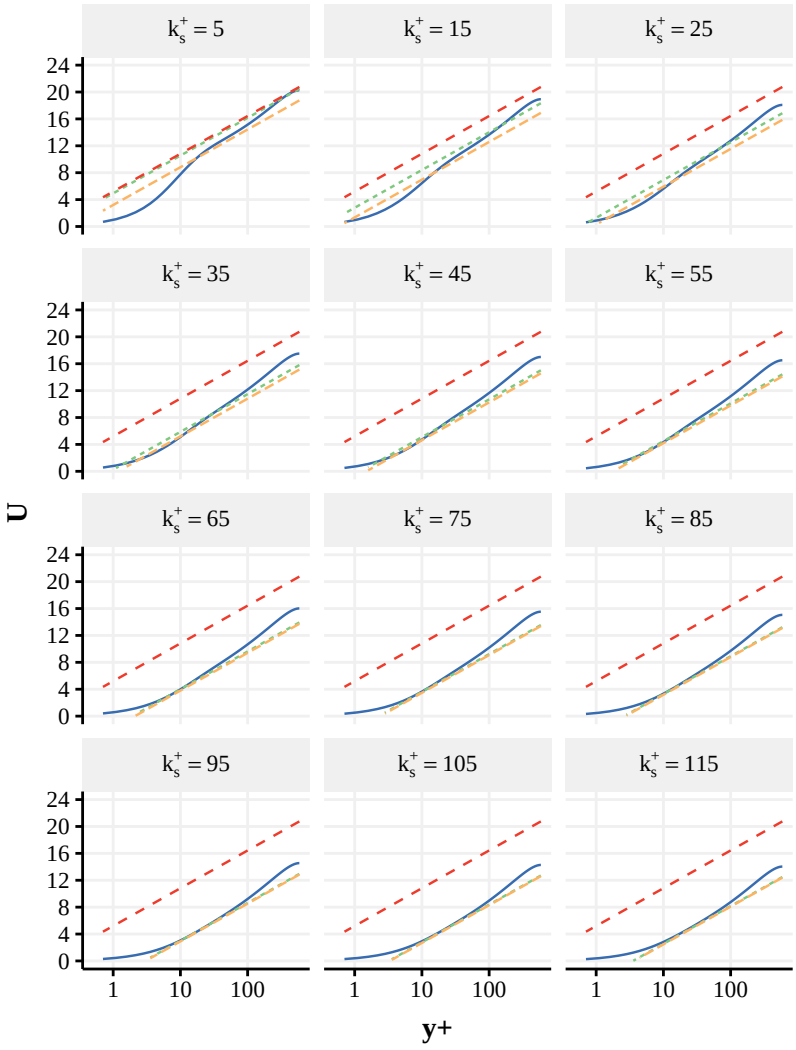

Figure 5.5: Rough wall channel flow results for multiple values of k_s^+ using the newly developed method. (- - - - -) Smooth log-layer theory, (----------) Ligrani and Moffett (Nikuradse) (- - - - -) Colebrook,(———) Velocity from channel from simulation

Figure 5.5 shows the simulation results of the boundary conditions given in the current work. These use the linear dependence on k_s^+ on the turbulent kinetic energy given by Knopp, a $\phi/k|_w$ given by combining Orlandi's work with the Ligrani

and Moffat roughness correlation of Nikuradse's work. $\varepsilon|_w$ is a new function that is similar to Knopp, but modifies the transitional behavior significantly. The results are believed to be a closer representation of actual roughness and seem to compare favorably to the roughness functions in Flack and Schultz [193]. These results sit between the Nikuradse and Colebrook (Ligrani/Moffat and Grigson correlations respectively) roughness functions below $k_s^+ = 15$.

Though the velocity shift is a fairly intuitive outcome of additional drag at a boundary, how should the turbulence quantities behave? Figures 5.6a through 5.6h compare the primary model variables with the current work on the left and the Aupoix-adapted condition on the right. Starting with k, there is a sizable difference in the distribution of $k|_w^+$ values. Though they both are increasing with k_s^+, the Aupoix-adapted boundary is increasing much more slowly. Lower $k|_w^+$ values allow for a larger $\phi/k|_w$ given our method for determining the boundary condition, which in turn drives a higher $\psi/k|_w$. These plots provide two arguments in favor of using the newly developed boundary condition. First, the Aupoix-adapted solution appears to depend on the $\varepsilon|_w$ boundary condition moving towards zero as k_s^+ does the same. However, an ideally configured solution would move $\varepsilon|_w^+$ toward the smooth wall solution, not zero.

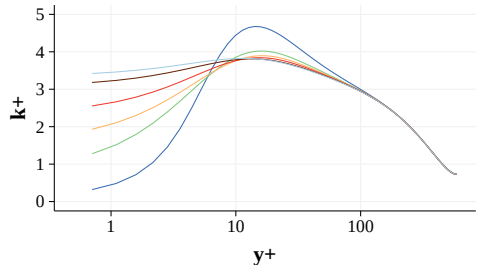

(a) *Turbulent kinetic energy: New boundary conditions*

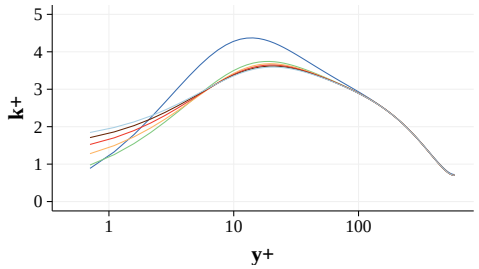

(b) *Turbulent kinetic energy: Aupoix-adapted boundary conditions*

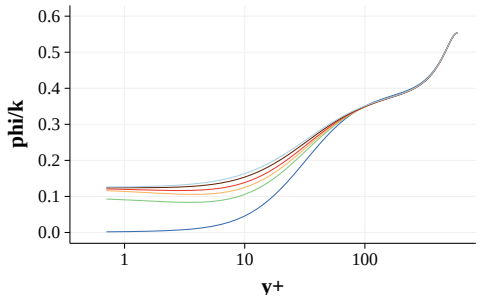

(c) ϕ/k*: New boundary conditions*

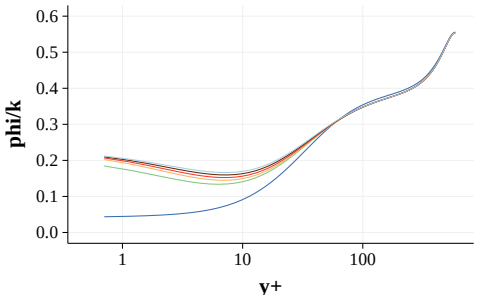

(d) ϕ/k*: Aupoix-adapted boundary conditions*

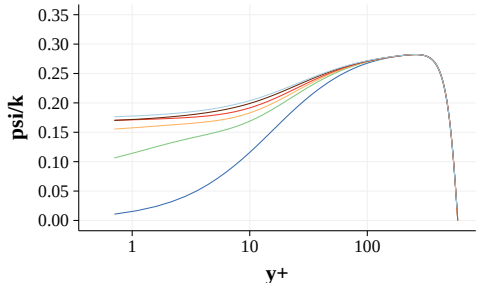

(e) ψ/k*: New boundary conditions*

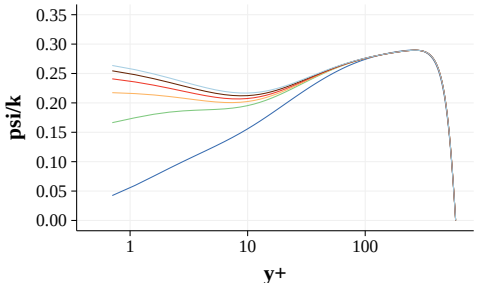

(f) ψ/k*: Aupoix-adapted boundary conditions*

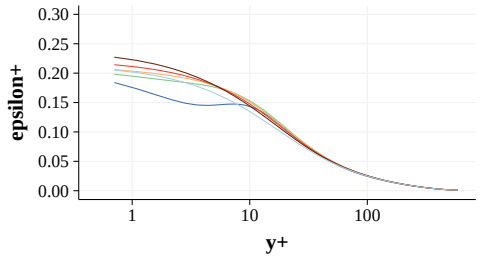

(g) ε*: New boundary conditions*

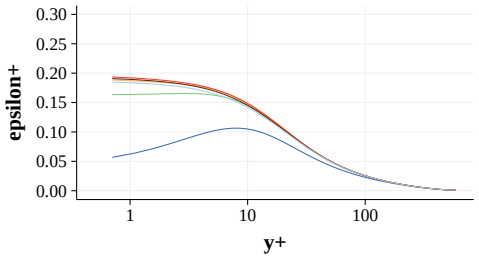

(h) ε*: Aupoix-adapted boundary conditions*

Figure 5.6: Comparison of channel flow turbulence quantities with varying roughness heights. (——) $k_s^+ = 5$, (——) $k_s^+ = 25$, (——) $k_s^+ = 45$,(——) $k_s^+ = 65$, (——) $k_s^+ = 105$

It is possible that the smooth wall solution could increasingly be blended in at low k_s^+ values, however this was beyond the scope of this work. The second argument is that the $\phi/k|_w$ and $\psi/k|_w$ in the newly developed model are monotonically increasing for all k_s^+ while the Aupoix-adapted boundary conditions create a negative slope in these variables near the wall. It is also possible that because this solution (and the Knopp et al. as well) were developed for the ω equation and not the ε equation, that they do not translate as simply as using the relation $\omega = \varepsilon/(0.09k)$. These solutions are shown to work well in the ***kω-SST*** equations [219] and the assumption of a straightforward translation to the TPM equations could be at issue.

5.5 Impinging Jet with Heat Transfer

The axisymmetric impinging jet experiments of Baughn et al. [258] and Cooper et al. [259], and the subsequent turbulence model comparison of Craft et al. [260] are valuable comparative case studies for turbulence model assessment of stagnation point (strain dominated) turbulent flow. In these experiments, a fully developed flow of air exited a round pipe at 90 degrees to a heated flat plate at various heights. The impinging jet case with H/D=2 was chosen for this work to minimize the number of computational cells needed in the domain.

Heat transfer from the impingement plate is handled using equations 5.3 through 5.6. The air jet is at ambient temperature of $\Theta = 300K$, while the plate is at a constant temperature of $\Theta = 360K$. Buoyancy and radiation effects are neglected in this model.

$$\frac{D\Theta}{\partial t} = \frac{\partial}{\partial x_i}\left(\frac{\nu}{Pr}\frac{\partial \Theta}{\partial x_i} + \overline{u_i\theta}\right) \tag{5.3}$$

$$\overline{u_i\theta} = \frac{\nu_{t\psi}}{Pr_t}\frac{\partial \Theta}{\partial x_i} \tag{5.4}$$

$$\nu_{t\psi} = \frac{|\boldsymbol{\psi}|}{|\boldsymbol{\omega}| + 1e^{-5\frac{\varepsilon}{k}}} \tag{5.5}$$

$Pr = 0.7$ is the viscous Prandtl number and Pr_T is the turbulence Prandtl num-

ber. The Pr_T used in this work is that of Kays and Crawford, as is used in Behnia [261] and elsewhere for this problem. This formulation of turbulence Prandtl number takes a value of approximately 1.7 at the wall and quickly asymptotes to 0.85 in the free-stream.

$$Pr_t = \frac{1}{0.5882 + 0.228(\nu_t/\nu) - 0.0441(\nu_t/\nu)^2(1 - exp(-5.165/(\nu_t/\nu)))} \tag{5.6}$$

Simulations are run at $Re_D = 23000$ and $Re_D = 70000$. It was ensured that these simulations had a centerline entrance pipe velocity approximately equal that of the correlation given in [259]. The results of a turbulent pipe flow simulation are mapped to the inlet of a 5 degree wedge domain shown in figure 5.7. This wedge mesh contains approximately 5×10^4 cells and the bottom wall is resolved to a non-dimensional first cell height of $y^+ \approx 2$.

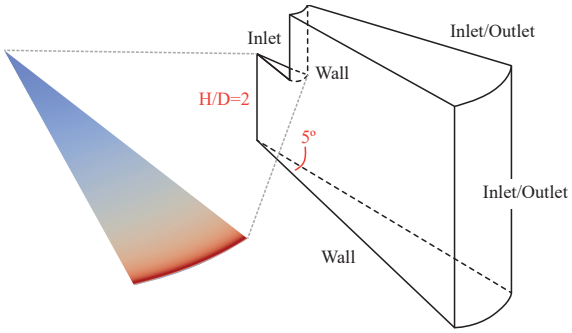

Figure 5.7: Diagram of axisymmetric impinging jet domain with example inlet condition for turbulent kinetic energy

In order to explore the turbulent kinetic energy production term, the impinging jet simulations using the TPM were run using equations 4.18, 4.22, and 4.24. Fig-

ure 5.8 shows the results of this comparison along with results using the $k\omega$-SST and v^2f turbulence models. The $k\omega$-SST version used is the default version in Foam-Extend from [262] with updated coefficients from [263].

Qualitatively, figure 5.8 shows that equation 4.18 is the closest to the other models and does not build up any turbulent kinetic energy near the stagnation point. The classic production model shows a sizable build-up of turbulent kinetic energy at the stagnation point. It is shown in other texts that this build-up is most likely the product of a turbulence model that has passed the limit of realizability. The mixed model lies in between the two extremes but close to the other models.

Another difference in the TKE solutions is that none of the TPM simulations lose turbulent kinetic energy near where the outer part of the jet turns. Both $k\omega$-SST and v^2f seem to lose a small degree of turbulent kinetic energy before gaining it back after the turn. This region of the jet is a turning mixing layer. It is clear from the above visualizations that $k\omega$-SST jet mixing layers (edges) spread significantly more after exiting the pipe than any of the other models, with the TPM exhibiting the least spreading.

The experiments of Cooper et al. used the Nusselt number as a proxy turbulence measurement, which on a surface can be a sensitive measure of turbulence in the adjacent flow. The Nusselt number can be written as in equation 5.7 where D is the jet diameter and n is the direction normal to the wall.

$$Nu = \frac{\frac{\partial \Theta}{\partial n} D}{T_{amb} - T_{wall}} \tag{5.7}$$

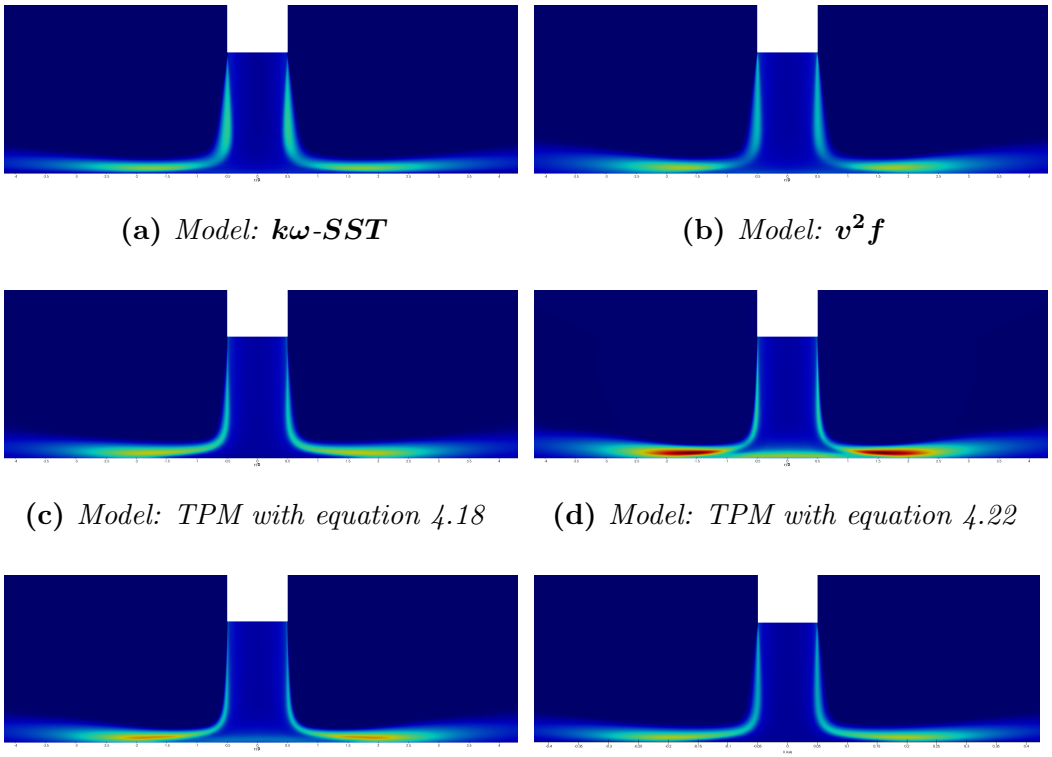

(a) *Model:* $k\omega$*-SST*

(b) *Model:* v^2f

(c) *Model: TPM with equation 4.18*

(d) *Model: TPM with equation 4.22*

(e) *Model: TPM with equation 4.24*

(f) *Model: Elliptic Turbulent Potential model*

Figure 5.8: Comparison of impinging jet turbulent kinetic energy results

Figure 5.9 shows the Nusselt number results for the tested models and the lower Re case (23,000). Figures 5.9a and 5.9b are shown for comparative purposes. Figures 5.9d and 5.9e confirm the qualitative picture seen in figure 5.8. The classic production term causes a build-up of turbulence near the stagnation point, and should probably not be used without some form of realizability constraint. It is therefore reasonable to continue using the $\psi \cdot \omega$ version of the production term with the caveat and understanding that it is necessarily missing some of the

production coming from straining or flow acceleration.

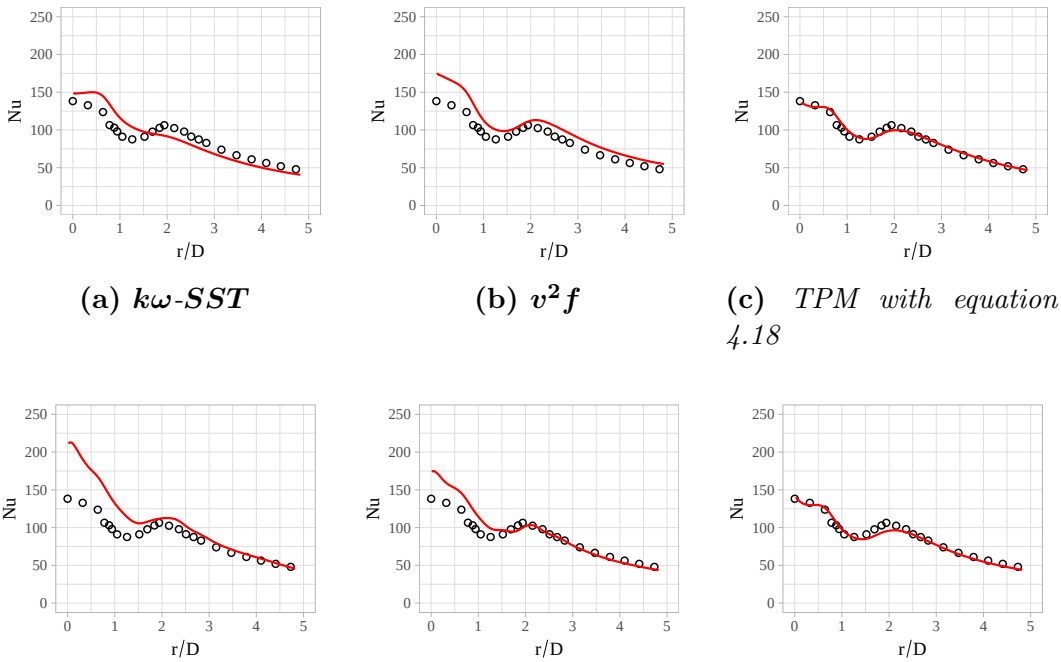

(a) ***kω-SST*** **(b)** v^2f **(c)** *TPM with equation 4.18*

(d) *TPM with equation 4.22* **(e)** *TPM with equation 4.24* **(f)** *Elliptic Turbulent Potential Model*

Figure 5.9: Comparison if impinging jet Nusselt number at Re=23000. (——) Simulation results, (○) Baughn et al. experiment [258].

The higher Reynolds number (70,000) case is shown in Figure 7. At this Reynolds number all the models struggle to reproduce the data as well as in the Re=23,000 case. This may be as much a result of the heat transfer models as the turbulence models. The TPM performs comparably to the other two models on this difficult test case.

Moving from heat transfer to mean velocity and wall normal Reynolds stress, results in figures 5.11 (Re=23,000) and 5.13 (Re=70,000) show predictions of mean velocity in the wall boundary layer for all tested models. The scalar potential, as shown in figures 5.12 and 5.14, though not exactly equal to v' in a 2D flow, we

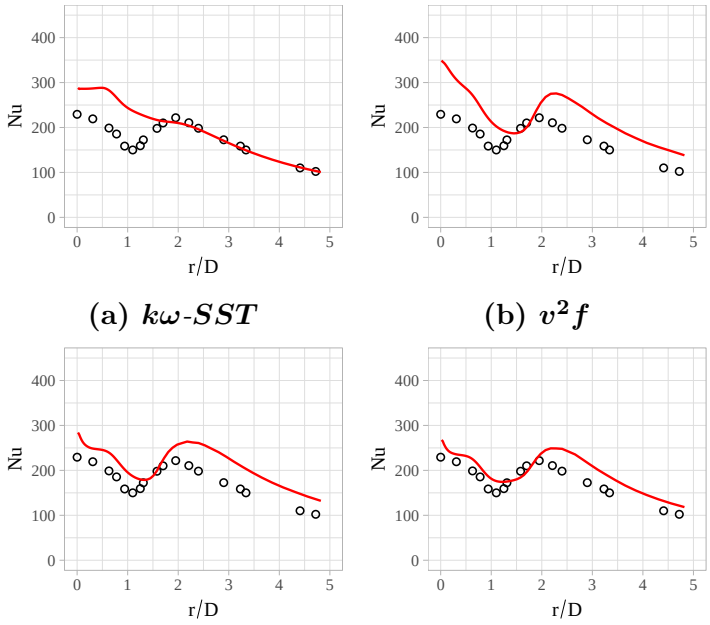

(a) ***kω-SST*** **(b)** $\boldsymbol{v^2f}$

(c) *TPM with equation 4.18* **(d)** *Elliptic Turbulent Potential Model*

Figure 5.10: Comparison if impinging jet Nusselt number at Re=70000. (——) Simulation results, (○) Baughn et al. experiment [258].

compare with v' from the data set. This shows reasonable agreement at R/D=1 or larger (where the BL is close to 1D), and worse agreement at the pipe radius R/D=0.5 (where the flow is still fairly two-dimensional in its directions of inhomogeneity).

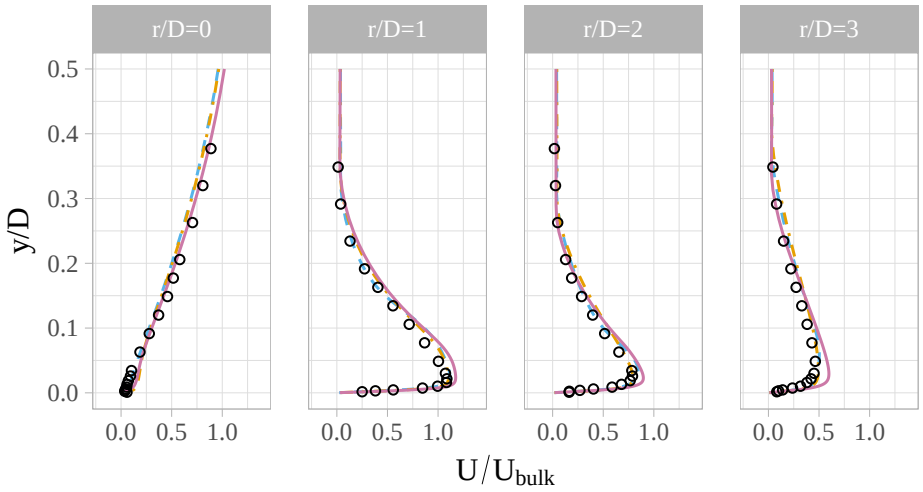

Figure 5.11: Mean velocity of impinging jet at $Re_D = 23000$. (○) Cooper et al. from ERCOFTAC database [259], (- - - -) Turbulent Potential Model, (–·–·–) $\boldsymbol{v^2 f}$ model, (———) $\boldsymbol{k\omega}$-$\boldsymbol{SST}$ model

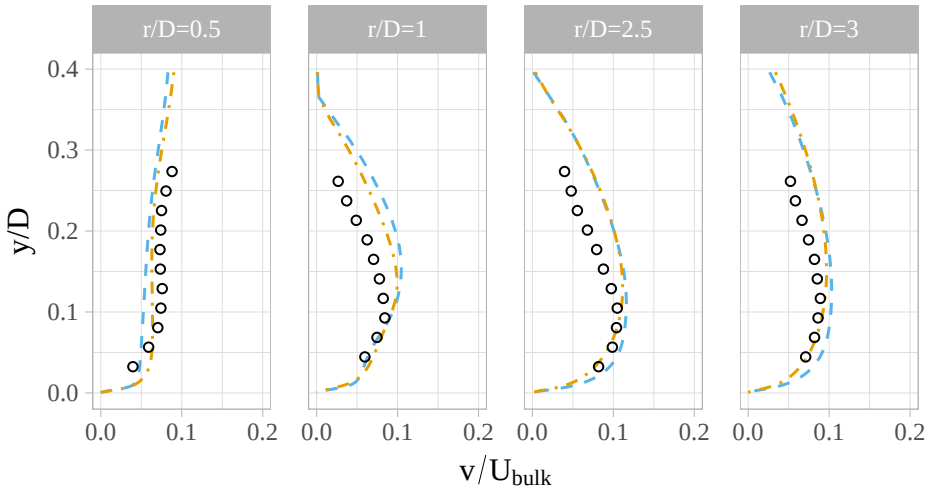

Figure 5.12: Wall-normal Reynolds stress of impinging jet at $Re_D = 23000$. (○) Cooper et al. from ERCOFTAC database [259], (- - - -) Turbulent Potential Model, (–·–·–) $\boldsymbol{v^2 f}$ model

Figures 5.12 and 5.14 show the non-dimensionalized square root of the wall-normal Reynolds stress. Important to remember is that the ϕ variable in the TPM is only exactly equal to v^2, or R_{22}, in flows with a single direction of inhomogeneity. In more complex flows, ϕ should be thought of as a combination of R_{11}, R_{22}, and R_{33} in which ϕ has a matching derivative to each Reynolds stress term in the

direction of that term. Therefore in the impinging jet case, it is expected that ϕ will have a matching derivative to that of v^2 and matching values depend on how close the flow is to having a single direction of inhomogeneity.

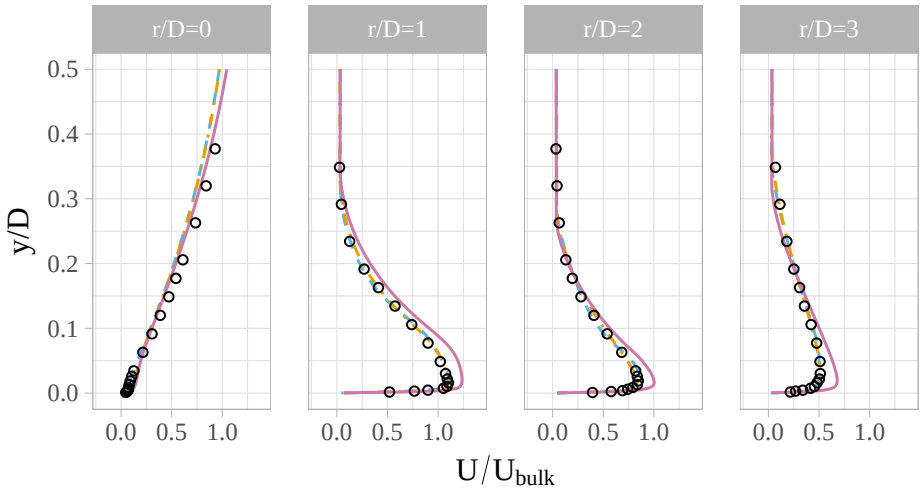

Figure 5.13: Mean velocity of impinging jet at $Re_D = 70000$. (∘) Cooper et al. from ERCOFTAC database [259], (- - - -) Turbulent Potential Model, (–·–·–) $\boldsymbol{v^2 f}$ model, (——) $\boldsymbol{k\omega}$-$\boldsymbol{SST}$ model

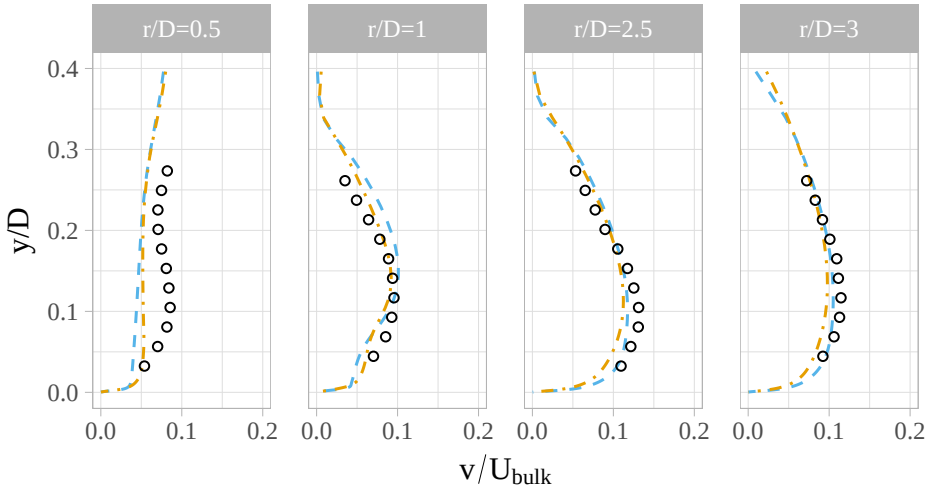

Figure 5.14: Wall-normal Reynolds stress of impinging jet at $Re_D = 70000$. (∘) Cooper et al. from ERCOFTAC database [259], (- - - -) Turbulent Potential Model, (–·–·–) $\boldsymbol{v^2 f}$ model

5.6 s809 Airfoil

The s809 has been conceptually in existence since the early 1980's when it was used to validate the Eppler aerodynamics code in a collaboration between NREL and the Delft University of Technology in 1986 [25]. It is an airfoil with a 21% thickness to chord ratio and was designed with the objectives of having a restrained maximum stall and being insensitive to roughness [25]. More details about the initial experimental validation can be found in Somers [25]. The s809 airfoil has been widely studied [21, 22, 24, 25, 40, 264]

To test the TP model and the effect of rough wall boundaries, the OSU/NREL experiments [264] are used. The computational domain faithfully represents the OSU wind tunnel in 2D and is set up as in figure 5.15. Simulations are run at a chord-based Reynolds number of $1.5e+6$, and inlet turbulence intensity of 0.053% and $y^+ \approx 1$ is at approximately $5e-6m$. Simulation parameters are given in appendix A.

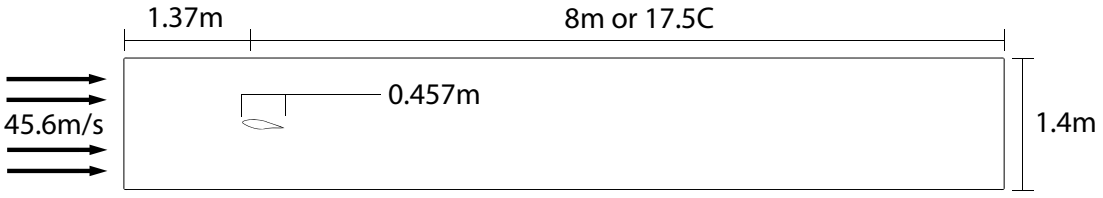

Figure 5.15: Domain description for s809 airfoil simulations

Smooth wall simulations of the s809 airfoil using the Turbulent Potential model are compared to the OSU/NREL data as well as two other common RANS models, $\boldsymbol{k\omega}$-$\boldsymbol{SST}$ and $\boldsymbol{v^2f}$.

Nominal α_p	Actual α_p	U_{Free} *Smooth*	U_{Free} *Rough*
0	0.02	45.90	48.31
4	4.03	45.29	48.34
8	7.97	45.45	48.25
10	10.02	45.20	48.28
14	13.95	45.05	48.13

Table 5.3: s809 test case parameters for smooth and rough simulations

The Turbulent Potential model compares favorably to the other RANS models as well as the OSU/NREL data below. The $\alpha_p = 10$ case is particularly challenging for all the turbulence models because it is on the cusp of separation behavior. Researchers have found that the s809 is more accurately modeled using a separate turbulence transition model in order to capture the laminar to turbulent behavior [154, 265]. Though possibly more representative of flow behavior, these models still involve some degree of tuning and fore-knowledge of transition behavior. Fully turbulent calculations, though less accurate without these explicit transition models, can still return reasonably close approximations to the flow. The Turbulent Potential model has been evaluated for transition-like behavior and more details can be found in Wang and Perot [266].

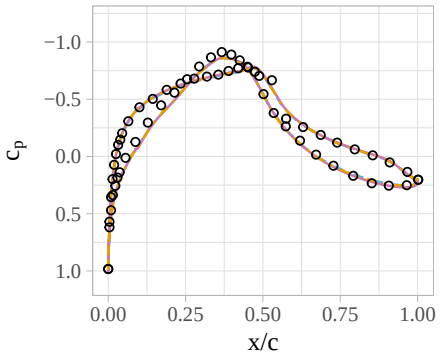

(a) *s809 airfoil at 0.02 degrees*

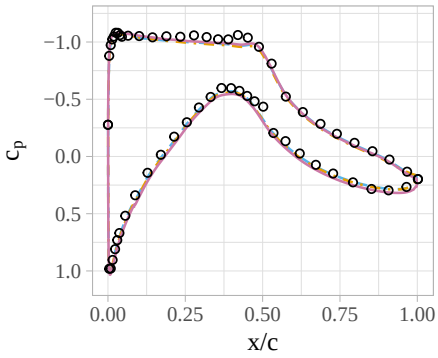

(b) *s809 airfoil at 4.03 degrees*

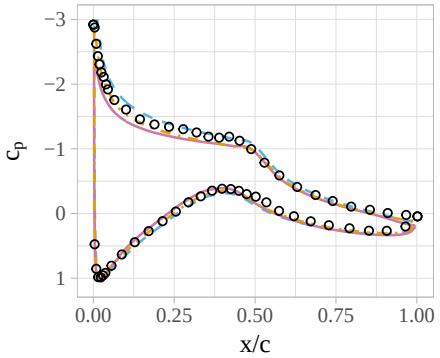

(c) *s809 airfoil at 7.97 degrees*

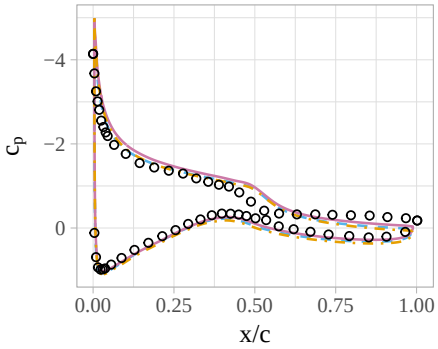

(d) *s809 airfoil at 10.03 degrees*

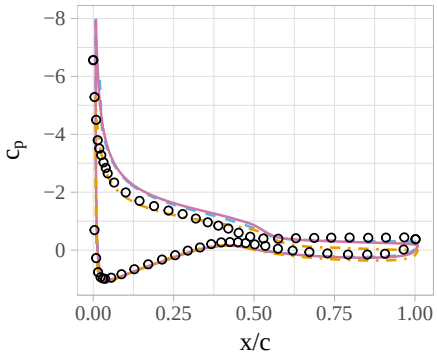

(e) *s809 airfoil at 13.95 degrees*

Figure 5.16: s809 airfoil simulations at various angles of attack. (- - - - -) Turbulent Potential Model, (−·−·−) $\boldsymbol{v^2f}$ model, (——) $\boldsymbol{k\omega}$-$\boldsymbol{SST}$ model, (○) OSU Experimental Data

5.7 Rough Wall s809 Airfoil

Though the s809 was designed to be insensitive to roughness, the application of rough surface features in the OSU/NREL experiments show a minimal but quantifiable difference in C_p. It is this difference that will be examined in this section. The OSU/NREL s809 experiment will be described, then simulations will be validated against experimental results, and lastly the model will be extended to micron-size roughness representing superhydrophobic surfaces.

5.7.1 OSU Experimental Comparison

According to Ramsay [264] the roughness on the Ohio State University s809 was based initially on a molded insect pattern taken from an operational wind turbine. The particle density was 32 particles per square inch in the middle of the pattern, thinning to 8 particles per square inch near the edges. A depiction of the roughness pattern can be found in Ramsay [264]. A template was then made by cutting holes into a steel sheet large enough for one piece of #40 lapidary grit in which to fit. This grit size gave a k/c=0.0019 for the 457mm chord airfoil. Using these parameters and the Dirling correlation in equations 3.13 to 3.15 we arrive at an equivalent sand grain roughness of 0.0008 for these simulations.

Figures 5.17a through 5.17d show the results of the newly developed roughness extension for the Turbulent Potential model compared to both the Ohio State University wind tunnel experiment data and the (light gray) smooth wall simulation for reference. In each case, the C_p curve not only moves in the correct direction,

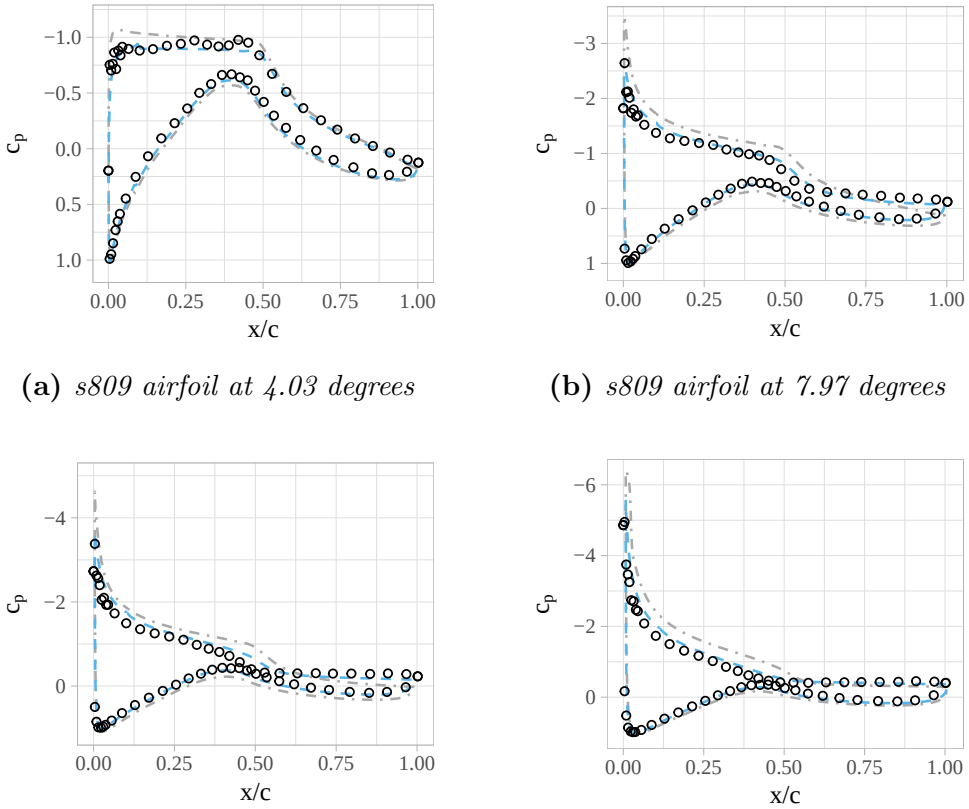

(a) *s809 airfoil at 4.03 degrees*

(b) *s809 airfoil at 7.97 degrees*

(c) *s809 airfoil at 10.03 degrees*

(d) *s809 airfoil at 13.95 degrees*

Figure 5.17: s809 airfoil simulations at various angles of attack with roughness. (- - - - -) Rough Turbulent Potential Model, (—·—·—) Smooth Turbulent Potential Model, (○) Rough OSU Experimental Data

but faithfully represents the rough leading edge experimental data. Though the model should be put through significantly more experimental validation cases, this result, plus the agreement with theoretical velocity deficits, serves as a preliminary validation of the method.

5.7.2 Effect of SHS

Using equations 3.13 through 3.15 an equivalent sand grain height is determined for a 30 micron and a 100 micron regularly spaced roughness. Using the Dirling

			Smooth		Rough		% Reduction	
α	h_R (μm)	k_s (m)	C_l OSU	C_l Sim	C_l OSU	C_l Sim	OSU	Sim
4	0.00087	0.0008	0.62	0.61	0.48	0.51	23	16
8	0.00087	0.0008	0.95	1.05	0.78	0.82	18	22
10	0.00087	0.0008	0.99	1.13	0.80	0.90	19	20
14	0.00087	0.0008	1.1	1.28	0.94	1.05	15	18

Table 5.4: s809 lift comparison between smooth and rough cases

correlation to determine ESG height is an engineering level method at best, and though we make our best guesses for each of the parameters, it cannot be taken as absolutely representational of the rough superhydrophobic surfaces. Given a longer period for study, a parametric examination of the range of parameters feeding the Dirling correlation could give a better idea of the possible solutions. However, as a preliminary step, the results below run counter to the intuition that because the 30 micron surface is well within the viscous sub-layer, it does not have pronounced effect on the overall flow.

The results in figure 5.18 show the 100 micron case is strongly affected by the roughness correction, both at the leading and trailing edges. This likely means that 100 microns is enough to stick out of the viscous sub-layer on most, if not all, of the airfoil. The 30 micron case however shows a similarly strong effect of roughness at the leading edge, but a return to close the smooth wall solution from about 60% of the chord rearward. The stronger velocity gradients and tighter boundary layers at the leading edge are grown to the point where the 30 micron roughness no longer affects the solution.

Table 5.5 gives comparative lift and drag coefficient results for the superhy-

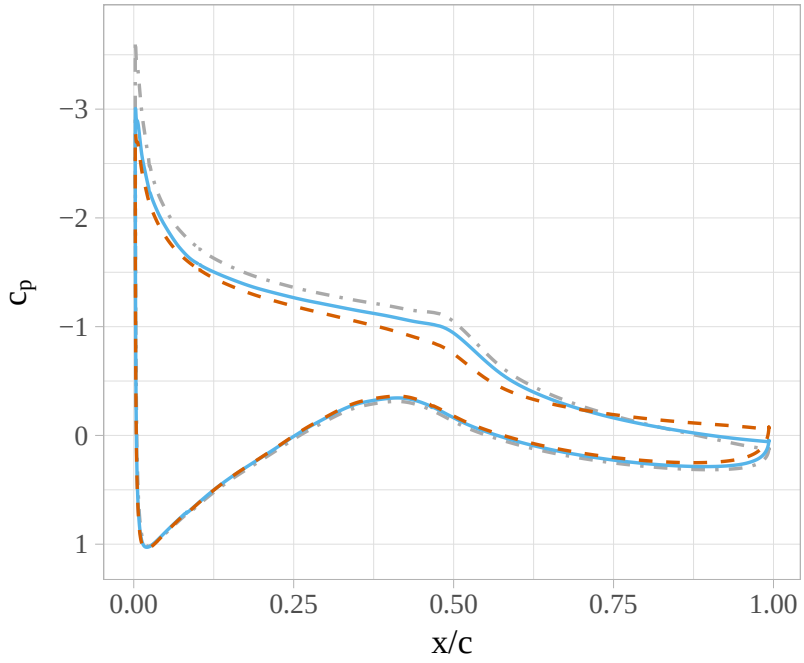

Figure 5.18: Simulation results of an s809 airfoil with micron roughness. SHS ESG roughness heights of (——) 30 microns, (- - - - -) 100 microns, (—·—·—) No roughness.

drophobic surface cases. The larger roughness shows nearly a twenty percent decrease in the lift coefficient for the airfoil section. Despite what intuitively would appear to be minor surface changes, these preliminary simulations lead us to conclude that even small surface irregularities can have significant impacts on the aerodynamics of airfoils in high Reynolds number flow.

Roughness Height (μm)	k_s (m)	C_l	C_l % Diff Smooth	C_d	C_d % Diff Smooth
30	0.00009	0.94	-9.5 %	0.023	+155%
100	0.0003	0.87	-17.1 %	0.028	+211%

Table 5.5: s809 lift and drag coefficient results

5.7.2.1 Estimating the Effect on Turbine Power

Estimation of the impact of SHS surfaces on wind turbine outputs is the desired outcome of this research. A fully resolved boundary layer CFD model of a rotating turbine would be a preferable simulation to this end. However, this computationally expensive investigation was beyond the scope of this work and is discussed in the future work section. A preliminary estimate can be found using the aeroelastic code FAST with lift reductions comparable to those found in the SHS s809 airfoil investigation above. The FAST code, developed at the National Renewable Energy Laboratory, couples aerodynamic, hydrodynamic, servodynamic, and elastic solutions in a wind turbine domain and is an industry standard for such simulations.

Roughness Height (μm)	k_s (m)	P_{pr} : 9 m/s	P_{pr} : 12 m/s
30	0.00009	0.95	1.0
100	0.0003	0.87	0.95

Table 5.6: Coefficient of power comparison using FAST simulations representing SHS surfaces

For the purposes of this work, FAST input parameters are chosen using the definition of a 5MW reference turbine, also developed at NREL [257], with any hydrodynamic models switched off. FAST version 8 (v8) is used in this work. Simulations were run using steady wind speeds of 9 m/s and 12 m/s which, respectively, are below and slightly above the rated wind speed of 11.4 m/s. Lift and drag curves for the aerodynamic part of the model were reduced by 10% and 17% to represent the effect of superhydrophobic surfaces found above. P_{pr} the

percentage reduction of power and is defined as the ratio of the baseline 5MW turbine simulation (with no alteration to lift and drag curves) generator power output to that of the simulations representing the SHS surfaces.

Results confirm a significant reduction of wind turbine power output with reduced lift characteristics at below rated conditions. At 12 m/s (slightly above rated) a minimal impact is shown. At above-rated conditions, this is expected given that the wind turbine is already shedding some available power in the wind in order to spin the generator optimally. At even higher wind speeds, it is presumed that little to no impact would be seen. The OSU roughness experiments show increased percentage lift reduction at lower angles of attack. Accuracy of the predictions above might improve if the constant 10% and 17% lift reductions were replaced with values that vary with angle of attack.

CHAPTER 6

FURTHER WORK AND CONCLUSION

6.1 Roughness

Preliminary work on the theory and implementation of the equivalent sand grain roughness method in the Turbulent Potential model has resulted in some promising results. Several aspects of the model could be improved, and there are many future directions the research could take. First and foremost, a roughness function for ϕ/k that better approximates the theoretical curve should be developed. Currently, the method is really only appropriate for roughness sizes well within the log layer. However, the large roughness corrections, i.e. at $k_s^+ > 300$, could be considered theoretically tenuous given that blockage effects of the roughness will become much more prevalent at these heights. Therefore would it not be prudent to re-mesh with an extended surface and smaller effective roughness? These questions could be answered by further study of the topic.

A practical new avenue for this research could be the implementation of a set of non-uniform roughness boundary conditions in OpenFOAM. At certain points during the course of this study, the author desired to control the roughness height as a function of the spatial directions, but the current implementation is either on or off. A mean roughness height is assigned to the entire patch.

Also interesting to explore would be a non-dimensional calculation of the the

RANS roughness boundary layer following the work of Aupoix [219] but directly for the Turbulent Potential model. This might shed some of the ambiguity present in the current work, wherein the initial $\varepsilon|_w$ formulations were actually design for $\omega|_w$. These could also use a roughness function directly from Flack and Schultz [193] that appears to be a useful compromise between the Nikuradse and Colebrook data and subsequent correlations.

The methods in this work could also be extended to finding rough surface boundary expressions for the elliptic Turbulent Potential model, as well as the $\boldsymbol{v^2 f}$ model. This would involve finding a rough wall expression for elliptically damped pressure strain/dissipation term f.

And finally, simulating a range of airfoils with varying roughness characteristics could be very interesting for use in a FAST/OpenFAST simulation in order to calculate the effect to which certain rough airfoils and their positioning affect the power output of a wind turbine.

6.2 Turbulent Potential Model

Though the Turbulent Potential model has been described in journal publications and applied to many test cases, it has not yet gone through the rigorous rounds of testing that would lead the broader research community to consider it a mature model. Langley Research Center (NASA) operates a "Turbulence Modeling Resource" wherein turbulence models are given a Model Readiness Rating (MRR) as a measure of their maturity and acceptance. Higher rated models have been

through multiple rounds of testing and have achieved certain benchmarks that bolster their believability. In order for the Turbulent Potential model to see more widespread use, it is recommended that it be put through such a process.

Concerning model development, core areas needing future attention are the production model(s), the turbulence Reynolds dependent dissipation and pressure strain, and the elliptic damping version as a whole. As is clear in the production model section of this work, the TKE production term, as well as the production terms in the turbulent potentials, are missing portions of the full term. This is especially true in three dimensional flow. The mixed production terms presented are an ad-hoc fix that could be improved upon with further research.

The Turbulent Potential model transition modifications were intentionally left out of this work, given than they were found to be inconsistent with a tensor version of the model. Replacement terms were identified but not tested to the point of trusting their efficacy and accuracy. Future work should examine these terms and rigorously test them in transitional flows.

Mathematically, the Turbulent Potential model relies on stripping the extraneous information from the $\nabla \cdot R$ term in the RANS equations. This effectively gives the solution a directionality that relates to wall-normal physics and shearing physics (ϕ and $\boldsymbol{\psi}$ respectively). It is thought that there may be a coordinate system that aligns with these physical processes, such that calculations in this new coordinate system would be highly simplified over their Cartesian tensor counterparts. The Frenet-Serret coordinate frame was identified as a candidate for this

transformation, however significant amounts of testing did not yield any working results. Future study is warranted to explore possible solutions in this area.

6.3 NREL Phase VI Experiment

It was hoped that there would be opportunity to use the NREL Phase VI as a test simulation for rough surface airfoil blades using the Turbulent Potential model. This however did not come to fruition during the research period. The background work with relation to roughness parameters is described below with the aim that future work on the project may find it useful. The Phase VI experiment has been used by many researchers as experimental validation [20, 79, 81, 86, 142, 143, 149, 152, 156, 161, 165, 167, 267–273]. The experiment is described in Hand et al. [20, 274].

Figure 6.1: NREL Phase VI wind turbine at the NASA Ames wind tunnel

Sectional properties for the blade model are taken from table 5.1 in [275]. The Phase VI turbine is a modified Grumman Wind Stream 33 rated at 20kW [274]. The properties in table 6.1 describe the experiment.

Number of blades	2
Rotor Diameter	10.058m
Rotor speed (nominal)	71.63rpm
Hub Height	12.192m
Rotor Overhang	1.401m(yaw-axis to blade-axis)
Tower Height	11.5m but 11.14m above floor
Tower Outer diameter (base)	0.6096m
Tower Outer diameter (top)	0.4064
Tunnel Width	120ft (36.576m)
Tunnel Height	80ft (24.384m)
Inlet Turbulence Intensity	0.5%

Table 6.1: NREL Phase VI experiment properties

Preliminary work, shown in figure 6.2, using the Spalart-Allmaras (SA) model and a wall function approach gave reasonable results for the flow field around the blade at a freestream velocity of 10m/s. The NREL Phase VI experiment would be the primary vehicle for comparing rough versus smooth surface rotor modeling.

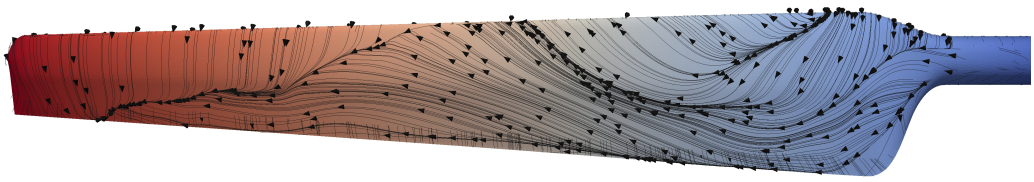

Figure 6.2: CFD simulation of the NREL Phase VI wind turbine using SA with wall functions, limiting streamlines result

Using equation 3.5 the NREL Phase VI turbine viscous sublayer height is plotted along the span of the blade. Assuming no spanwise flow, SHS asperity reference heights of $y = 30\mu m$ and $y = 100\mu m$ are plotted in figure 6.3 to show that indeed

some heights of SHS would protrude out of the viscous sublayer and interrupt turbulence production in the buffer layer.

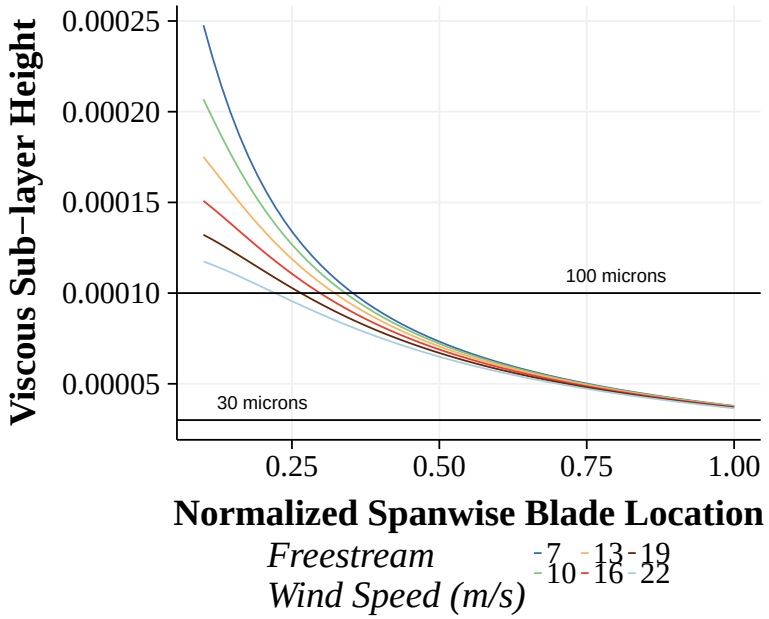

Figure 6.3: Viscous sublayer height along the NREL Phase VI blade at various freestream velocities

A new mesh was developed that allows for boundary layer resolved computation of the NREL Phase VI wind turbine with blade boundary cells on the order of $y^+ \approx 1$. Due to time and computing restraints, this mesh was not run for this research project, but will hopefully be used in the future to examine the roughness losses for an entire turbine model.

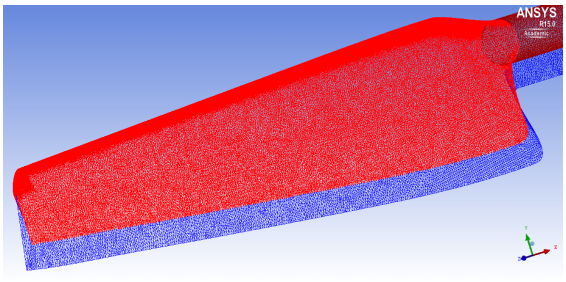

(a) *Wireframe of blade and trailing inner wall on which to grow prism elements*

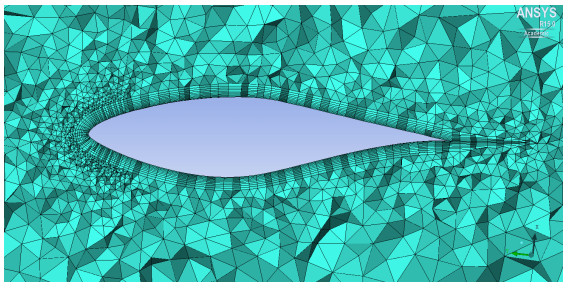

(b) *Mesh cut plane showing boundary layer*

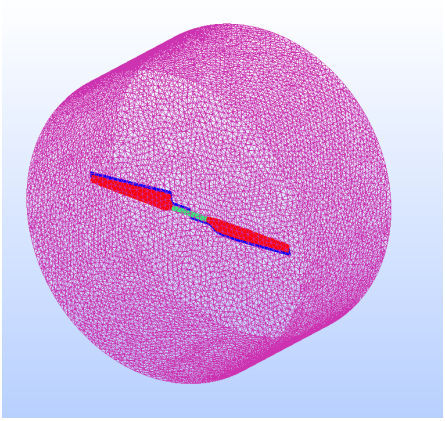

(c) *Rotating portion of the mesh*

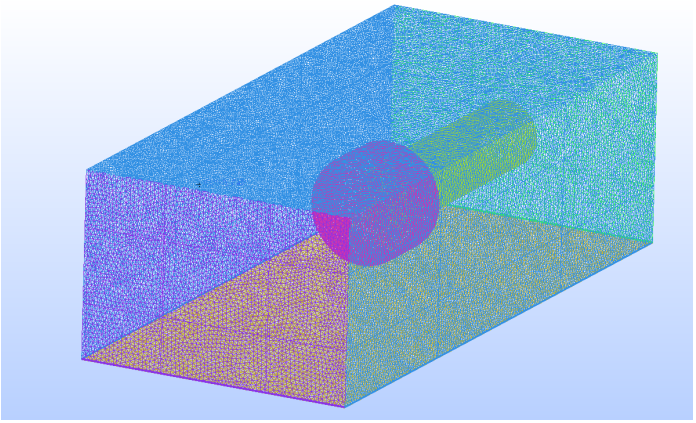

(d) *Farfield portion of the mesh*

Figure 6.4: Four views of the NREL Phase VI mesh

6.4 Conclusion

Airfoil data is regularly used in many aspects of wind turbine research. From actuator line methods embedded in large domain wake analysis tools like SOWFA, to FAST/OpenFAST blade element momentum methods developed at NREL, to potential flow simulations using lifting lines, airfoil data is at the crux of determining the forces exerted on the flow. The work carried out in this manuscript could be useful in developing more real-world sets of airfoil data, combining accurate airfoil simulation with a parameterized roughness, without the need to carry out expensive wind tunnel testing. Design methods could be developed that rely on rough surface airfoil simulations with roughnesses that grow over time. It is the hope of the author that these methods become incorporated into design tools that no longer predict the power output of a wind turbine with perfectly smooth airfoils, but that represent a more realistic view of wind turbines that exist in a larger environment.

The primary goal of this dissertation, to incorporate rough surface boundary conditions into the Turbulent Potential model has been accomplished. The approach, combining equivalent sand grain methods from other RANS models with a relation determined from DNS, has been shown to accurately represent velocity shifts in plane channel flow and leading edge roughness on the s809 airfoil. It was determined that the methods used for other RANS models needed adaptation for use in the Turbulent Potential Model, especially the wall value of dissipation in the transitionally rough regime. These results were then extended to examine

and make a guess at whether superhydrophobic surface roughness would have a significant impact on an airfoil aerodynamics. It was shown that indeed, regular roughness at 30 microns and 100 microns high does have an impact on the flow-field around and s809 airfoil. These aims, approach, and results were placed in the context of computational modeling for wind turbines more broadly.

Secondarily, modifications to the Turbulent Potential model were presented. Simulations of plane channel flow at multiple turbulence Reynolds numbers verified that the modifications were implemented correctly and represented a simplified boundary layer with a reasonable degree of accuracy. Impinging jet simulations showed that in the lower Reynolds number case, both the Turbulent Potential model and the elliptic Turbulent Potential model represented the flow field and heat transfer accurately. More investigation will be necessary to deal with inaccuracies present in the higher Reynolds number case, though these issues are present with all the turbulence models presented, so the answer may be elsewhere.

APPENDICES

APPENDIX A

TURBULENT POTENTIAL EQUATIONS

A.1 Current Work

$$\frac{Dk}{Dt} = \nabla \cdot (\nu + \nu_t \bar{\sigma_k}) \nabla k + P - \varepsilon \tag{A.1}$$

$$\frac{D\epsilon}{Dt} = \nabla \cdot (\nu + \nu_t \bar{\sigma_\epsilon}) \nabla \varepsilon + \frac{\hat{\varepsilon}}{k}(C_{\epsilon 1} P - C_{\epsilon 2}\varepsilon + C_{\epsilon 3} P_{3D}) \tag{A.2}$$

$$\begin{aligned}\frac{D(\phi/k)^{1/2}}{Dt} = \nabla \cdot (\nu + \nu_t \bar{\sigma_\phi}) \nabla (\phi/k)^{1/2} - \frac{1}{2}(1 - C_{p2})(\phi/k)^{1/2}\frac{P}{k} \\ + \frac{1}{2}(C_{p1}\frac{\nu_t}{\nu_t + 10\nu})\frac{\hat{\varepsilon}}{k}(2\alpha - 1)(\phi/k)^{1/2}\end{aligned} \tag{A.3}$$

$$\begin{aligned}\frac{D(\psi/k)}{Dt} = \nabla \cdot (\nu + \nu_t \bar{\sigma_\psi}) \nabla (\psi/k) + C_{p4}(2\alpha - 1)\frac{\phi}{k}\omega - C_{p3}\alpha(\psi/k)\frac{P}{k} \\ - C_{p1}\frac{\nu_t}{\nu_t + 10\nu}\frac{\hat{\varepsilon}}{k}(1 - \alpha)(\psi/k) - (1 - C_{p2})(\psi/k\frac{P}{k} - \frac{\phi}{k}\omega) \\ + C_R\frac{(1 - \alpha)k}{\nu/C_\lambda + \sqrt{\nu_t \nu}}\psi/k\end{aligned} \tag{A.4}$$

$$\frac{P}{k} = \frac{\psi}{k} \cdot \omega, \quad P_{3D} = |\frac{\psi}{k} \times \omega|, \quad \frac{\hat{\varepsilon}}{k} = \varepsilon/(1 + 10\nu\nabla\sqrt{k})$$

$$\nu_t = (\tfrac{1}{2}(0.12 + 0.37\lambda)\phi/k + \tfrac{1}{2}\tfrac{\psi}{k} \cdot \tfrac{\psi}{k})\frac{k^2}{\varepsilon}, \quad \alpha = (1 + 1.5\frac{\phi}{k})^{-1} \quad \lambda = (1 + C_\lambda\sqrt{\nu_t/\nu})^{-1}$$

Where model constants are:

$$C_\mu = 0.21, \quad C_{p1} = 1.9, \quad C_{p2} = 3/5, \quad C_{p3} = 2.0, \quad C_{p4} = 0.21$$

$$C_{\epsilon 1} = 1.45 + 0.05(2\alpha - 1), \quad C_{\epsilon 2} = 1.83, \quad C_{\epsilon 3} = 0.15, \quad C_R = 0.0^*$$

$$\bar{\sigma_k} = 1.0, \quad \bar{\sigma_\epsilon} = 0.83, \quad \bar{\sigma_\phi} = 0.33, \quad \bar{\sigma_\psi} = 1.0, \quad C_\lambda = 0.33$$

A.2 Are et al. [243]

$$\frac{Dk}{Dt} = \nabla \cdot (\nu + \nu_t \bar{\sigma_k}) \nabla k + P - \varepsilon \tag{A.5}$$

$$\frac{D\epsilon}{Dt} = \nabla \cdot (\nu + \nu_t \bar{\sigma_\epsilon}) \nabla \varepsilon + \frac{\hat{\varepsilon}}{k}(C_{\epsilon 1} P - C_{\epsilon 2}\varepsilon + C_{\epsilon 3} P_{3D}) \tag{A.6}$$

$$\begin{aligned}\frac{D(\phi/k)^{1/2}}{Dt} = \nabla \cdot (\nu + \nu_t \bar{\sigma_k}) \nabla (\phi/k)^{1/2} - \frac{1}{2}(1 - C_{p2})(\phi/k)^{1/2}\frac{P}{k} \\ + \frac{1}{2} C_{p1} \frac{\nu_t}{\nu_t + 10\nu} \frac{\hat{\varepsilon}}{k}(2\alpha - 1)(\phi/k)^{1/2}\end{aligned} \tag{A.7}$$

$$\begin{aligned}\frac{D(\psi/k)}{Dt} = \nabla \cdot (\nu + \nu_t) \nabla (\psi/k) + 0.21(2\alpha - 1)\frac{\phi}{k}\omega - C_{p3} 2\alpha (\psi/k)\frac{P}{k} \\ - C_{p1} \frac{\nu_t}{\nu_t + 10\nu} \frac{\hat{\varepsilon}}{k}(1 - \alpha)(\psi/k) - (1 - C_{p2})(\psi/k \frac{P}{k} - \frac{\phi}{k}\omega)\end{aligned} \tag{A.8}$$

$$\frac{P}{k} = \frac{\psi}{k} \cdot \omega, \quad P_{3D} = |\frac{\psi}{k} \times \omega|, \quad \frac{\hat{\varepsilon}}{k} = \varepsilon / (1 + 10\nu \nabla \sqrt{k})$$

$$\nu_t = C_\mu \frac{\phi k}{\varepsilon}, \quad \alpha = (1 + 1.5\frac{\phi}{k})^{-1}$$

Where model constants are:

$$C_\mu = 0.21, \quad C_{p1} = 1.7, \quad C_{p3} = 0.12$$

$$C_{\epsilon 1} = 1.45, \quad C_{\epsilon 2} = 1.83 - 0.16 e^{\left(-0.1 \frac{k^2}{\nu \varepsilon}\right)}, \quad C_{\epsilon 3} = 0.15$$

$$\bar{\sigma_k} = 0.33 + 0.67 \frac{P}{\hat{\varepsilon}}, \quad \bar{\sigma_\epsilon} = 0.33 + 0.5 \frac{P}{\hat{\varepsilon}}$$

A.3 Elliptic Turbulent Potential

$$\frac{Dk}{Dt} = \nabla \cdot (\nu + \nu_t \sigma_k) \nabla k + P - \varepsilon \tag{A.9}$$

$$\frac{D\varepsilon}{Dt} = \nabla \cdot (\nu + \nu_t \sigma_\epsilon) \nabla \varepsilon + (C_{\epsilon 1} P - C_{\epsilon 2} \varepsilon)/T \tag{A.10}$$

$$L^2 \nabla^2 f - f = -\Pi_\eta \tag{A.11}$$

$$\frac{D\eta}{Dt} = \nabla \cdot (\nu + \nu_t \sigma_\phi) \nabla \eta + min[f, \Pi_\eta] - \frac{P}{k}\eta \tag{A.12}$$

$$\frac{D\xi}{Dt} = \nabla \cdot (\nu + \nu_t \sigma_\psi) \nabla \xi + \eta \boldsymbol{\omega} - \frac{P}{k}\xi - \Pi_\xi - (1 - \lambda_\xi)\xi/T + C_R \frac{(1-\alpha)k}{\nu/C_\lambda + \sqrt{\nu_t \nu}}\xi \tag{A.13}$$

$$\Pi_\eta = (C_{p1} - 1)\frac{1}{T}(\tfrac{2}{3} - \eta) + C_{p2}\frac{2}{3}\frac{P}{k} + \frac{\varepsilon}{k}\eta + \frac{\nu_t}{\nu + \nu_t}((\tfrac{2}{3} - \eta)^2 + \xi \cdot \xi - \frac{2}{3} II_b)/T \tag{A.14}$$

$$\Pi_\xi = C_{p1}\xi f_d/T + C_{p2}\eta\omega + (C_{p3} - 0.12\lambda_\xi)\frac{P}{k}\xi + \frac{\nu_t}{\nu + \nu_t}((\tfrac{2}{3} - \eta)^2 + (\tfrac{2}{3} - \chi)^2)\xi/T \tag{A.15}$$

$$L = C_{L1} max\left[\frac{k^{3/2}}{\varepsilon}, C_{L2}\left(\frac{\nu^3}{\varepsilon}\right)^{\frac{1}{4}}\right] \qquad T = max\left[\frac{k}{\varepsilon}, 6.0\left(\frac{\nu}{\varepsilon}\right)^{\frac{1}{2}}\right] \tag{A.16}$$

$$P = \boldsymbol{\psi} \cdot \omega \qquad \hat{\varepsilon} = \varepsilon/(1 + 10\nu\frac{|\nabla k^{1/2}|}{k}) \tag{A.17}$$

$$\lambda_\xi = \left(1 + 0.33\left(\frac{C_\mu \eta k^2}{\nu\varepsilon}\right)^{\frac{1}{2}}\right)^{-1} \qquad \nu_t = (0.6(0.12 + (1-\alpha)\lambda_\xi)\eta + 0.4(\xi \cdot \xi))\frac{k^2}{\varepsilon} \tag{A.18}$$

$$\chi = \tfrac{4}{3}(1.75\alpha - 0.375) \qquad II_b = (2\alpha - 1)^2 + 2(\xi \cdot \xi) \tag{A.19}$$

$$\alpha = (1 + 1.5\eta)^{-1} \qquad f_d = tanh\left[\frac{f}{\Pi_\eta}\right] \tag{A.20}$$

Where model constants are:

$$\sigma_k = 1.0, \quad \sigma_\epsilon = 0.83 \quad \sigma_\phi = 0.4 \quad \sigma_\psi = 1.0$$
$$C_\mu = 0.21, \quad \beta_k = 0.09, \quad C_{p1} = 1.4 - \lambda_\xi, \quad C_{p2} = 0.45, \quad C_3 = 1.8, \quad C_R = 0.0*$$
$$C_{\varepsilon 1} = 1.45 + 0.09(2\alpha - 1), \quad C_{\varepsilon 2} = 1.83, \quad C_{\varepsilon 3} = 0.15, \quad C_{L1} = 0.3 \quad C_{L2} = 75.0$$
$$C_t = 0.04(1 - \Lambda_r)\sqrt{\tfrac{\nu_t}{\nu}}$$

APPENDIX B

S809 SIMULATION PARAMETERS

Common

	Inlet	Outlet	Tunnel Walls	Airfoil Walls	Initial
U	¡45.6,0,0¿	Zero gradient	Zero Gradient	No-slip	¡45.6,0,0¿
p	Zero gradient	0.0	Zero gradient	Zero gradient	0.0
ν_T	7.265e-6	Zero gradient	Zero gradient	0.0	7.265e-6

Spalart-Allmaras

	Inlet	Outlet	Tunnel Walls	Airfoil Walls	Initial
$\tilde{\nu}$	$5\nu_T$	Zero gradient	Zero gradient	0.0	$5\nu_T$

K-Omega SST

	Inlet	Outlet	Tunnel Walls	Airfoil Walls	Initial
k	0.0078	Zero gradient	Zero gradient	Zero Gradient	0.0078
ω	9.659	Zero gradient	Zero gradient	$\sqrt{(6\nu/\beta_1 y^2)^2 + (\sqrt{k}/{C_{mu}}^{0.25}\kappa y)^2}$	9.12

v2f

	Inlet	Outlet	Tunnel Walls	Airfoil Walls	Initial
k	0.0078	Zero gradient	Zero gradient	0.0	0.0078
ε	0.0035	Zero gradient	Zero gradient	$2\nu k/y^2$	0.0035
v^2	0.67k	Zero gradient	Zero gradient	0.0	0.57k
f	0.0	Zero gradient	0.0	0.0	0.0

Turbulent Potential

	Inlet	Outlet	Tunnel Walls	Airfoil Walls	Air Initial Condition
k	0.0078	Zero gradient	Zero gradient	0.0	0.0078
ε	0.0035	Zero gradient	Zero gradient	$2\nu\sqrt{\lvert k^{0.5}\rvert}$	0.0035
ϕ/k	0.57	Zero gradient	Zero gradient	0.0	0.57
ψ/k	¡0,0,0,¿	Zero gradient	Zero gradient	¡0,0,0,¿	¡0,0,0,¿

APPENDIX C

WIND TURBINE VISCOUS SUBLAYER HEIGHT

The figures below describe SHS height (red) vs. viscous sub-layer and buffer layer heights for two wind turbines for freestream velocities of 1m/s - 25m/s.

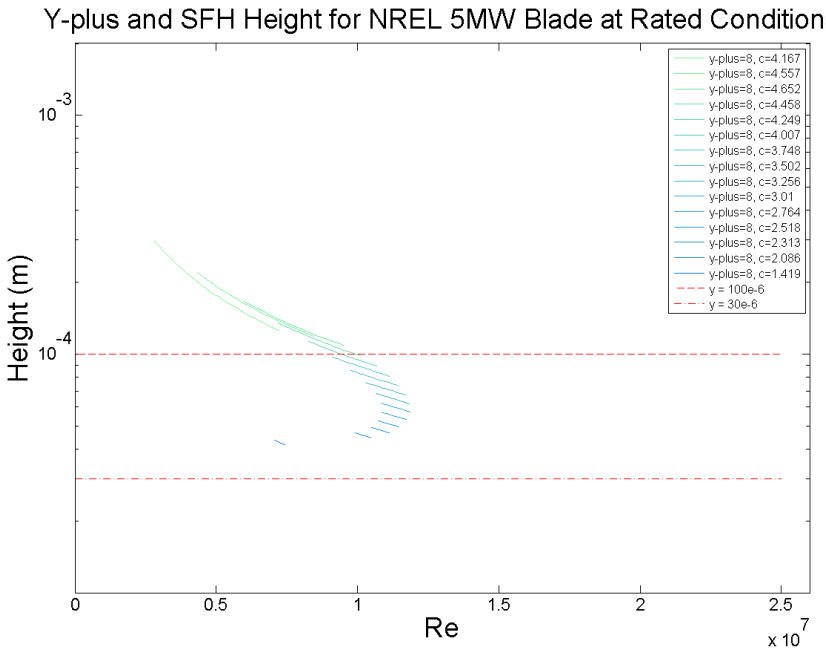

Figure C.1: Height of the viscous sub-layer $y^+ \approx 8$ (green/blue) compared to the height of SHS asperities (red)

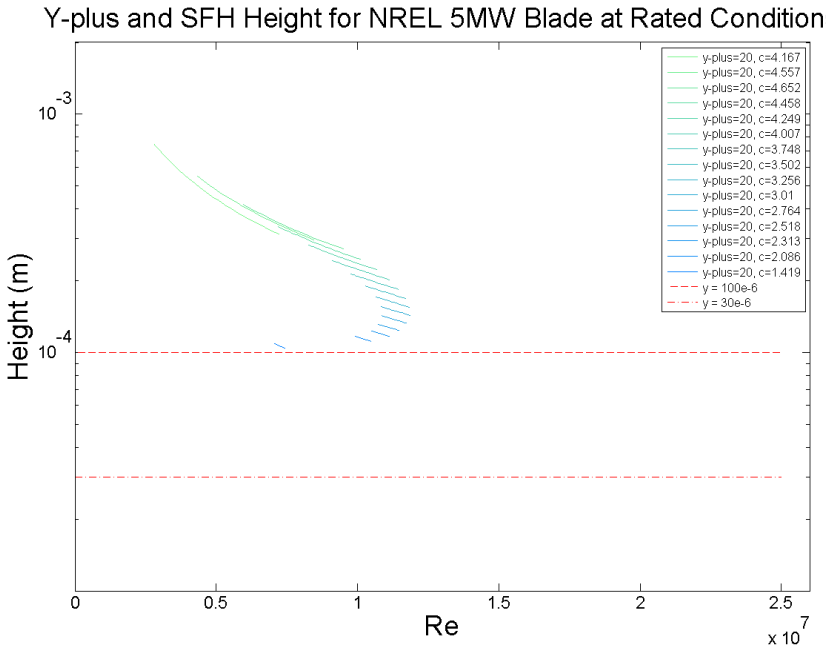

Figure C.2: Height of the buffer layer $y^+ \approx 20$ (green/blue) compared to the height of SHS asperities (red)

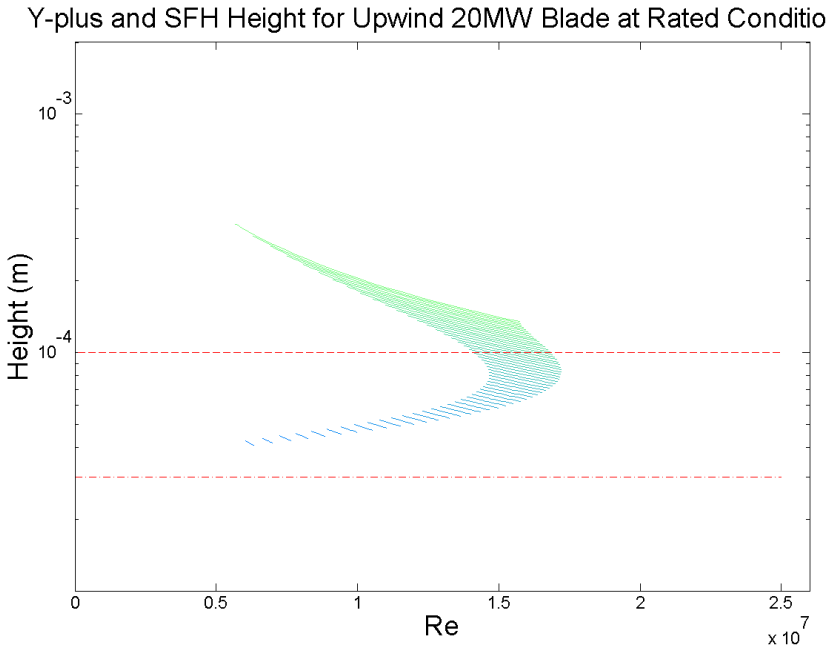

Figure C.3: Height of the viscous sub-layer $y^+ \approx 8$ (green/blue) compared to the height of SHS asperities (red)

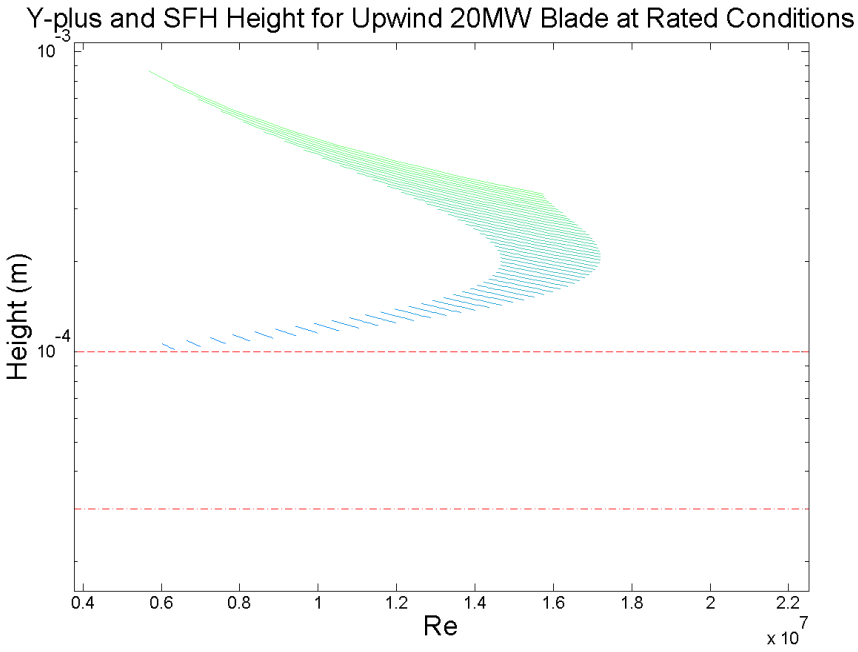

Figure C.4: Height of the buffer layer $y^+ \approx 20$ (green/blue) compared to the height of SHS asperities (red)

APPENDIX D

INITIAL WORK WITH WALL FUNCTIONS

Smooth wall calculations of the s809 airfoil using a wall function approach.

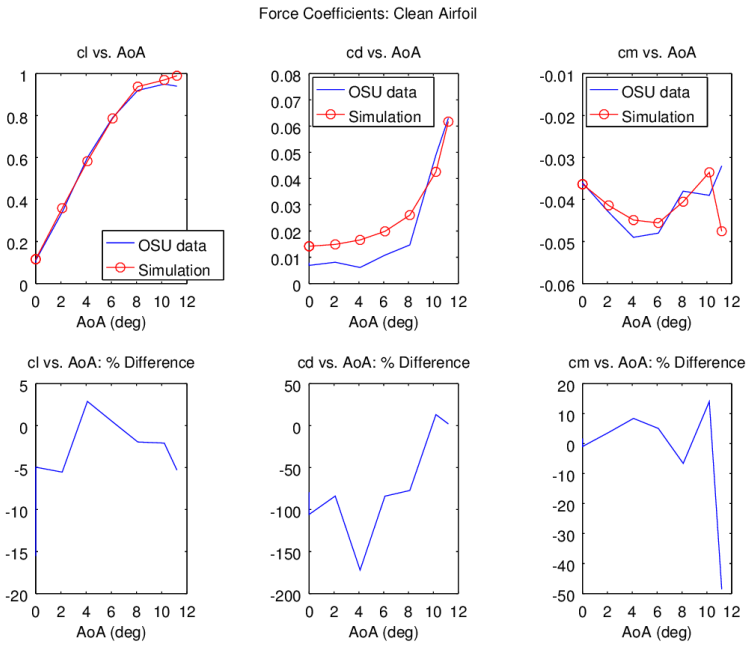

Figure D.1: Smooth Airfoil

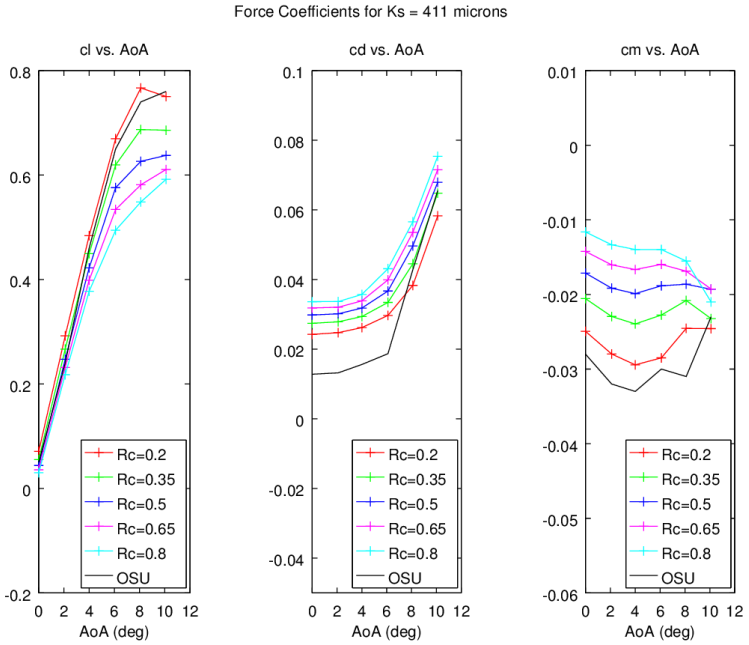

Figure D.2: Rough Airfoil $k_s = 411\ microns$

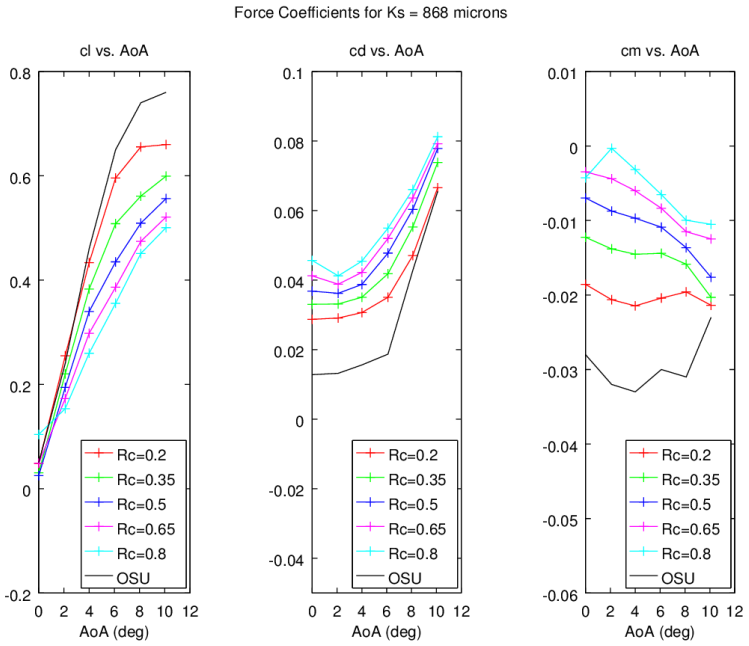

Figure D.3: Rough Airfoil $k_s = 868\ microns$

APPENDIX E

NOTE ON SEPARATION CORRECTION C_R

The issue of separation length on the NASA wall-mounted hump validation case has been given much attention [276]. Most RANS models overpredict the separation length even in the baseline case [277]. Rumsey and Jeyapaul [278] tried to fix this in their SSG pressure-strain model by modifying the C_3 constant (looks like $C_3 k S_{ij}$). The general strategy pf such modifications is to encourage the growth of Reynolds shear stress in separation regions whilst having little to no effect on boundary layer flow. The constant stated in the TPM definitions above, $C_R = 0.0*$, has an asterisk next to the zero because this term was developed encourage shear stress growth in separation regions. This term worked to increase ψ separation region of the wall-mounted hump case, shortening the distance of the reattachment point from the hump. However, this term also prevented the higher angle of attack s809 simulations from separating, negating its usefulness as a correction. Further work must be done to explore this correction, or another like it, such that a term can be developed that both works for separating humps and airfoils.

BIBLIOGRAPHY

1. Altemus, J. D. *Deicing Device For Airplane Propellers, Winds, And The Like* 1943.

2. Parent, O. & Ilinca, A. Anti-icing and de-icing techniques for wind turbines: Critical review. *Cold Regions Science and Technology* **65,** 88–96. ISSN: 0165232X (2011).

3. GL Renewables Certificati. *Technical Note: Certification of Wind Turbines for Extreme Temperatures* tech. rep. (Germanischer Lloyd Industrial Services GmbH, Hamburg, 2013).

4. Baring-Gould, I. *et al. Wind Energy Projects in Cold Climates* tech. rep. (International Energy Agency, 2012), 1–43.

5. Dalili, N., Edrisy, A. & Carriveau, R. A review of surface engineering issues critical to wind turbine performance. *Renewable and Sustainable Energy Reviews* **13,** 428–438. ISSN: 13640321 (2009).

6. Tammelin, B. *et al.* Wind energy production in cold climate (WECO). *ETSU contractor's report W/11/00452/REP, UK DTI,* 1–38 (1999).

7. Salam, A., Alsabagh, Y, Tiu, W., Xu, Y. & Virk, M. S. A Review of the Effects of Ice Accretion on the Structural Behavior of Wind Turbines, 59–70 (2013).

8. Suddath, C. *A Brief History of: Velcro* 2010. `http://content.time.com/time/nation/article/0,8599,1996883,00.html` (2016).

9. Vincent, J. F., Bogatyreva, O. A., Bogatyrev, N. R., Bowyer, A. & Pahl, A.-K. Biomimetics: its practice and theory. *Journal of The Royal Society Interface* **3,** 471–482. ISSN: 1742-5689 (2006).

10. Barthlott, W. & Neinhuis, C. Purity of the sacred lotus, or escape from contamination in biological surfaces. *Planta* **202,** 1–8. ISSN: 00320935 (1997).

11. Cheng, Y.-T. & Rodak, D. E. Is the lotus leaf superhydrophobic? *Applied Physics Letters* **86,** 144101. ISSN: 00036951 (2005).

12. Li, X.-M., Reinhoudt, D. & Crego-Calama, M. What do we need for a superhydrophobic surface? A review on the recent progress in the preparation of superhydrophobic surfaces. *Chemical Society Reviews* **36,** 1350. ISSN: 0306-0012 (2007).

13. Jung, S. *et al.* Are superhydrophobic surfaces best for icephobicity? *Langmuir : the ACS journal of surfaces and colloids* **27,** 3059–66. ISSN: 1520-5827 (2011).

14. Boinovich, L. B. & Emelyanenko, A. M. Anti-icing potential of superhydrophobic coatings. *Mendeleev Communications* **23,** 74–75. ISSN: 09599436 (2013).

15. Farhadi, S., Farzaneh, M. & Kulinich, S. Anti-icing performance of superhydrophobic surfaces. *Applied Surface Science* **257,** 6264–6269. ISSN: 01694332 (2011).

16. Cao, L., Jones, A. K., Sikka, V. K., Wu, J. & Gao, D. Anti-Icing superhydrophobic coatings. *Langmuir* **25,** 12444–12448. ISSN: 07437463 (2009).

17. Bons, J. P. A Review of Surface Roughness Effects in Gas Turbines. *Journal of Turbomachinery* **132,** 1–16. ISSN: 0889504X (2010).

18. Esterly, S., Gelman, R. & Haas, K. *2013 Renewable Energy Data Book* tech. rep. (U.S. Department of Energy, National Renewable Energy Laboratory, 2015).

19. Musial, W. & Ram, B. *Large-Scale Offshore Wind Power in the United States: Assessment Of Opportunities And Barriers* tech. rep. September (National Renewable Energy Laboratory, 2010), 1–240.

20. Simms, D, Schreck, S, Hand, M & Fingersh, L. J. *NREL Unsteady Aerodynamics Experiment in the NASA-Ames Wind Tunnel : A Comparison of Predictions to Measurements* tech. rep. June (National Renewable Energy Laboratory, Golden, Colorado, 2001).

21. Wolfe, W. P. & Ochs, S. S. CFD calculations of S809 aerodynamic characteristics, 1–8 (1997).

22. Guerri, O., Bouhadef, K. & Harhad, A. Turbulent Flow Simulation of the NREL S809 Airfoil. *Wind Engineering,* 287–302 (2006).

23. Pape, a. L. & Lecanu, J. 3D Navier-Stokes computations of a stall-regulated wind turbine. *Wind Energy* **7,** 309–324. ISSN: 1095-4244 (2004).

24. Gupta, S. & Leishman, J. G. Validation Of A Free-Vortex Wake Model For Wind Turbines In Yawed Flow. *A collection of technical papers; 44th AIAA Aerospace Sciences Meeting, Reno, Nevada,* 4529–4543 (2006).

25. Somers, D. M. & Tangler, J. *Design and Experimental Results for the S809 Airfoil* tech. rep. January 1997 (National Renewable Energy Laboratory, Golden, Colorado, 1997), 1–97.

26. Wilson, R. E. & Lissaman, P. B. S. *Applied Aerodynamics Of Wind Power Machines* tech. rep. (Oregon State University, 1974).

27. Manwell, J. F., McGowan, J. G. & Rogers, A. L. *Wind Energy Explained* 2nd, 1–675 (John Wiley & Sons, West Sussex, United Kingdom, 2009).

28. Van Kuik, G. a. M. An inconsistency in the actuator disc momentum theory. *Wind Energy* **7,** 9–19. ISSN: 10954244 (2004).

29. Hansen, A. & Butterfield, C. Aerodynamics of horizontal-axis wind turbines. *Annual Review of Fluid Mechanics* **25,** 115–149 (1993).

30. *Wind Turbine Technology: Fundamental Concepts of Wind Turbine Engineering* (ed Spera, D.) (ASME Press, New York, 1994).

31. Glauert, H. in *Aerodynamic Theory Vol. IV* (ed Durand, W.) 169–360 (Springer, New York, 1935).

32. Leishman, J. G. *Principles of Helicopter Aerodynamics* (Cambridge University Press, Cambridge, UK, 2006).

33. Theodorsen, T. *Theory of Propellers* 1st (McGraw-Hill, New York, 1948).

34. Johnson, W. *Helicopter Theory* reprint (Courier Dover Publications, 2012).

35. Hansen, M. O. L. *Aerodynamics of Wind Turbines* 2nd (Earthscan, London, UK, 2008).

36. Burton, T., Sharpe, D., Jenkins, N. & Bossanyi, E. *Wind Energy Handbook* (John Wiley & Sons, Ltd, Chichester, UK, 2001).

37. Sørensen, J. N. Aerodynamic Aspects of Wind Energy Conversion. *Annual Review of Fluid Mechanics* **43,** 427–448. ISSN: 0066-4189 (2011).

38. Gupta, S. & Leishman, J. G. Comparison of Momentum and Vortex Methods for the Aerodynamic Analysis of Wind Turbines. *43rd AIAA Aerospace Sciences Meeting and Exhibit* **AIAA 2005-,** 1–24 (2005).

39. Hansen, M. O. L. & Aagaard Madsen, H. Review Paper on Wind Turbine Aerodynamics. *Journal of Fluids Engineering* **133,** 114001. ISSN: 00982202 (2011).

40. Tangler, J. L. The Nebulous Art of Using Wind Tunnel Aerofoil Data for Predicting Rotor Performance†. *Wind Energy* **5,** 245–257. ISSN: 1099-1824 (2002).

41. Buhl, M. L. *A Comparison of Wind Turbine Aeroelastic Codes Used for Certification Preprint* tech. rep. (2006).

42. Snel, H. Review of the present status of rotor aerodynamics. *Wind Energy* **1,** 46–69. ISSN: 10954244 (1998).

43. Quarton, D. C. The Evolution of Wind Turbine Design Analysis - A Twenty Year Progress Review. *Wind Energy* **24,** 5–24 (1998).

44. Snel, H. Review of Aerodynamics for Wind Turbines. *Wind Energy* **6,** 203–211. ISSN: 1095-4244 (2003).

45. Sørensen, J. N. & Shen, W. Z. Numerical Modeling of Wind Turbine Wakes. *Journal of Fluids Engineering* **124,** 393. ISSN: 00982202 (2002).

46. Hansen, M., Sørensen, J. N., Voutsinas, S., Sørensen, N. & Madsen, H. State of the art in wind turbine aerodynamics and aeroelasticity. *Progress in Aerospace Sciences* **42,** 285–330. ISSN: 03760421 (2006).

47. Benini, E. & Toffolo, A. Optimal Design of Horizontal-Axis Wind Turbines Using Blade-Element Theory and Evolutionary Computation. *Journal of Solar Energy Engineering* **124,** 357. ISSN: 01996231 (2002).

48. Cline, S. & Crawford, C. Comparison of Potential Flow Wake Models for Horizontal-Axis Wind Turbine Rotors. *Mechanical Engineering* **463** (2010).

49. Kloosterman, M. H. M. *Development of the Near Wake behind a Horizontal Axis Wind Turbine* PhD thesis (2009).

50. Prandtl, L. Tragflügeltheorie. I. Mitteilung. *Nachrichten von der Gesellschaft der Wissenschaften zu Göttingen, Mathematisch-Physikalische Klasse* **1918,** 451–477 (1918).

51. Jones, R. T. *The Unsteady Lift of a Wing of Finite Aspect Ratio* tech. rep. 681 (National Advisory Commitee for Aeronautics, Washington D.C., 1940).

52. Weissinger, J. *The Lift Distribution of Swept-Back Wings* tech. rep. (National Advisory Committee For Aeronautics, Washington, D.C., 1947).

53. Breton, S. P., Coton, F. N. & Moe, G. A study on rotational effects and different stall delay models using a prescribed wake vortex scheme and NREL phase VI experiment data. *Wind Energy* **11,** 459–482. ISSN: 10954244 (2008).

54. Basuno, B, Coton, F. N. & Galbraith, R. A. A prescribed wake aerodynamic model for vertical axis wind turbines. *ARCHIVE: Proceedings of the Institution of Mechanical Engineers, Part A: Journal of Power and Energy 1990-1996 (vols 204-210)* **206,** 159–166. ISSN: 0957-6509 (1992).

55. Coton, F. N., Jiang, D & Galbraith, R. A. M. An unsteady prescribed wake model for vertical axis wind turbines. *ARCHIVE: Proceedings of the Institution of Mechanical Engineers, Part A: Journal of Power and Energy 1990-1996 (vols 204-210)* **208,** 13–20. ISSN: 0957-6509 (1994).

56. Coton, F. N., Galbraith, R. A. M. & Jiang, D. The influence of detailed blade design on the aerodynamic performance of straight-bladed vertical axis wind turbines. *ARCHIVE: Proceedings of the Institution of Mechanical Engineers, Part A: Journal of Power and Energy 1990-1996 (vols 204-210)* **210,** 65–74. ISSN: 0957-6509 (1996).

57. Coton, F. N. & Wang, T. The prediction of horizontal axis wind turbine performance in yawed flow using an unsteady prescribed wake model. *Proceedings of the Institution of Mechanical Engineers, Part A: Journal of Power and Energy* **213,** 33–43. ISSN: 0957-6509 (1999).

58. Chattot, J.-J. Optimization of wind turbines using helicoidal vortex model. *Journal of solar energy engineering* (2003).

59. Chattot, J.-J. Extension of a Helicoidal Vortex Model to Account for Blade Flexibility and Tower Interference. *Journal of Solar Energy Engineering* **128,** 455. ISSN: 01996231 (2006).

60. Chattot, J. J. Helicoidal vortex model for steady and unsteady flows. *Computers and Fluids* **35,** 733–741. ISSN: 00457930 (2006).

61. Chattot, J. J. Helicoidal vortex model for wind turbine aeroelastic simulation. *Computers and Structures* **85,** 1072–1079. ISSN: 00457949 (2007).

62. Chattot, J.-J. Effects of blade tip modifications on wind turbine performance using vortex model. *Computers and Fluids* **38,** 1405–1410. ISSN: 0045-7930 (2009).

63. Kocurek, D. Prescribed Wake Lifting Surface Hover Performance Analysis. *Journal of the American Helicopter Society* **22,** 24–35 (1977).

64. Caradonna, F. X. & Tung, C. *Experimental and Analytical Studies of a Model Helicopter Rotor in Hover* tech. rep. 25 (1980).

65. Azzam, H & Taylor, P. *Prescribed Wake Model for Helicopter Rotor Behavior* in *11th European Rotorcraft Forum* (1985), (30)1–14.

66. Zhong, S & Infield, D. G. *Prediction of Wind Turbine Performance in Axial and Non-axial Flows by a Prescribed Wake Model* in *Wind Energy Conversion: Proceeds of the ... British Wind Energy Association Conference* (1991), 261–267.

67. Robison, D., Coton, F. N., Galbraith, R. a. M. & Vezza, M. Application of a Prescribed Wake Aerodynamic Prediction Scheme to Horizontal Ais Wind Turbines in Axial Flow. *Wind Engineering* **19,** 41–51 (1995).

68. Robison, D., Coton, F. N., Galbraith, R. a. M. & Vezza, M. *Development of a Prescribed Wake Model for Performance Prediction in Steady Yawed Flow* in *Wind Energy 1995: presented at Energy and Environemtnal Expo '95* (Houston, Texas, 1995), 211–216.

69. Fisichella, C. *A Case for Improving Prescribed Wake Analysis* in *2000 ASME Wind Energy Symposium, Aerospace Sciences Meetings* (2000), 150–160.

70. Coton, F. N., Wang, T. & Galbraith, R. a. M. An examination of key aerodynamic modelling issues raised by the NREL blind comparison. *Wind Energy* **5,** 199–212. ISSN: 1095-4244 (2002).

71. Murakami, Y., Tanabe, Y. & Saito, S. *A New Appreciation of Prescribed Wake Models for CFD Analysis in View of Aeroacoustic Applications* in *37th European Rotorcraft Forum 2011* (Gallarate, Italy, 2011), 841–850.

72. Sugiura, M., Tanabe, Y., Saito, S., Sugawara, H. & Ohshio, K. *Hybrid Method of CFD and prescribed wake model for Rotorcraft Aeroacoustics and Aerodynamics Prediction* in *38th European Rotorcraft Forum Proceedings* (Amsterdam, Netherlands, 2012), 593–601.

73. Gupta, S. & Leishman, J. G. Stability of methods in the free-vortex wake analysis of wind turbines. *23rd ASME Wind Energy Symposium and 42nd AIAA Aerospace Sciences Meeting, Reno Nevada,* 339–353 (2004).

74. Gupta, S. & Leishman, J. G. *Accuracy of the Induced Velocity of Wind Turbine Wakes Using Vortex Segmentaiton* in *AIAA-2004* (2004).

75. Gupta, S. *Development of a time-accurate viscous Lagrangian vortex wake model for wind turbine applications* PhD thesis (University of Maryland, College Park, 2006).

76. Leishman, J. G., Bhagwat, M. J. & Bagai, A. Free-Vortex Filament Methods for the Analysis of Helicopter Rotor Wakes. *Journal of Aircraft* **39,** 759–775. ISSN: 0021-8669 (2002).

77. Sebastian, T & Lackner, M. Development of a free vortex wake method code for offshore floating wind turbines. *Renewable Energy* (2012).

78. Sebastian, T. *The Aerodynamics and Near Wake of an Offshore Floating Horizontal Axis Wind Turbine* PhD thesis (University of Massachusetts Amherst, 2012).

79. Sezer-Uzol, N. & Uzol, O. Effect of steady and transient wind shear on the wake structure and performance of a horizontal axis wind turbine rotor. *Wind Energy* **16,** 1–17. ISSN: 10954244 (2013).

80. Sant, T., van Kuik, G. & van Bussel, G. J. W. Estimate the Angle of Attack from Blade Pressure Measurements on the NREL Phase VI Rotor Using a Free Wake Vortex Model: Axial Conditions. *Wind Energy,* 549–577 (2006).

81. Sant, T., Van Kuik, G. & Van Bussel, G. J. W. Estimating the angle of attack from blade pressure measurements on the National Renewable Energy Laboratory phase VI rotor using a free wake vortex model: Yawed conditions. *Wind Energy* **12,** 1–32. ISSN: 10954244 (2009).

82. Katz, J. & Plotkin, A. *Low-Speed Aerodynamics* 2nd, 1–609 (Cambridge University Press, Cambridge, United Kingdom, 2001).

83. Karamcheti, K. *Principles of Ideal-Fluid Aerodynamics* 1–636 (Wiley, New York, 1966).

84. Cottet, G.-H. & Koumoutsakos, P. *Vortex Methods: Theory and Practive* 1st (Cambridge University Press, Cambridge, UK, 2000).

85. Xu, G. & Sankar, L. N. Computational Study of Horizontal Axis Wind Turbines. *Journal of Solar Energy Engineering* **122,** 35. ISSN: 01996231 (2000).

86. Xu, G. & Sankar, L. N. Development of engineering aerodynamics models using a viscous flow methodology on the NREL Phase VI rotor. *Wind Energy* **5,** 171–183. ISSN: 1095-4244 (2002).

87. Schmitz, S. & Chattot, J. J. A coupled Navier-Stokes/Vortex-Panel solver for the numerical analysis of wind turbines. *Computers and Fluids* **35,** 742–745. ISSN: 00457930 (2006).

88. Schmitz, S. & Chattot, J.-J. Flow physics and Stokes' theorem in wind turbine aerodynamics. *Computers & Fluids* **36,** 1583–1587. ISSN: 00457930 (2007).

89. Leishman, J. G. Challenges in modelling the unsteady aerodynamics of wind turbines. *Wind Energy* **5,** 85–132. ISSN: 1095-4244 (2002).

90. Barnes, J. & Hut, P. A hierarchocal O(NlogN) force-calculation algorithm. *Nature* **324,** 446–449 (1986).

91. Greengard, L & Rokhlin, V. A Fast Algorithm for Particle Simulations. *Journal of Computational Physics* **73,** 325–348 (1987).

92. Makino, J. The GRAPE project. *Computing in Science and Engineering* **8,** 30–40. ISSN: 15219615 (2006).

93. Darve, E., Cecka, C. & Takahashi, T. The fast multipole method on parallel clusters, multicore processors, and graphics processing units. *Comptes Rendus Mécanique* **339,** 185–193. ISSN: 16310721 (2011).

94. DeVelder, N. B. *Free Wake Potential Flow Vortex Wind Turbine Modeling: Advances in Parallel Processing and Integration of Ground Effects* PhD thesis (University of Massachusetts Amherst, 2014).

95. Einkemmer, L. Evaluation of the Intel Xeon Phi and NVIDIA K80 as accelerators for two-dimensional panel codes. *arXiv preprint,* 1–11. arXiv: `1511.02166` (2015).

96. Portegies Zwart, S., Belleman, R. & Geldof, P. High-performance direct gravitational N-body simulations on graphics processing units. *New Astronomy* **12,** 641–650. arXiv: `0702135v1 [arXiv:cs]` (2007).

97. Rossinelli, D. & Koumoutsakos, P. Vortex methods for incompressible flow simulations on the GPU. *The Visual Computer* **24,** 699–708. ISSN: 0178-2789 (2008).

98. Rossinelli, D., Bergdorf, M., Cottet, G.-H. & Koumoutsakos, P. GPU accelerated simulations of bluff body flows using vortex particle methods. *Journal of Computational Physics* **229,** 3316–3333. ISSN: 00219991 (2010).

99. Stock, M. J. & Gharakhani, A. A GPU-accelerated Boundary Element Method and Vortex Particle Method. *AIAA 40th Fluid Dynamics Conference and,* 1–12 (2010).

100. Yokota, R. *et al.* Fast multipole methods on a cluster of GPUs for the meshless simulation of turbulence. *Computer Physics Communications* **180,** 2066–2078. ISSN: 00104655 (2009).

101. Yokota, R. & Barba, L. Comparing the treecode with FMM on GPUs for vortex particle simulations of a leapfrogging vortex ring. *Computers & Fluids* **45,** 155–161. ISSN: 00457930 (2011).

102. Yokota, R., Narumi, T. & Barba, L. Petascale turbulence simulation using a highly parallel fast multipole method. *Arxiv preprint arXiv:* arXiv: `arXiv:1106.5273v1` (2011).

103. Yokota, R. & Barba, L. Treecode and Fast Multipole Method for N-Body Simulation with CUDA. *GPU Computing Gems Emerald Edition - Chapter 9,* 113–132. arXiv: `arXiv:1010.1482v1` (2011).

104. Sumner, J., Watters, C. S. & Masson, C. CFD in wind energy: The virtual, multiscale wind tunnel. *Energies* **3,** 989–1013. ISSN: 19961073 (2010).

105. Hsu, M.-c., Akkerman, I. & Bazilevs, Y. Finite element simulation of wind turbine aerodynamics : Validation study using NREL Phase VI experiment. *Wind Energy,* 1–20 (2012).

106. Gross, A., Fasel, H. F., Friederich, T. & Kloker, M. J. Numerical investigation of rotational augmentation for S822 wind turbine airfoil. *Wind Energy* **15,** 983–1007. ISSN: 10954244 (2012).

107. Zhang, W. & Samtaney, R. A direct numerical simulation investigation of the synthetic jet frequency effects on separation control of low-Re flow past an airfoil. *Physics of Fluids* **27,** 055101. ISSN: 1070-6631 (2015).

108. Ivanell, S., Sørensen, J. N., Mikkelsen, R. & Henningson, D. Analysis of numerically generated wake structures. *Wind Energy* **12,** 63–80. ISSN: 10954244 (2009).

109. Choi, H. & Moin, P. Grid-point requirements for large eddy simulation: Chapman's estimates revisited. *Physics of Fluids* **24,** 1–6. ISSN: 10706631 (2012).

110. Spalart, P. R., Jou, W. H., Strelets, M. & Allmaras, S. R. Comments on the feasibility of LES for wings and on a hybrid RANS/LES approach. *Advances in DNS/LES* **1,** 4–8 (1997).

111. Sanderse, B, van der Pijl, S. & Koren, B. Review of computational fluid dynamics for wind turbine wake aerodynamics. *Wind Energy* **14,** 799–819 (2011).

112. Sagaut, P. *Large Eddy Simulation for Incompressible Flows: An Introduction* 575. ISBN: 978-3-540-26403-3 (2006).

113. Piomelli, U. Large-eddy simulation: achievements and challenges. *Progress in Aerospace Sciences* **35,** 335–362. ISSN: 03760421 (1999).

114. Moin, P. Advances in large eddy simulation methodology for complex flows. *International Journal of Heat and Fluid Flow* **23,** 710–720. ISSN: 0142727X (2002).

115. Bouffanais, R. Advances and challenges of applied large-eddy simulation. *Computers and Fluids* **39,** 735–738. ISSN: 00457930 (2010).

116. Yang, X., Kang, S. & Sotiropoulos, F. Computational study and modeling of turbine spacing effects infinite aligned wind farms. *Physics of Fluids* **24.** ISSN: 10706631 (2012).

117. Meyers, J. & Meneveau, C. Optimal turbine spacing in fully developed wind farm boundary layers. *Wind Energy* **15,** 305–317. ISSN: 10954244 (2012).

118. Réthoré, P.-E. & Sørensen, N. A discrete force allocation algorithm for modelling wind turbines in computational fluid dynamics. *Wind Energy* **15,** 915–926. ISSN: 10954244. arXiv: `arXiv:1006.4405v1` (2012).

119. Meyers, J. & Meneveau, C. Flow visualization using momentum and energy transport tubes and applications to turbulent flow in wind farms. *Journal of Fluid Mechanics* **715,** 335–358. ISSN: 0022-1120. arXiv: `arXiv:1209.4578v2` (2013).

120. Storey, R. C., Norris, S. E., Stol, K. A. & Cater, J. E. Large eddy simulation of dynamically controlled wind turbines in an offshore environment. *Wind Energy* **16,** 845–864. ISSN: 10954244 (2013).

121. Krogstad, P. Å. & Eriksen, P. E. "Blind test" calculations of the performance and wake development for a model wind turbine. *Renewable Energy* **50,** 325–333. ISSN: 09601481 (2013).

122. VerHulst, C. & Meneveau, C. Large eddy simulation study of the kinetic energy entrainment by energetic turbulent flow structures in large wind farms. *Physics of Fluids* **26.** ISSN: 10897666 (2014).

123. Keck, R.-E., Mikkelsen, R., Troldborg, N., de Maré, M. & Hansen, K. S. Synthetic atmospheric turbulence and wind shear in large eddy simulations of wind turbine wakes. *Wind Energy* **17,** 1247–1267. ISSN: 10954244 (2014).

124. Yang, D., Meneveau, C. & Shen, L. Large-eddy simulation of offshore wind farm. *Physics of Fluids* **26.** ISSN: 10897666 (2014).

125. Xie, S. & Archer, C. Self-similarity and turbulence characteristics of wind turbine wakes via large-eddy simulation. *Wind Energy* **17.** ISSN: 10954244 (2014).

126. Sarmast, S., Chivaee, H. S., Ivanell, S. & Mikkelsen, R. F. Numerical investigation of the wake interaction between two model wind turbines with span-wise offset. *Journal of Physics: Conference Series* **524,** 012137. ISSN: 1742-6596 (2014).

127. Abkar, M. & Porté-agel, F. Influence of atmospheric stability on wind-turbine wakes : A large-eddy simulation study. *Physics of Fluids* **16,** 8101. ISSN: 1070-6631 (2014).

128. Park, J., Basu, S. & Manuel, L. Large-eddy simulation of stable boundary layer turbulence and estimation of associated wind turbine loads. *Wind Energy* **17,** 359–384. ISSN: 10954244 (2014).

129. Yang, X., Sotiropoulos, F., Conzemius, R. J., Wachtler, J. N. & Strong, M. B. Large-eddy simulation of turbulent flow past wind turbines/farms: the Virtual Wind Simulator (VWiS). *Wind Energy* **17.** ISSN: 10954244 (2014).

130. Zhou, N., Chen, J., Adams, D. E. & Fleeter, S. Influence of inflow conditions on turbine loading and wake structures predicted by large eddy simulations using exact geometry. *Wind Energy* **17.** ISSN: 10954244 (2015).

131. Allaerts, D. & Meyers, J. Large eddy simulation of a large wind-turbine array in a conventionally neutral atmospheric boundary layer. *Physics of Fluids* **065108** (2015).

132. Nilsson, K. *et al.* Large-eddy simulations of the Lillgrund wind farm. *Wind Energy* **18,** 449–467. ISSN: 10954244 (2015).

133. Van der Laan, M. P. *et al.* An improved k-ϵ model applied to a wind turbine wake in atmospheric turbulence. *Wind Energy* **18,** 889–907. ISSN: 10954244 (2015).

134. Luo, K. *et al.* Large-eddy simulation and wind-tunnel measurement of aerodynamics and aeroacoustics of a horizontal-axis wind turbine. *Renewable Energy* **77,** 351–362. ISSN: 09601481 (2015).

135. Martínez-Tossas, L, Churchfield, M & Meneveau, C. Large Eddy Simulation of wind turbine wakes: detailed comparisons of two codes focusing on effects of numerics and subgrid modeling. *Journal of Physics: Conference Series* **625,** 012024. ISSN: 1742-6588 (2015).

136. Martínez-Tossas, L. A., Churchfield, M. J. & Leonardi, S. Large eddy simulations of the flow past wind turbines: actuator line and disk modeling. *Wind Energy,* 1047–1060 (2015).

137. Bunge, U., Mockett, C. & Thiele, F. Guidelines for implementing Detached-Eddy Simulation using different models. *Aerospace Science and Technology* **11,** 376–385. ISSN: 12709638 (2007).

138. Spalart, P. R. *et al.* A new version of detached-eddy simulation, resistant to ambiguous grid densities. *Theoretical and Computational Fluid Dynamics* **20,** 181–195. ISSN: 09354964 (2006).

139. Travin, A. K., Shur, M., Spalart, P. & Strelets, M. *Improvement of Delayed Detached-Eddy Simulation for LES with Wall Modelling* in *European Conference on Computational Fluid Dynamics* (2006), 1–23.

140. Batten, P., Goldberg, U. & Chakravarthy, S. Interfacing Statistical Turbulence Closures with Large-Eddy Simulation. *AIAA Journal* **42,** 485–492. ISSN: 0001-1452 (2004).

141. Shur, M, Spalart, P., Strelets, M & Travin, A. Detached-eddy simulation of an airfoil at high angle of attack. *Engineering Turbulence Modelling and Experiments* (1999).

142. Li, Y., Paik, K.-J., Xing, T. & Carrica, P. M. Dynamic Overset CFD Simulations of Wind Turbine Aerodynamics. *Renewable Energy* **37,** 285–298 (2012).

143. Johansen, J, Sørensen, N. N., Michelsen, J. A. & Schreck, S. Detached-Eddy simulation of flow around the NREL phase-VI blade. *ASME 2002 Wind Energy Symposium, WIND2002* **197,** 106–114. ISSN: 10954244 (2002).

144. Troldborg, N., Zahle, F., Réthoré, P.-E. & Sørensen, N. N. Comparison of wind turbine wake properties in non-sheared inflow predicted by different computational fluid dynamics rotor models. *Wind Energy* **18,** 1239–1250. ISSN: 10954244 (2015).

145. Durbin, P. A. & Reif, B. A. P. *Statistical Theory and Modeling for Turbulent Flows* 2nd ed. (John Wiley & Sons, Ltd, West Sussex, United Kingdom, 2011).

146. Réthoré, P. E., Sørensen, N. N. & Bechmann, A. *Modelling issues with wind turbine wake and atmospheric turbulence* in *TORQUE proceedings* (2010).

147. Sørensen, N. N. & Hansen, M. O. L. *Rotor performance predictions using a Navier-Stokes method* in *ASME Wind Energy Symposium, Aerospace Sciences Meetings* (1998), 52.

148. Duque, E. P. N., van Dam, C. & Hughes, S. *Navier-Stokes Simulations of the NREL Combined Experiment Phase II Rotor* in *AIAA 37th Aerospace Sciences Meeting and Exhibit* (1999), 143–.

149. Sørensen, N. N., Michelsen, J. A. & Schreck, S. Navier-Stokes predictions of the NREL phase VI rotor in the NASA Ames 80 ft x 120 ft wind tunnel. *Wind Energy* **5,** 151–169. ISSN: 1095-4244 (2002).

150. Chaviaropoulos, P. K. *et al.* Viscous and Aeroelastic Effects on Wind Turbine Blades. The VISCEL project. Part I: 3D Navier-Stokes Rotor simulations. *Wind Energy* **6,** 365–385. ISSN: 1095-4244 (2003).

151. Sørensen, N. N. & Johansen, J. *UPWIND, aerodynamics and aero-elasticity rotor aerodynamics in atmospheric shear flow* in *European Wind Energy Conference and Exhibition 2007, EWEC 2007* **2** (2007). ISBN: 9781622764686.

152. Potsdam, M. A. & Mavriplis, D. J. *Unstructured Mesh CFD Aerodynamic Analysis of the NREL Phase VI Rotor* in *47th AIAA Aerospace Sciences Meeting* (AIAA, Orlando, Florida, 2009).

153. Zahle, F., Sørensen, N. N. & Johansen, J. Wind turbine rotor-tower interaction using an incompressible overset grid method. *Wind Energy* **12,** 594–619. ISSN: 10954244 (2009).

154. Sørensen, N. N. CFD modelling of laminar-turbulent transition for airfoils and rotors using the Gamma-Re model. *Wind Energy* **12,** 715–733. ISSN: 10954244 (2009).

155. Bechmann, A., Sørensen, N. N. & Zahle, F. CFD simulations of the MEXICO rotor. *Wind Energy* **14,** 677–689. ISSN: 10954244 (2011).

156. Lanzafame, R., Mauro, S. & Messina, M. Wind turbine CFD modeling using a correlation-based transitional model. *Renewable Energy* **52,** 31–39. ISSN: 09601481 (2013).

157. Quon, E. W., Smith, M. J. & Whitehouse, G. R. A Novel Computational Approach to High Fidelity Wind Turbine Flow Simulation. *69th American Helicopter Society International Annual Forum 2013: Vertical Flight Technical Society* **2,** 1540–1551 (2013).

158. AbdelSalam, A. M. & Ramalingam, V. Wake prediction of horizontal-axis wind turbine using full-rotor modeling. *Journal of Wind Engineering and Industrial Aerodynamics* **124,** 7–19. ISSN: 01676105 (2014).

159. Carrión, M *et al.* Computational fluid dynamics analysis of the wake behind the MEXICO rotor in axial flow conditions. *Wind Energy,* 1023–1045 (2015).

160. Guntur, S. & Sørensen, N. N. A study on rotational augmentation using CFD analysis of flow in the inboard region of the MEXICO rotor blades. *Wind Energy* **18,** 745–756. ISSN: 10954244. arXiv: `arXiv:1006.4405v1` (2015).

161. Song, Y. & Perot, J. B. CFD Simulation of the NREL Phase VI Rotor. *Wind Engineering* **39,** 299–310. ISSN: 0309524X. arXiv: `1404.6183` (2015).

162. Make, M. & Vaz, G. Analyzing scaling effects on offshore wind turbines using CFD. *Renewable Energy* **47,** 1–15. ISSN: 09601481 (2015).

163. Mann, J. Wind field simulation. *Probabilistic Engineering Mechanics* **13,** 269–282. ISSN: 02668920 (1998).

164. Calaf, M., Meneveau, C. & Meyers, J. Large eddy simulation study of fully developed wind-turbine array boundary layers. *Physics of Fluids* **22,** 1–16. ISSN: 10706631 (2010).

165. Mo, J. O., Choudhry, A., Arjomandi, M. & Lee, Y. H. Large eddy simulation of the wind turbine wake characteristics in the numerical wind tunnel model. *Journal of Wind Engineering and Industrial Aerodynamics* **112,** 11–24. ISSN: 01676105 (2013).

166. Wood, S. L., Deiterding, R. & Technology, F. A Lattice Boltzmann Method for Horizontal Axis Wind Turbine Simulation, 1–18 (2015).

167. Xu, J. Wake Interaction of NREL Wind Turbines Using a Lattice Boltzmann Method. *Sustainable Energy* **4,** 1–6 (2016).

168. Vorobyev, A. Y. & Guo, C. Multifunctional surfaces produced by femtosecond laser pulses. *Journal of Applied Physics* **117.** ISSN: 10897550 (2015).

169. Gogte, S. *et al.* Effective slip on textured superhydrophobic surfaces. *Physics of Fluids* **17,** 051701. ISSN: 10706631 (2005).

170. Min, T. & Kim, J. Effects of hydrophobic surface on skin-friction drag. *Physics of Fluids* **16,** L55. ISSN: 10706631 (2004).

171. Fukagata, K., Kasagi, N. & Koumoutsakos, P. A theoretical prediction of friction drag reduction in turbulent flow by superhydrophobic surfaces. *Physics of Fluids* **18,** 051703. ISSN: 10706631 (2006).

172. Martell, M. B., Perot, J. B. & Rothstein, J. P. Direct numerical simulations of turbulent flows over superhydrophobic surfaces. *Journal of Fluid Mechanics* **620,** 31. ISSN: 0022-1120 (2009).

173. Martell, M. B., Rothstein, J. P. & Perot, J. B. An analysis of superhydrophobic turbulent drag reduction mechanisms using direct numerical simulation. *Physics of Fluids* **22,** 065102. ISSN: 10706631 (2010).

174. Ou, J., Perot, B. & Rothstein, J. P. Laminar drag reduction in microchannels using ultrahydrophobic surfaces. *Physics of Fluids* **16,** 4635–4643. ISSN: 10706631 (2004).

175. Shirtcliffe, N. J., McHale, G., Atherton, S. & Newton, M. I. An introduction to superhydrophobicity. *Advances in colloid and interface science* **161,** 124–38. ISSN: 1873-3727 (2010).

176. Rothstein, J. P. Slip on Superhydrophobic Surfaces. *Annual Review of Fluid Mechanics* **42,** 89–109. ISSN: 0066-4189 (2010).

177. Guo, Z., Liu, W. & Su, B.-L. Superhydrophobic surfaces: from natural to biomimetic to functional. *Journal of colloid and interface science* **353,** 335–55. ISSN: 1095-7103 (2011).

178. Jung, Y. C. & Bhushan, B. Biomimetic structures for fluid drag reduction in laminar and turbulent flows. *Journal of Physics: Condensed Matter* **22,** 035104. ISSN: 1361-648X (2010).

179. Antonini, C., Innocenti, M., Horn, T., Marengo, M. & Amirfazli, a. Understanding the effect of superhydrophobic coatings on energy reduction in anti-icing systems. *Cold Regions Science and Technology* **67,** 58–67. ISSN: 0165232X (2011).

180. Samaha, M. a., Tafreshi, H. V. & Gad-el Hak, M. Superhydrophobic surfaces: From the lotus leaf to the submarine. *Comptes Rendus Mécanique* **340,** 18–34. ISSN: 16310721 (2012).

181. Celia, E., Darmanin, T., Taffin de Givenchy, E., Amigoni, S. & Guittard, F. Recent advances in designing superhydrophobic surfaces. *Journal of Colloid and Interface Science* **402,** 1–18. ISSN: 00219797 (2013).

182. Daniello, R. J., Waterhouse, N. E. & Rothstein, J. P. Drag reduction in turbulent flows over superhydrophobic surfaces. *Physics of Fluids* **21,** 085103. ISSN: 10706631 (2009).

183. Bhushan, B., Jung, Y. C. & Koch, K. Micro-, nano- and hierarchical structures for superhydrophobicity, self-cleaning and low adhesion. *Philosophical transactions. Series A, Mathematical, physical, and engineering sciences* **367,** 1631–1672. ISSN: 1364-503X (2009).

184. Öner, D. & McCarthy, T. J. Ultrahydrophobic surfaces. Effects of topography length scales on wettability. *Langmuir* **16,** 7777–7782. ISSN: 07437463 (2000).

185. Sagol, E., Reggio, M. & Ilinca, A. Issues concerning roughness on wind turbine blades. *Renewable and Sustainable Energy Reviews* **23,** 514–525. ISSN: 13640321 (2013).

186. Schlichting, H. *Boundary Layer Theory* 7th. ISBN: 0-07-055334-3 (1979).

187. Jimenez, J. Turbulent Flows Over Rough Walls. *Annual Review of Fluid Mechanics* **36,** 173–196. ISSN: 0066-4189 (2004).

188. Cebeci, T. & Smith, A. M. O. *Analysis of Turbulent Boundary Layers* ISBN: 0323151051, 9780323151054 (Academic Press, New York, NY, 1974).

189. Nikuradse, J. *Laws of Flow in Rough Pipes* tech. rep. Translation 1950 (National Advisory Committee for Aeronautics, Washington, D.C., 1933), 1–62.

190. Blocken, B., Stathopoulos, T. & Carmeliet, J. CFD simulation of the atmospheric boundary layer: wall function problems. *Atmospheric Environment* **41,** 238–252. ISSN: 13522310 (2007).

191. Flack, K. A. & Schultz, M. P. Roughness effects on wall-bounded turbulent flows. *Physics of Fluids* **26,** 1–17. ISSN: 1070-6631 (2014).

192. Aupoix, B. A General Strategy to Extend Turbulence Models to Rough Surfaces: Application to Smith's k-L Model. *Journal of Fluids Engineering* **129,** 1245. ISSN: 00982202 (2007).

193. Flack, K. A. & Schultz, M. P. Review of Hydraulic Roughness Scales in the Fully Rough Regime. *Journal of Fluids Engineering* **132,** 041203. ISSN: 00982202 (2010).

194. Myers, T. G. & Charpin, J. P. F. A mathematical model for atmospheric ice accretion and water flow on a cold surface. *International Journal of Heat and Mass Transfer* **47,** 5483–5500. ISSN: 00179310 (2004).

195. Ackley, S. & Templeton, M. *Computer Modeling of Atmospheric Ice Accretion* tech. rep. (U.S. Army Cold Regions Research and Engineering Laboratory, Hanover, New Hapshire, USA, 1979).

196. Shin, J. Characteristics of surface roughness associated with leading edge ice accretion. *Journal of Aircraft* **33,** 316–321 (1994).

197. Jasinski, W. J., Noe, S. C., Selig, M. S. & Bragg, M. B. *Wind turbine performance under icing conditions* in *AIAA* (1997), 1–7.

198. Bragg, M., Broeren, A. & Blumenthal, L. Iced-airfoil aerodynamics. *Progress in Aerospace Sciences* **41,** 323–362. ISSN: 03760421 (2005).

199. Bragg, M *et al.* Airfoil Ice-Accretion Aerodynamics Simulation. *AIAA Paper* **85,** 1–22 (2007).

200. Horak, V., Rozehnal, D., Chara, Z. & Hyll, A. *CFD and Experimental Study of Aerodynamic Degradation of Iced Airfoils* in *Colloquium Fluid Dynamics* (Institute of Thermodynamics, Prague, 2008), 1–10.

201. Makkonen, L., Laakso, T., Marjaniemi, M. & Finstad, K. J. Modelling and prevention of ice accretion on wind turbines. *Wind Engineering* **25,** 3–21. ISSN: 0309-524X (2009).

202. Fu, P. & Farzaneh, M. A CFD approach for modeling the rime-ice accretion process on a horizontal-axis wind turbine. *Journal of Wind Engineering and Industrial Aerodynamics* **98,** 181–188. ISSN: 01676105 (2010).

203. Virk, M. S., Homola, M. C. & Nicklasson, P. J. Effect of Rime Ice Accretion on Aerodynamic Characteristics of Wind Turbine Blade Profiles. *Wind Engineering* **34,** 207–218. ISSN: 0309-524X (2010).

204. Barber, S, Wang, Y, Jafari, S, Chokani, N & Abhari, R. *The Impact of Ice Formation on Wind Turbine Performance and Aerodynamics* in *Eurpean Wind Energy Conference* (Warsaw, 2010).

205. Kinzel, M. & Sarofeen, C. *A Finite-Volume Approach to Modeling Ice Accretion* in *28th AIAA Applied Aerodynamics Conference* (Chicago, IL, 2010), 1–16. ISBN: 9781617389269.

206. Jha, P. K., Brillembourg, D. & Schmitz, S. *Wind Turbines under Atmospheric Icing Conditions - Ice Accretion Modeling, Aerodynamics, and Control Strategies for Mitigating Performance Degradation* in *50th AIAA Aerospace Sciences Meeting* (Nashville, Tennesee, 2012), 1–11. ISBN: 978-1-60086-936-5.

207. Homola, M. C., Virk, M. S., Nicklasson, P. J. & Sundsbø, P. A. Performance losses due to ice accretion for a 5 MW wind turbine. *Wind Energy* **15,** 379–389. ISSN: 10954244 (2012).

208. Han, Y., Palacios, J. & Schmitz, S. Scaled ice accretion experiments on a rotating wind turbine blade. *Journal of Wind Engineering and Industrial Aerodynamics* **109,** 55–67. ISSN: 01676105 (2012).

209. Yi, X., Wang, K. C. & Ma, H. L. Prediction of Ice Accretion on Wind Turbine with Numerical Method. *Advanced Materials Research* **512-515,** 754–757. ISSN: 1662-8985 (2012).

210. Anttho, A. M. *In-Cloud Ice Accretion Modeling on Wind Turbine Blades Using Extended Messinger Model* in *13th International nergy Conversion Engineering Conference* (Red Hook, NY, 2015), 55–69.

211. Wright, B. *User Manual for the NASA Glenn Ice Accretion Code LEWICE Version 2.2.2* tech. rep. August (NASA, 2002).

212. Ligrani, P. & Moffat, R. Structure of transitionally rough and fully rough turbulent boundary layers. *Journal of Fluid Mechanics* **162,** 69–98 (1986).

213. Raupach, M. Rough-wall turbulent boundary layers. *Applied Mechanics Reviews* (1991).

214. Krogstad, P. & Antonia, R. Surface roughness effects in turbulent boundary layers. *Experiments in Fluids* **27,** 450–460. ISSN: 0723-4864 (1999).

215. Shockling, M. A., Allen, J. J. & Smits, A. J. Roughness effects in turbulent pipe flow. *Journal of Fluid Mechanics* **564,** 267. ISSN: 0022-1120 (2006).

216. Orlandi, P. The importance of wall-normal Reynolds stress in turbulent rough channel flows. *Physics of Fluids* **25,** 110813. ISSN: 10706631 (2013).

217. Park, H., Park, H. & Kim, J. A numerical study of the effects of superhydrophobic surface on skin-friction drag in turbulent channel flow. *Physics of Fluids* **25,** 110815. ISSN: 10706631 (2013).

218. Kim, J. Physics and control of wall turbulence for drag reduction. *Philosophical transactions. Series A, Mathematical, physical, and engineering sciences* **369,** 1396–411. ISSN: 1364-503X (2011).

219. Aupoix, B. Roughness Corrections for the k-omega Shear Stress Transport Model : Status and Proposals. **137,** 1–10 (2015).

220. Apsley, D. CFD Calculation of Turbulent Flow with Arbitrary Wall Roughness. *Flow, Turbulence and Combustion* **78,** 153–175. ISSN: 1386-6184 (2007).

221. Suga, K., Craft, T. & Iacovides, H. An analytical wall-function for turbulent flows and heat transfer over rough walls. *International Journal of Heat and Fluid Flow* **27,** 852–866. ISSN: 0142727X (2006).

222. Ambrosini, W., Pucciarelli, a. & Borroni, I. A methodology for including wall roughness effects in k-ε low-Reynolds turbulence models. *Nuclear Engineering and Design* **286,** 175–194. ISSN: 00295493 (2015).

223. Aupoix, B. & Spalart, P. Extensions of the Spalart–Allmaras turbulence model to account for wall roughness. *International Journal of Heat and Fluid Flow* **24,** 454–462. ISSN: 0142727X (2003).

224. Durbin, P. A., Medic, G., Seo, J.-M., Eaton, J. K. & Song, S. Rough Wall Modification of Two-Layer k-ϵ. *Journal of Fluids Engineering* **123,** 16. ISSN: 00982202 (2001).

225. George, J, Simone, A. D., Iaccarino, G & Jimenez, J. Modeling roughness effects in turbulent boundary layers by elliptic relaxation. *Center for Turbulence Reseach Proceedings of the Summer Program 2010,* 119–128 (2010).

226. Han, L. A mixing length model for turbulent boundary layers over rough surfaces. *International journal of heat and mass transfer* **34,** 2053–2062 (1991).

227. Hellsten, A. & Laine, S. Extension of the kW Shear-Stress Transport Turbulence Model For Flows Over Rough Surfaces. *AIAA Atmospheric Flight Mechanics Conference* (1997).

228. Knopp, T., Eisfeld, B. & Calvo, J. B. A new extension for k–W turbulence models to account for wall roughness. *International Journal of Heat and Fluid Flow* **30,** 54–65. ISSN: 0142727X (2009).

229. Langel, C. *et al.* A Computational Approach to Simulating the Effects of Realistic Surface Roughness on Boundary Layer Transition. *AIAA 52nd Aerospace Sciences Meeting* (2014).

230. Leighton, R. & Walker, D. Reynolds stress modeling for rough wall turbulence: An invited Paper. *37th AIAA Fluid Dynamics Conference and ...,* 2546–2561 (2007).

231. Lu, M.-H. & Liou, W. W. A new second-order closure model for rough-wall turbulent flows using the Brinkman equation. *Computers & Fluids* **39,** 626–639. ISSN: 00457930 (2010).

232. Tarada, F. Prediction of rough-wall boundary layers using a low Reynolds number k-ϵ model. *International Journal of Heat and Fluid Flow,* 331–345 (1990).

233. Wilcox, D. C. Formulation of the k-w Turbulence Model Revisited. *AIAA Journal* **46,** 2823–2838. ISSN: 0001-1452 (2008).

234. Zhang, H, Faghri, M & White, F. A new low-Reynolds-number k-ϵ model for turbulent flow over smooth and rough surfaces. *Journal of Fluids Engineering* **118,** 255–259 (1996).

235. Vijiapurapu, S. & Cui, J. Performance of turbulence models for flows through rough pipes. *Applied Mathematical Modelling* **34,** 1458–1466. ISSN: 0307904X (2010).

236. Patel, V. & Yoon, J. Application of turbulence models to separated flow over rough surfaces. *Journal of Fluids Engineering* **177,** 234–241 (1995).

237. Lu, M.-H. & Liou, W. W. Assessment of two low-Reynolds-number k-epsilon models in turbulent boundary layers with surface roughness. *Journal of Spacecraft and Rockets* **44,** 1307–1316. ISSN: 0022-4650 (2007).

238. Craft, T. J., Launder, B. E. & Suga, K. Development and application of a cubic eddy-viscosity model of turbulence. *International Journal of Heat and Fluid Flow* **17,** 108–115. ISSN: 0142727X (1996).

239. Perot, B. Turbulence modeling using body force potentials. *Physics of Fluids* **11,** 2645–2656. ISSN: 1070-6631 (1999).

240. Perot, B & Moin, P. *A new approach to turbulence modeling* in *Center for Turbulence Reseach Proceedings of the Summer Program 1996* (1996), 35–46.

241. Zhang, X. & Perot, B. Turbulent Vortex Shedding From Triangle Cylinder Using the Turbulent Body Force Potential Model. *Proceedings of ASME Fluids Engineering Division, FEDSM2000-11172,* 1–6 (2000).

242. Perot, B., Are, S. & Wang, C. Application of the turbulent potential model to complex flows. *... Symposium on Engineering Turbulence ...* (2002).

243. Are, S., Zhang, X. & Perot, B. *Application of the turbulent potential model to unsteady flows and three-dimensional boundary layers* in *The 9th International Symposium on Transport Phenomena and Dynamics of Rotating Machinery* (2002), 1–9.

244. Perot, B. *Turbulence Modeling Using Body Force Potentials* tech. rep. (AFOSR, Arlington, VA, 2003), 1–48.

245. Pope, S. B. *Turbulent Flows* 2008th ed. (Cambridge University Press, Cambridge, UK, 2000).

246. Sveningsson, A. & Davidson, L. Assessment of realizability constraints in v2-f turbulence models. *International Journal of Heat and Fluid Flow* **25,** 785–794. ISSN: 0142727X (2004).

247. Lee, M. & Moser, R. D. Direct numerical simulation of turbulent channel flow up to ReT $\approx$ 5200. *Journal of Fluid Mechanics* **774,** 395–415. ISSN: 14697645. arXiv: 1410.7809 (2015).

248. Moser, R. D., Kim, J. & Mansour, N. N. Direct numerical simulation of turbulent channel flow up to Re[sub τ]=590. *Physics of Fluids* **11,** 943. ISSN: 10706631 (1999).

249. Antonia, R. A., Djenidi, L. & Spalart, P. R. Anisotropy of the dissipation tensor in a turbulent boundary layer. *Physics of Fluids* **6,** 2475–2479 (1994).

250. Durbin, P. A. Near-wall turbulence closure modeling without "damping functions". *Theoretical and Computational Fluid Dynamics* **3,** 1–13. ISSN: 09354964 (1991).

251. Durbin, P. A. Separated flow computations with the k-epsilon-v-squared model. *AIAA Journal* **33,** 659–664 (1995).

252. Lien, F. S. & Durbin, P. Non-linear k-E-v2 modeling with application to high-lift. *Center for Turbulence Reseach Proceedings of the Summer Program 1996.* ISSN: 1057-7149 (1996).

253. Kalitzin, G. Application of turbulence models to high-lift airfoils. *Center for Turbulence Research Annual Research Briefs 1997,* 165–177 (1997).

254. Durbin, P. A. On the k-Epsilon Stagnation Point Anomaly. *International Journal of Heat and Fluid Flow* **17,** 89–90. ISSN: 0142727X (1996).

255. Hanjalic, K., Popovac, M & Hadz, M. A robust near-wall elliptic-relaxation eddy-viscosity turbulence model for CFD. *International Journal of Heat and Fluid Flow* **25,** 1047–1051 (2004).

256. Laurence, D. R., Uribe, J. C. & Utyuzhnikov, S. V. A Robust Formulation of the v2-f Model. *Flow, Turbulence and Combustion* **73,** 169–185. ISSN: 13866184 (2004).

257. Jonkman, J., Butterfield, S, Musial, W & Scott, G. *Definition of a 5-MW Reference Wind Turbine for Offshore System Development* tech. rep. February (2009), 1–75.

258. Baughn, J., Yan, X. & Masbah, M. *The effect of Reynolds number on the heat transfer distribution from a flat plate to an impinging jet* in *ASME Winter annual meeting* (1992).

259. Cooper, D, Jackson, D. C., Launder, B. E. & Liao, G. X. Impinging jet studies for turbulence model assessment - I. Flow-field experiments. *International Journal of Heat and Mass Transfer* **36,** 2675–2684 (1993).

260. Craft, T. J., Graham, L. J. W. & Launder, B. E. Impinging jet studies for turbulence model assessment - II. An examination of the performance of four turbulence models. *International Journal of Heat and Mass Transfer* **36,** 2685–2697 (1993).

261. Behnia, M, Parneix, S & Durbin, P. A. Prediction of heat transfer in an axisymmetric turbulent jet impinging on a flat plate. *International Journal of Heat and Mass Transfer* **41,** 1845–1855. ISSN: 00179310 (1998).

262. Menter, F. & Esch, T. Elements of Industrial Heat Transfer Predictions. *Proceedings of COBEM* **20,** 117–127 (2001).

263. Menter, F. R., Kuntz, M & Langtry, R. Ten Years of Industrial Experience with the SST Turbulence Model. *Turbulence, Heat and Mass Transfer 4* (2003).

264. Ramsay, R. R., Hoffmann, M. J. & Gregorek, G. *Effects of Grit Roughness and Pitch Oscillations on the S809 Airfoil* tech. rep. December (National Renewable Energy Laboratory, 1995).

265. Mauro, S, Lanzafame, R, Messina, M & Pirrello, D. Transition turbulence model calibration for wind turbine airfoil characterization through the use of a Micro-Genetic Algorithm. *International Journal of Energy and Environmental Engineering* **8,** 359–374. ISSN: 2251-6832 (2017).

266. Wang, C. & Perot, B. Prediction of turbulent transition in boundary layers using the turbulent potential model. *Journal of Turbulence,* 1–15 (2002).

267. Duque, E. P. N., Burklund, M. D. & Johnson, W. Navier-Stokes and Comprehensive Analysis Performance Predictions of the NREL Phase VI Experiment. *Journal of Solar Energy Engineering* **125,** 457. ISSN: 01996231 (2003).

268. Ferrer, E & Munduate, X. Wind turbine blade tip comparison using CFD. *Journal of Physics: Conference Series* **75,** 012005. ISSN: 1742-6596 (2007).

269. Gonzalez, A. & Munduate, X. Three-Dimensional and Rotational Aerodynamics on the NREL Phase VI Wind Turbine Blade. *Journal of Solar Energy Engineering* **130,** 031008. ISSN: 01996231 (2008).

270. Potsdam, M. A. & Mavriplis, D. J. Unstructured Mesh CFD Aerodynamic Analysis of the NREL Phase VI Rotor. *47th AIAA Aerospace Sciences Meeting Including The New Horizons Forum and Aerospace Exposition,* 1–18 (2009).

271. Sezer-Uzol, N., Gupta, A. & Long, L. N. *3-D time-accurate inviscid and viscous CFD simulations of wind turbine rotor flow fields* in *Lecture Notes in Computational Science and Engineering* **67 LNCSE** (2009), 457–464. ISBN: 978-3-540-92743-3.

272. Sørensen, N. N. & Schreck, S. Computation of the National Renewable Energy Laboratory Phase-VI rotor in pitch motion during standstill. *Wind Energy,* 425–442 (2012).

273. Elfarra, M. A., Sezer-Uzol, N. & Akmandor, I. S. NREL VI rotor blade: numerical investigation and winglet design and optimization using CFD. *Wind Energy* **17,** 605–626. ISSN: 10954244 (2014).

274. Hand, M. M. *et al. Unsteady Aerodynamics Experiment Phase VI : Wind Tunnel Test Configurations and Available Data Campaigns* tech. rep. December (National Renewable Energy Laboratory, 2001), 1–299.

275. Jonkman, J. M. *Modeling of the UAE Wind Turbine for Refinement of FAST_AD* tech. rep. December (National Renewable Energy Laboratory, 2003), 184.

276. Rumsey, C. L., Gatski, T. B., Sellers, W. L., Vatsa, V. N. & Viken, S. A. Summary of the 2004 CFD validation workshop on Synthetic Jets And Turbulent Separation Control. *2nd AIAA Flow Control Conference,* 1–45 (2004).

277. Viken, S. A., Vatsa, V. N., Rumsey, C. L. & Carpenter, M. H. *Flow Control Analysis on the Hump Model with RANS Tools* in *41st Aerospace Sciences Meeting & Exhibit Reno , NV* (American Institute of Aeronautics and Astronautics, Reno, NV, 2003).

278. Rumsey, C. L. & Jeyapaul, E. Pressure-strain and near-wall modeling for two-dimensional separated flows. *Center for Turbulence Research: Proceedings of the Summer Program 2012,* 273–282 (2012).